ISTANBUL TECHNICAL UNIVERSITY ★ GRADUATE SCHOOL OF SCIENCE ENGINEERING AND TECHNOLOGY

EFFECTS OF COATING ON THE MECHANICAL AND ACOUSTIC PROPERTIES OF NANOPOROUS METALS

Ph.D. THESIS

Yunus Onur YILDIZ

Department of Mechanical Engineering

Mechanical Engineering Doctorate Programme

NOVEMBER 2019

ISTANBUL TECHNICAL UNIVERSITY ★ GRADUATE SCHOOL OF SCIENCE ENGINEERING AND TECHNOLOGY

EFFECTS OF COATING ON THE MECHANICAL AND ACOUSTIC PROPERTIES OF NANOPOROUS METALS

Ph.D. THESIS

Yunus Onur YILDIZ
(503142012)

Department of Mechanical Engineering

Mechanical Engineering Doctorate Programme

Thesis Advisor: Assoc. Prof. Dr. Mesut KIRCA

NOVEMBER 2019

İSTANBUL TEKNİK ÜNİVERSİTESİ ★ FEN BİLİMLERİ ENSTİTÜSÜ

NANO GÖZENEKLİ METALLERDE YÜZEY KAPLAMANIN MEKANİK ve AKUSTİK ÖZELLİKLERE OLAN ETKİLERİ

DOKTORA TEZİ

Yunus Onur YILDIZ
(503142012)

Makina Mühendisliği Anabilim Dalı

Makina Mühendisliği Doktora Programı

Tez Danışmanı: Doç. Dr. Mesut KIRCA

KASIM 2019

Yunus Onur YILDIZ, a Ph.D. student of ITU Graduate School of Science Engineering and Technology 503142012 successfully defended the thesis entitled "EFFECTS OF COATING ON THE MECHANICAL AND ACOUSTIC PROPERTIES OF NANO-POROUS METALS", which he/she prepared after fulfilling the requirements specified in the associated legislations, before the jury whose signatures are below.
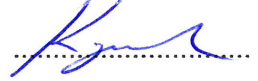
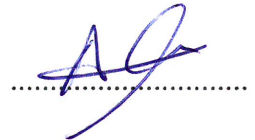|		
Thesis Advisor :	**Assoc. Prof. Mesut KIRCA** Istanbul Technical University	
Jury Members :	**Assoc. Prof. Dr. Ahmet Sinan ÖKTEM** Gebze Technical University	
	Assoc. Prof. Dr. Devrim Barış KAYMAK Istanbul Technical University	
	Assist. Prof. Dr. Nazar İLERİ ERCAN Bogazici University	
	Assist. Prof. Dr. Atakan ALTINKAYNAK Istanbul Technical University	

Date of Submission :   **30 September 2019**
Date of Defense :   **04 November 2019**

To my spouse and children,

FOREWORD

I would like to express my sincere gratitude to my advisor Assoc. Prof. Mesut KIRCA for his significant and valuable contributions. He has always strongly supported me in my research studies with patience and encouragement. I am grateful to him for showing me what a good academician should be.

In addition, I would like to thank my co-advisor Prof. Aylin AHADI. She supported my research all the time and provided me with an amazing opportunity to witness and experience the research environment at Lund University. I would also like to thank Prof. Ata MUĞAN for his help and support.

Furthermore, I would like to thank all my friends and colleagues who helped to complete this thesis, be it with discussions, supports, and encouragements.

I sincerely thank my parents, Neriman and Üzeyir YILDIZ, for their lifelong support and motivation. All this would not have been possible without them. Last, but not least, I would like to dedicate my deepest gratitude to my love Olga YASHCHANKA-YILDIZ, and my children. Their love is an eternal source of energy for me even when I am far from them.

November 2019   Yunus Onur YILDIZ

TABLE OF CONTENTS

ABBREVIATIONS

aCNA	:	Adaptive Common Neighbor Analysis
Ag@np-Au	:	Silver Coated Nanoporous Gold
ALD	:	Atomic Layer Deposition
ALE	:	Atomic Layer Epitaxy
BCC	:	Body Centered Cubic
CNA	:	Common Neighbor Analysis
CNT	:	Carbon Nanotube
EAM	:	Embedded Atom Method
FCC	:	Face Centered Cubic
HCP	:	Hexagonal Close Packed
LAMMPS	:	Large-scale Atomic/Molecular Massively Parallel Simulator
LJ	:	Lennard-Jones
MD	:	Molecular Dynamics
np	:	Nanoporous
np-Au	:	Nanoporous Gold
OTHER	:	Undefined Crystal Structure
Pt@np-Au	:	Platinum Coated Nanoporous Gold
SEM	:	Scanning Electron Microscope

SYMBOLS

a	:	Acceleration
Ag	:	Silver
Au	:	Gold
E	:	Energy
F	:	Force
K	:	Kinetic Energy
m	:	Mass
N	:	Particle
P	:	Pressure
Pt	:	Platinum
r	:	Position Vector
T	:	Temperature
t	:	Time
U	:	Potential Energy
V	:	Volume
ε	:	Bond Energy
μ	:	Chemical Energy
ρ	:	Atomic Electron Density
σ	:	Stress, Cutoff Distance
ϕ	:	Pair Potential

LIST OF TABLES

LIST OF FIGURES

EFFECTS OF COATING ON THE MECHANICAL AND ACOUSTIC PROPERTIES OF NANOPOROUS METALS

SUMMARY

Nanoporous materials are porous materials whose porous structure cells' diameters vary between 1-100 nanometers. Due to their novel structural properties and large interconnected internal surface at the atomistic scale, usage of nanoporous materials is increasing day by day. Having certain nanoscale morphological features they have been employed as sensors, actuators, insulators, electrodes, energy absorbents and also for adsorption and separation in recent years. The interest in studying this class of materials derives from their characteristic high surface-to-volume ratio. In addition, another interesting subject is coating of a nanoporous material with an other functional materials, and it helps to enhance physical or chemical properties of the former.

In this thesis, firstly, a new method developed for the generation of periodic atomistic models of coated and uncoated nanoporous metals (NPMs) is presented by examining the thermodynamic stability of coated and uncoated nanoporous structures. The proposed method is mainly based on the Voronoi tessellation technique, which provides the ability to control cross-sectional dimension and slenderness of ligaments as well as the thickness of coating. By the utilization of the method, molecular dynamic (MD) simulations of randomly structured NPMs with coating can be performed efficiently in order to investigate their physical characteristics. In this context, for the purpose of demonstrating the functionality of the method, sample atomistic models of Au/Pt NPMs are generated and the effects of coating and porosity on the thermodynamic stability are investigated by using MD simulations. Based on the results, while it is demonstrated that coating the nanoporous structures slightly decreases the structural stability causing atomistic configurational changes, it is also shown that the stability of the atomistic models is higher at lower porosities. Furthermore, adaptive common neighbour analysis is also performed to identify the stabilized atomistic structure after the coating process, which provides direct foresights for the mechanical behaviour of coated nanoporous structures.

Secondly, the mechanical properties of nanoporous gold (np-Au) coated with different ultrathin metallic materials (i.e., platinum and silver) are studied through molecular dynamics simulations. A proposed atomistic modelling technique, which is based on the Voronoi tessellation method providing periodic atomistic specimens, is used for the geometric representation of np-Au structure. Three different coating thickness values are used to examine the role of thickness on the coating performance under tensile loading at a constant strain rate. Several parameters, including Young's modulus, yield, and ultimate strengths, are utilized to compare the mechanical characteristics of coated and uncoated np-Au specimens. Moreover, adaptive common neighbor analyses are performed on the specimens for the purpose of understanding the deformation mechanisms of coated and uncoated nanoporous specimens comprehensively by monitoring the microstructural evolution of the crystal structure of the specimens

within the deformation process. As a main finding from the simulations, it is observed that the mechanical properties of np-Au are improved by coating independently of the coating material type. However, enhancements on the yield and ultimate strengths maintained by platinum coating are greater than those provided by the silver coating.

Additionally, the compressive and shear properties of nanoporous gold (np-Au) coated with different ultrathin metallic materials (i.e., platinum and silver) are investigated via molecular dynamics simulations. The same atomistic models generated before are used for the geometric representation of coated and uncoated np-Au structures. The role of thickness for the coating performance is examined under compressive and shear loading by comparing the mechanical characteristics of the atomistic models such as Young's modulus, yield, and ultimate strengths. Moreover, adaptive common neighbor analyses are also carried out by monitoring the evolution of the crystal structure of the specimens during the loading process. In this way, the deformation mechanisms of coated and uncoated nanoporous specimens are identified thoroughly. As a key finding from the simulation results, it is observed that the mechanical properties of np-Au are crucially dependent on the type of the coating material. However, a significant improvement on the toughness within the plastic regime is demonstrated for all types of coating materials and loading conditions.

Furthermore, the strain rate effects on the tensile and compressive properties of nano-crystalline nanoporous gold (nc-NPAu) are also investigated by performing molecular dynamics simulations. In order to examine the role of strain rate, atomistic models of nc-NPAu structures with three different grain size are generated through a novel modeling technique based on the Voronoi tessellation method. Additionally, adaptive common neighbor analysis (aCNA) is carried out to observe the evolution of the crystal structure. In this way, the deformation mechanisms of nc-NPAu atomistic models are investigated thoroughly. The findings point out that such mechanical properties as toughness, ultimate and yield strengths grow at increasing strain rates for both tensile and compressive loadings. The elastic moduli of nc-NPAu atomic models have exhibited insignificant changes for the different strain rates. Moreover, this study shows that the deformation mechanism is not only a combination of dislocation movements, grain rotations, and grain boundary sliding but also additionally grain travelling.

Finally, acoustical properties of the uncoated and coated (i.e. Platinum and Silver) nanoporous gold are investigated by performing molecular dynamics simulations. The monatomic gas in which the sound waves can propagate is chosen as Argon. The sound wave is generated by using oscillating solid wall. All acoustical analysis are carried out for only one frequency value (i.e. 2.57 GHz) and the acoustic Reynold's number R=0.5. It is demonstrated that the nanoporous specimens placed in front of the propagating sound wave absorb the sound energy although they also act as a reflector. Furthermore, dependence of sound absorption on the porosity of nanoporous material is demonstrated by utilizing different specimens with varied porosities. Findings show that the sound energy absorption capacity can be increased by decreasing the porosity of materials. It is also presented that the type of the coating material directly affects the sound absorption capacity while the coating thickness does not change the sound absorption notably.

NANO GÖZENEKLİ METALLERDE YÜZEY KAPLAMANIN MEKANİK ve AKUSTİK ÖZELLİKLERE OLAN ETKİLERİ

ÖZET

Son yıllarda ümit vaad eden fiziksel ve kimyasal özellikleriyle araştırmacıların ilgi odağında olan nano-gözenekli metal malzemeler bu tezin konusunu oluşturmaktadır. Buna göre tez kapsamında, farklı bir metal malzeme ile kaplama yapılmış nano-gözenekli metal malzemelerin mekanik özellikleri ve ses dalgalarına verdiği cevaplar, yeni ve özgün bir sayısal atomik modelleme tekniği kullanılarak moleküler dinamik (MD) simülasyonları vasıtasıyla incelenmiştir. Bu amaç doğrultusunda, kaplama etkisinin detaylı bir şekilde incelenebilmesi için farklı kaplama kalınlığı ve malzemesinin kullanıldığı değişik varyasyonlardaki atomsal modeller hazırlanarak farklı şekil değiştirme oranlarında uygulanan farklı mekanik yüklemeler (çekme, basma, kesme) ve belli bir frekans aralığında gönderilen ses dalgaları göz önüne alınmıştır ve kaplama yapılmış nano-gözenekli malzemenin mekanik davranışını belirleyen deformasyon mekanizmaları ve Young modülü, çekme mukavemeti gibi mekanik özelliklerinin yanı sıra, ses dalgalarının malzemeye olan etkisi de belirlenmiştir.

Nano-köpük malzemeler, nano ölçekte hücresel boşlukları olan gözenekli malzemelerdir. Gözenek çapları 1-100 nm arasında değişmektedir. Nano-köpük malzemelerin en önemli özelliği sahip oldukları nano-gözenek yapısı itibariyle yüzey alanı-hacim oranının çok yüksek olmasıdır. Malzeme tipine ve gözenek büyüklüğü ve topolojisine bağlı olarak nano-köpük malzemeler çok farklı mühendislik alanlarında yüksek kullanım potansiyeline sahiptirler. Katalizasyon, yüzeye tutunma (absorption), ayırma (separation), biyolojik molekül saklama ve saflaştırma, çevre kirliliği kontrolü, kimyasal sensör uygulamaları gibi pek çok uygulamada kullanabilirler. Ayrıca, yarı-yalıtkanlar, mikroelektronik, bataryalardaki elektrot malzemeleri, yakıt hücreleri, süperkapasitör ve optik cihaz geliştirme alanlarında kullanılmak üzere araştırmacıların yoğun ilgisini toplamaktadır. Bunlarla beraber, gözenekli yapıları sayesinde kendilerini oluşturan malzemenin yığın (bulk) malzeme halinden doğal olarak daha hafiftirler, dolayısıyla havacılık ve uzay gibi ağırlık azaltımının çok önemli olduğu alanlarda kullanım potansiyelleri yüksektir. Sayılan ve daha da örnekleri artırılabilecek kullanım alanlarında, nano-köpük malzemelerin etkin bir şekilde kullanılabilmesi için mekanik özelliklerinin çok iyi bilinmesi ve karakterize edilmesi gerekmektedir. Literatürde, nano-gözenekli malzemelerin mekanik özelliklerinin incelenmesi konusunda hem deneysel hem de sayısal çalışmalar az sayıda mevcuttur. Yüksek yüzey alanına sahip bu malzemelerin başka bir metal malzeme ile kaplanarak mekanik özelliklerindeki değişimin incelenmesi konusunda ise literatürde herhangi bir teorik çalışma bulunmamaktadır. Literatürdeki bu boşluğu gidermek amacıyla bu proje kapsamında, farklı metaller ile kaplanan nano-gözenekli metal malzemelerin mekanik özellikleri atomsal benzetim teknikleri ile incelenmiştir. Laboratuvar ortamında deneylerin hem pahalı hem de ilgili deformasyon mekanizmalarının

incelenmesinin zor olması nedeniyle benzetim yoluyla yapılan sayısal deneyler önemli yer tutmaktadır. Sayısal deneylerin yapılabilmesi için gerek duyulan atomik modellerin oluşturulması ise karmaşık nano-gözenek yapıları dolayısıyla oldukça zordur. Literatürde bu alandaki teorik çalışmaların azlığının en önemli sebebi de budur. Karmaşık yapılı nano-gözenekli malzemelerin atomsal modellerinin oluşturulabilmesi için geliştirilmiş yöntemler literatürde mevcuttur. Fakat, bu yöntemlerin hiçbiri kaplama etkisini modellemeye elverişli değildir. Bu projede geliştirilen yeni ve özgün bir yöntemle nano-gözenekli malzemelerin farklı bir malzeme ile kaplanmış durumdaki atomsal modellerinin edilmesi sağlanmıştır ve literatüre bu konuda önemli bir katkı sağlanmıştır.

Bu tezdeki araştırma çalışmaları genel olarak üç aşamadan oluşmaktadır. İlk aşamada nano köpük malzeme yapısı için özgün bir yöntem kullanılarak atomsal model oluşturulması için gerekli algoritmalar geliştirilmiş ve gerekli kod yazılımları gerçekleştirilmiştir. Geliştirilen bu yöntemle nano-köpük yapısını oluşturan gözeneklerin büyüklükleri ile bu gözenekleri çevreleyen ligamentlerin kesit alanı büyüklükleri doğrudan kontrol altında tutulmuştur. Buna ilaveten, geliştirilen bu yöntem ile nano-gözeneklerin farklı bir malzeme ile kaplanması durumundaki sayısal model de kolaylıkla oluşturulabilmektedir. Bu aşamadaki nihai hedef, ikinci ve üçüncü aşamada gerçekleştirilecek moleküler dinamik simülasyonları için gerekli olan rastgele yapıdaki nano köpük modellerine ait atom koordinatlarının üretilmesidir. Projenin ikinci aşamasında ise, üretilen atomsal modellerdeki boşluk oranı, ligament uzunluğu ve kesit genişliği, kaplama malzemesinin tipi ve kalınlığı gibi parametreler değiştirilerek, uygulanan çeşitli yüklemeler sonrasında nano-köpük yapısında oluşan deformasyon mekanizmaları moleküler dinamik benzetimleriyle nano ölçekte incelenmiştir. Böylelikle, farklı bir malzeme ile kaplanan nano-gözenekli malzemelerin mekanik davranışlarında görülebilecek değişiklikler, farklı parametrelerin etkisi göz önüne alınarak incelenebilmiştir. Son aşamada ise; daha önce literatürde gerçekleştirilmemiş olan nano-gözenekli malzemelerin akustik incelemesi sayısal olarak yapılarak, ses yutum katsayıları hakkında fikir sahibi olunmuştur. Bunu gerçekleştirmek için öncelikle monoatomik (tek elementli) bir gaz ortamında sesin yayılması ve sönümlenmesi moleküler dinamik benzetimleri ile gerçekleştirilmiştir. Daha sonra buradan kazanılan deneyimler ile aynı ortamda yer alan bir nano-gözenekli metalin ses dalgalarına gösterdiği cevap tespit edilmiş ve bu modelin ses yutum katsayısı hesaplanmıştır. Bu sayede, literatüre yapılan katkının yanında kullanım alanı günden güne genişleyen bir malzemenin önemli bir fiziksel özelliği hakkında da bilgi edinilmiş olunmuştur. Bunun dışında daha önceden geliştirilen modelleme tekniği ile kaplamalı nano-gözenekli metallerin de akustik analizi de gerçekleştirilmiştir. Böylelikle literatürde yer almayan kaplanmış nano-gözenekli malzemelerde kaplamanın akustik özelliklere olan etkisi ortaya konmuştur.

Çalışmamızda ana malzemeler olarak Platinyum (Pt) ve Gümüş (Ag) ile kaplamalı ve kaplanmamış nano gözenekli altın malzemeler incelenmiştir. Moleküler dinamik simülasyonları ile kaplamalı ve kaplamasız modellerin çekme, basma ve kayma analizleri yapılarak mekanik davranışları araştırılmıştır. Buna ilave olarak, kaplama malzemesi ve kaplama kalınlığının etkileri de incelenmiştir. Kaplamanın malzemeden bağımsız olarak mekanik özellikleri iyileştirdiği tespit edilmiştir. Çekme test sonuçlarında; platinyum kaplama malzemesi, gümüş kaplamaya oranla mekanik özelliklerde daha fazla iyileştirme sağladığı anlaşılmıştır. Çekme test sonuçlarının aksine basma ve kayma test sonuçları incelendiğinde de gümüş kaplama malzemesinin,

platinyum kaplamaya oranla mekanik özelliklerde artış sağladığı anlaşılmıştır. Çekme esnasında, plastik boyun verme ve kırılma ilk olarak çekme yönünde olan ligamentlerde başladığı, bu durum kayma da ise; düzlem içinde uzanan ligamentlerde gözlemlenmiştir. Basma yüklemesinde ise gözeneklerin kapandığı ve ligamentlerin kalınlaştığı gözlemlenmiştir. Genelde yükleme yönündeki ligamentlerde kümeleşen dizilim hataları ve Lomer-Cottrell kilitleri bir sonraki dislokasyon hareketliliğini engellediği ve bunun bir sonucu olarak malzemenin mukavemetini artırdığı anlaşılmıştır. Dizilim hatalarına ve Lomer-Cottrell kilitlerine kaplamalı modellerde daha fazla rastlanılır, bu da doğal olarak daha mukavemetli olmasını sağlar. Ayrıca ligamentlerin başlı başına deformasyonlarının, nano-kabloların deformasyon mekanizmaları ile olan benzerliği de ortaya konulmuştur. Bu çalışma; kaplamalı ve kaplamasız modellerin mekanik özelliklerini ve buna bağlı deformasyon mekanizmalarını anlamada faydalı bir kaynak olmuştur.

Akustik analizlere göre, hız ve basınç profilleri, yerel ses emme katsayıları tüm modeller için hesaplanmıştır. Elde edilen bulgular, nano gözenekli malzemelerin yansıtıcı gibi davranmalarına rağmen ses enerjisini simülasyon alanından emdiğini ve enerji yutma oranının nano gözenekli malzemesinin gözenekli yapısına dayandığını göstermektedir. Ek olarak, kaplama malzemeleri de ses enerjisi sönümlemesinde büyük bir rol oynamaktadır. Örneğin, Gümüş kaplamanın, Platinyum kaplama ile karşılaştırıldığında ses seviyesini azaltmak için biraz daha etkili olduğu görülmüştür. Kaplama malzemelerinin farklı kalınlıklarda olmasının ise, ses yutum performansı üzerinde kayda değer bir gelişme sağlamadığı gösterilmiştir. Yerel ses yutum katsayısı grafikleri incelendiğinde; kaplanmamış ve kaplamalı nano gözenekli malzeme modellerinin önünde büyük dalgalanmalar gözükmektedir. Bu dalgalanmalar, nano gözenekli malzeme modelinin boşluk oranı ile paralel bir şekilde artmıştır. Ayrıca, aynı porozitede fakat farklı morfolojik yapıya sahip modellerin akustik davranışlarının karşılaştırılmasında, ses yutum performanslarında kayda değer bir değişme gözlemlenmemiştir. Bununla birlikte, aynı porozite ve morfolojik yapıda fakat farklı malzeme tipine ait modeller karşılaştırıldığında Platinyum'un Altın'a oranla daha fazla ses enerjisini yutma kapasitesine sahip olduğu anlaşılmıştır.

1. INTRODUCTION

At the beginning of the 21st century, nanotechnology started to play a huge role in science. Almost all scientific fields and researches are affected by it today. Due to the nanotechnology, nowadays science has reached a level on which new functions and properties can be added to materials in order to improve new products' possibilities. Products and applications developed with the help of nanotechnology contribute a lot in to making our life easier, safer and more comfortable. For instance, some nanoparticles (i.e. chitosan, alginate, xanthan gum, liposomes, polymeric micelles, dendrimers, etc.) are used in drug delivery technology [1, 2], some other nanoparticles (i.e. 2D hexagonal boron nitride nanosheets, carbon nitride nanotubes, mesoporous silica nanoparticles, CuO, TiO_2, Fe_3O_4, $CoFe_2O_4$ nanoparticles, etc.) are used as plant growth regulator, pest control and nutrient supplies in agriculture sector [3]. Carbon based nanomaterials (Carbon nanotubes, Nanoribbons, Graphenes and Fullerenes etc.) are used in device applications for energy conversion and storage such as solar cells, fuel cells, Li-ion batteries, supercapacitors [4], etc.

Suchlike examples of nanotechnology products are numerous. This study is specifically focused on "*nanoporous metals* (NPMs)". As the name suggests, nanoporous metals contain nano-sized pores. The dimensions of these nano-sized pores vary between 1 and 100 nm [5]. NPMs have excellent functional and structural properties such as high surface area, low bulk density, good penetrability, low thermal conductivity, noise and vibration absorption, etc. Therefore they become a more popular research subject day by day.

1.1 Nanoporous Metals

As mentioned previously, the main advantage of nanoporous metals is their cellular structure at the nano scale. Due to this advantage, their material properties are superior in comparison with their bulk counterparts, which makes them potential candidates in a wide range of industrial applications such as sensors [6], fuel cells [7], actuators [8],

heat exchangers [9, 10], filters [11], energy absorbers [12, 13] and catalysts [14]. In addition, the automotive and aerospace industries are interested in NPMs as a lightweight structural material [12, 15].
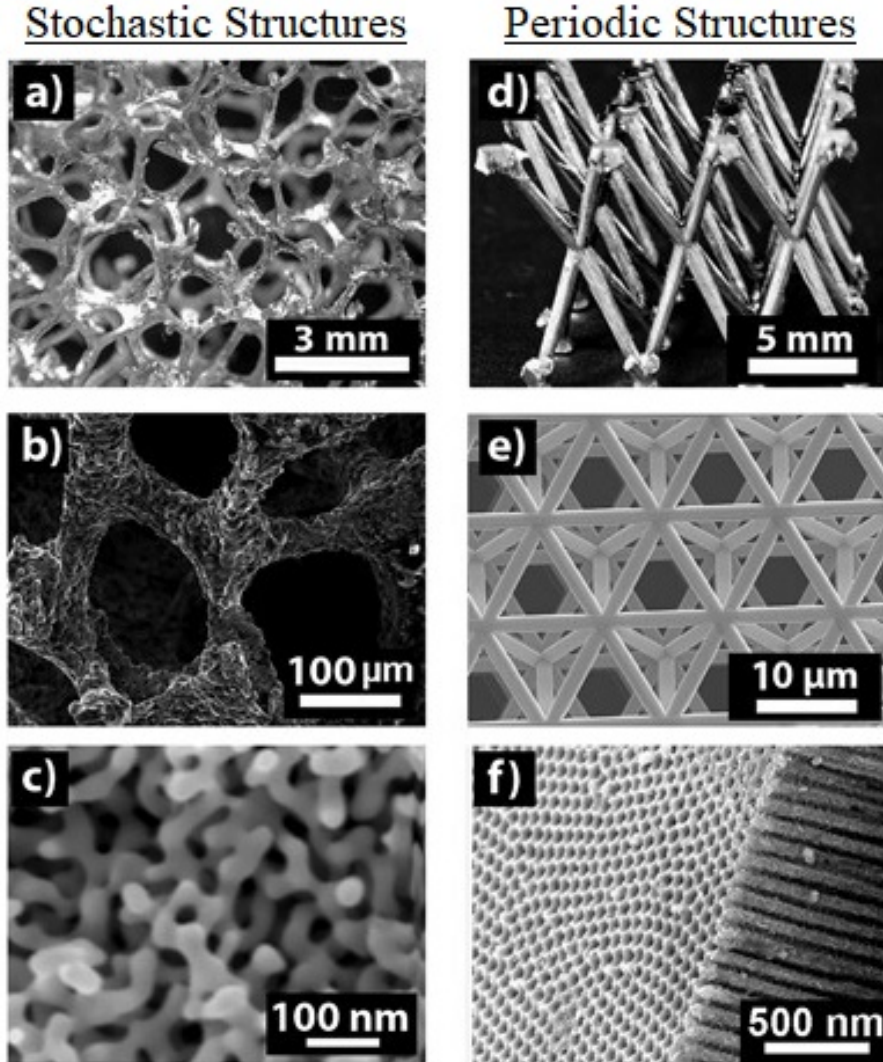
Figure 1.1 : Cellular materials, a–c) stochastic and d–f) periodic structures [11].

NPMs can be classified into two general categories as stochastic and periodic (see Figure 1.1) [11]. Stochastic structures (Figure 1.1a–c) have random pore and ligament distributions. In contrast, periodic structures (Figure 1.1d–f) have a repeated base cell such as the honeycomb in Figure 1.1f [12, 15, 16]. The mechanical properties, production effort or cost and relative density depend on the morphology of NPMs. In addition, according to the morphology these materials can be classified as open and closed cell NPMs (see Figure 1.2). Both stochastic and periodic NPMs can be fabricated with a wide variety of base metals (Copper, Aluminium, Titanium, Platinum, etc.) and open or closed cells.
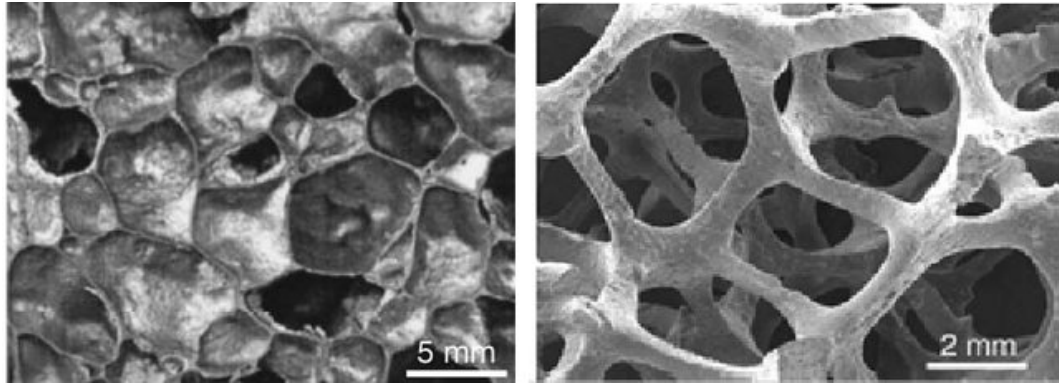
Figure 1.2 : a) A closed and b) an open cell aluminum foam [17].

The basic way to obtain metallic foam is injecting gas into molten metal [12]. The injected gas forms bubbles that become pores in the metal. Another processing method is to use powder sintering. In this method, metal powders are pressed with a metal hydride and heat-treated near the melting temperature. This process releases gas from the metal hydride and creates pores in the soft metal [12]. But this producing methods are not effective to obtain homogeneous morphology and nano-sized pores. In order to obtain nano-scaled pores in a metal, a procedure called dealloying is used. Dealloying, also known as selective leaching, is an electrochemical reaction in which the less noble component is removed from an alloy. After this process, other component forms a ligament network structure by surface diffusion. In the end, a nanoporous structure is obtained in the material. The dealloying process can be controlled by a corrosive solution and corrosion time [18]. Figure 1.3 represents the scanning electron microscope (SEM) images of nanoporous gold (np-Au) produced in different ways.
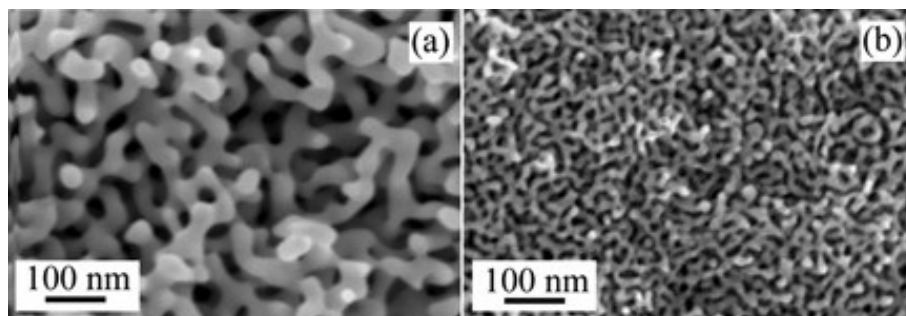
Figure 1.3 : SEM images of np-Au a) free corrosion and b) electrochemically driven corrosion [11].

Another interesting subject is the coating of a nanoporous materials with other functional materials and it helps to enhance physical or chemical properties of the former (see Figure 1.4). The common way to coat free surfaces of nanoporous

3

materials is atomic layer deposition (ALD), also known as atomic layer epitaxy (ALE). ALD can deliver a conformal coating of the nanoporous materials with well-controlled thickness [19]. That is why the application of nanoporous materials coated with different functional materials is expanding. For instance; in one of the studies, platinum coated np-Au was fabricated to investigate the fuel cell performance [20], in another study, silver coated np-Au was produced to examine its mechanical behavior [21, 22].
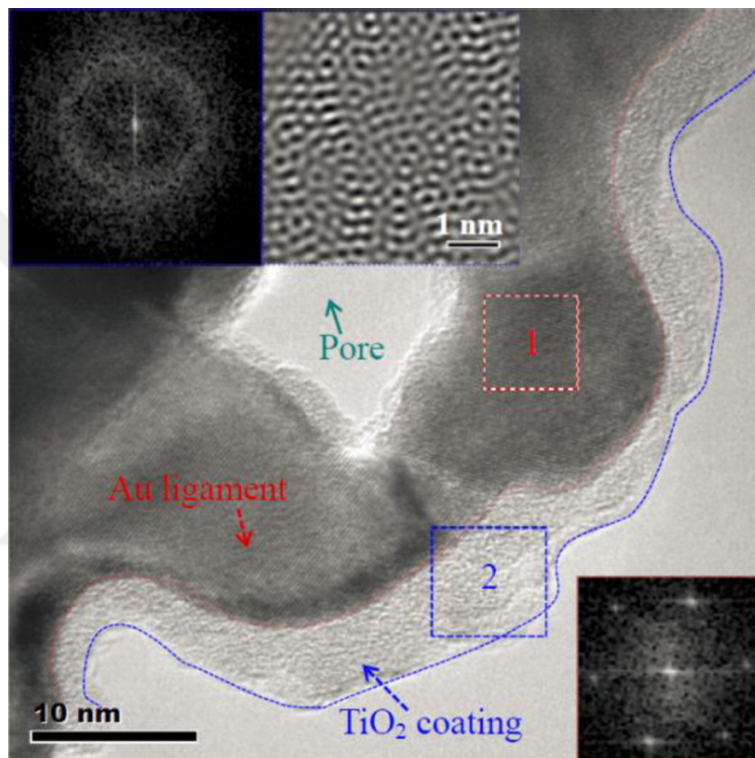
Figure 1.4 : SEM image of TiO_2 coated np-Au foam [23]

Some difficulties and high costs of performing nanoscale experiments on these nanostructures push the researchers to use computational methods such as molecular dynamics (MD) simulations.

1.2 Molecular Dynamics Simulations

Molecular dynamics (MD) simulations which are widely used to investigate the behavior of atomistic systems can be also utilized to observe the behavior of nanoporous materials. This method is used to obtain the trajectories of atoms and molecules, which interact with each other and it consists in numerically solving the equations of motions. Fundamentally, in this method atoms are considered as a point

mass, where they are interconnected with springs. In this case, the springs characterize forces between the atoms. In order to calculate these forces, the values called potentials (also known as force fields) are used. The potentials are mathematical functions for calculating the potential energy of an atomistic system with given positions in space [24].

The molecular dynamics method utilizes the law of classical Newtonian mechanics to derive the equation of motion.

$$\mathbf{F}_i = m_i \mathbf{a}_i \tag{1.1}$$

Here, $\mathbf{F}$ force, m mass, $\mathbf{a}$ acceleration and i represents each atom in the atomistic model. The positions and velocities of all atoms are calculated by using Newton's law and energy equivalence for each time step. The total energy E is the summation of kinetic energy K and potential energy U as seen in Eq 1.2.

$$E = K + U \tag{1.2}$$

In order to obtain the expected results from MD simulations, some parameters such as the atomistic model (i.e. initial positions of atoms), initial conditions (i.e. temperature, pressure, etc.), boundary conditions (i.e. periodic/non-periodic, loads) and material properties (i.e. interatomic potentials) are required. After that, the simulation continues with the positions, velocities calculations of atoms in each time step by using MD algorithms. Furthermore, other desired physical quantities are also calculated for each time step.

Verlet integration [25] is widely used to calculate trajectories of atoms in MD simulations. It is a numerical method and uses to integrate Newton's equations of motion. Thus the new positions and velocities of the atoms for each time step are calculated and the new structure of the atomistic system is determined.

Thanks to statistical mechanics, the microscopic states such as the positions, velocities and accelerations of the atoms can be converted to the macroscopic states. The macroscopic states such as temperature, pressure, energy are controlled by the statistical ensembles. NVE (Microcanonical ensemble), NVT (Canonical ensemble),

NPT (Isothermal-isobaric ensemble) are the most commonly used statical ensembles. For instance, the NVE ensemble keeps constant the number of atoms, volume and energy. In a similar way, the NVT ensemble keeps constant the number of atoms, volume and temperature. Likewise, the constant variables are the number of atoms, pressure and temperature for the NPT ensemble.

As mentioned before the interatomic potentials are used to describe the interaction between the atoms. In this context, there are a lot of potentials and methods in the literature. One of the widely used potentials is the Lennard-Jones potential (LJ) as given in Eq 1.3.

$$E = 4\varepsilon \left[\left(\frac{\sigma}{r} \right)^{12} - \left(\frac{\sigma}{r} \right)^{6} \right] \tag{1.3}$$

where E is total energy, ε is bond energy, σ is cutoff distance and r is the atomic distance. The LJ potential depicts the van der Waals forces between the atoms. Another well-known potential is the embedded atom method (EAM). The EAM potential which is given in Eq 1.4 is especially used for interactions between metals and metal alloys.

$$E_i = F_\alpha \left(\sum_{i \neq j} \rho_\beta(r_{ij}) \right) + \frac{1}{2} \sum_{i \neq j} \varphi_{\beta\alpha} r_{ij} \tag{1.4}$$

where E is total energy for an atom, F is embedded function which evaluates the motion energy between atoms, $\varphi_{\beta\alpha}$ is a function of pairwise potential, r is distance between atoms.

Although there are some limitations, such as time scale and force field accuracy, MD simulations are the best way to analyze atomistic systems. In this thesis, the MD simulations are carried out by using the open-source code LAMMPS (Large-scale Atomistic/Molecular Massively Parallel Simulator) [26, 27]. LAMMPS is a classical molecular dynamics simulator designed for clusters and desktops. Nanoscale systems such as atomic, polymeric, biological, metallic, granular, or mesoscale systems can be modeled using a variety of force fields and boundary conditions in this software.

1.3 Purpose of Thesis

The main purpose of this dissertation is to develop a novel atomistic modeling technique through molecular dynamics (MD) simulations for coated and uncoated nanoporous metals and to investigate their mechanical and acoustic behavior. Along with this purpose, in order to take into account the effect of coating elaborately, atomistic models with varying values of coating material and thickness were generated to examine mechanical loading (i.e. tensile, compression and shear) and under those conditions deformation mechanisms which dictate the mechanical properties of coated nanoporous metals such as Young's modulus, ultimate stress, yield points were determined. In addition, a unique method for generating nanocrystalline nanoporous was presented and the atomistic models of nanocrystalline nanoporous materials with different grain size were generated by the developed modeling technique. Then the generated models were subjected to tensile and compressive loading with different strain rates. Thus, strain rate and grain effects on nc-NPAu can be investigated by this way. Furthermore, the acoustic properties of the coated and uncoated nanoporous materials under a specific frequency were investigated by performing molecular dynamic simulations. For the purpose of examining the effects of coating, coated and uncoated models at constant porosity are subjected to the same sound frequency. The sound absorption characteristics are examined in a comparative manner by means of sound absorption coefficient-location graphs extracted through molecular dynamic simulations.

The obtained results constitute the content of this thesis; the atomistic modeling is in Chapter 2, the mechanical inspections are in Chapter 3-4 and the last subject acoustic is examined in Chapter 6.

2. ATOMISTIC MODELLING OF NANOPOROUS METALS

Nanoporous metals (NPMs) constitute one of the popular nanostructured material groups that attract a great deal of attention owing to their unique mechanical, physical and chemical properties. Compared with conventional bulk metals, NPMs showed several advantages. For instance, although having very low density due to their porous structure, their most distinctive property is to preserve toughness and ductility of bulk [28, 29]. Therefore these materials are of great interest especially in areas such as the aerospace and defence industry in which the specific strength quantity is highly important [29]. Besides this, nanoporous materials with a high surface-area-to-volume ratio can be used to store energy or for catalysis [30, 31]. With those extraordinary properties which are still under investigation by researchers, nanoporous materials have a notable potential to be used in a wide range of industrial applications such as insulators, energy absorbers, electrodes and sensors/actuators [32].

In literature, behaviour of NPMs is examined in several experiments including nano notch testing [33], bending of beam [34] and micro column compression [35]. The test specimens of NPMs are generally manufactured by dealloying which is a special manufacturing process. In this process, the less noble metal is removed from the metal alloy. Despite the fact that important experimental evidences regarding their physical behaviour have been exploited, most of them are conflicting [29]. As far as mechanical experiments go, it is difficult to prepare samples of nanoporous materials whose structure could be studied using an electron microscope [36, 37]. Therefore numerical experiments at atomistic or continuum scale can help to understand the experimental results and governing of new experiments. Furthermore, numerical simulation techniques play a huge role in obtaining results which are difficult to get under experimental conditions.

Regarding the mechanical behaviour of NPMs, several continuum based models exist in literature [38,39]. Among these, Gurson's model [38] presents a yield criteria which depends on porosity excluding geometrical parameters (i.e. shape and size of the

ligaments and pores) at the atomistic level. On the other hand, it has been demonstrated that the yielding phenomenon at the nano scale depends vigorously on the pore size for both face-centred cubic (fcc) [40,41] and body-centred cubic (bcc) [42] metals by using the detailed atomistic simulations. In another continuum based model that is named as the modified Gurson's model [39], the Taylor dislocation model is utilized to establish the effects of pore size on the yielding behaviour of micron- and submicron-sized voided materials while the validity of this model should be examined for nanoporous materials as also mentioned by Rodriguez-Nieva et al [29].

Properties such as stress, temperature and deformation of the systems occurring in multitudinous atoms can be obtained through atomistic simulations such as the molecular dynamics (MD) method in which empirical potentials are used. In this regard, the MD simulation technique is a suitable choice for the realization of numerical experiments of NPMs. However, there are very few numerical studies because of the difficulty to generate the atomistic models of nanoporous structures due to their randomly organized and highly complex shaped architecture.

In one of these limited number of studies, Erhant et al [36] studied the behaviour of copper and aluminium NPMs under compressive loading at high strain rates. Numerical models in this study were generated by creating randomly located spherical spaces at the nano-lattice structure.

In another study, Crowson et al [43] developed a new numerical method to generate realistic atomistic models of NPM structures by reporting the observation of the surface relaxation phenomenon after alloy discretization. In another study, Crowson et al [44] explored the morphological stability of NPMs under capillary stresses by employing atomistic simulations. In that study, atomistic models with different ligament sizes were generated by their proposed method and tested under different capillary surface stresses. As a conclusion, they reported the minimum cross-sectional diameter of the ligaments for the structural stability as 1.7 nm.

The method developed by Crowson et al [43] to generate atomistic models has been employed in several other studies. For example, Farkas et al [45] examined the mechanical behaviour of golden nanoporous materials under tensile and compressive loading through MD simulations by utilizing the atomic models that were generated

by using the method of Crowson et al [43]. The obtained results were compared with the available experimental results.

In another approach for the generation of atomistic models of NPMs presented by Kirca et al [46], an ensemble of randomly intersected spherical volumes is extracted from a bulk volume resulting in randomly oriented ligaments with non-uniform mass distribution. Using this method, To et al [47] investigated the deformation mechanisms of nanoporous aluminium materials subjected to compressive loading and demonstrate the softening behaviour by underlining the collective effects of ligaments and joints in the porous network. In a different study, by using the same atomistic modelling approach, To et al [48] examined the mechanical behaviour of nanoporous gold materials under compressive loading through MD simulations and consequently identifying three characteristic zones of deformation phases.

Recently, coating the free surfaces of nanoporous materials with different materials that can be realized by the atomic layer deposition (ALD) method has emerged as a new research area. By this way, growth of a thin film on nanoporous material surfaces with complex morphology can be maintained to improve the physical and chemical properties [49, 50]. Thus, the performance of nanoporous materials can be increased considerably in drug delivery, biological detection and filtration applications [51].

In literature, several recent studies investigated the effects of coating on the characteristics of NPMs experimentally. In this context, in one of those studies aluminium oxide was utilized as the coating material on nanoporous platinum core material by using the ALD method. In the same way, nanoporous aluminium oxide was coated with platinum to observe the chemical and physical alterations. Altogether, it was concluded that coating of the NPMs through the ALD method brought in new and excellent functional properties [52].

In another experimental study on the coating of NPMs, performance of sensing and identifying glucose molecules was explored on nanoporous golden film layers coated with copper [53]. The results of the experiments reveal that nanoporous golden film layers can be used as a bio-sensor for glucose molecules after coated with copper. In a similar experimental study, nanoporous aluminium oxide was coated with aluminium by using electro-coating and then the structure resulting from the coating process was

filled with nickel [54]. Following the examination of the samples through nano-notch experiments, it was reported that the hardness of those filled and not filled with nickel samples remained the same. In contrast with this result, Young's modulus of the samples filled with nickel was reported to slightly increased.

Even though some aforementioned experimental studies on the coating of NPMs can be found in literature, there is no numerical investigation which may help to widen and deepen the scope of the research on the coating of NPMs. The main obstacle for the realization of numerical simulations is the generation of the atomistic models of the coated NPMs. With this motivation, the ultimate goal of this study is to develop a new method for the generation of the atomistic models of the coated NPMs with periodic boundary conditions. The atomistic modelling method proposed within the study is mainly based on the standard Voronoi tessellation technique which has been previously used in many studies for the numerical modelling of cellular solids [55–57]. In addition to the standard Voronoi approach in which the cell faces are constructed as being equidistant from the seed points of their cells, other tessellation techniques which are generalized by using weighted distances or by employing more general objects (e.g. balls or line segments) as generators are also developed to extend the conventional form of Voronoi tessellation. For example, one of those generalized tessellation technics, the Laguerre tessellations technique is employed to generate stochastic geometry of the closed cell foams [58]. Furthermore, as the variants of the Voronoi and Laguerre tessellations, the other tessellation techniques such as Poisson Voronoi and Poisson Laguerre, can also be used to generate numerical models of cellular and granular structures [59]. In this regard, by using the modelling approach presented in this study, on the condition of resembling the real topology, different versions of random tessellation methods can also be used to generate the atomistic structure of nanoporous materials consisting of randomly oriented struts with non-uniform longitudinal mass distribution. The other advantage of the proposed method over the other modelling techniques is the ability to control cross-sectional dimensions and slenderness of the ligaments. In this way, effects of geometrical parameters at the atomistic level on the mechanical behaviour can be investigated for both coated and uncoated nanoporous materials efficiently. From this point of view, the method can be efficiently used by the researchers interested in computational characterization of NPMs to perform

atomistic simulations of coated NPMs, which enables one to investigate the physical characteristics of multi-functional nanoporous hybrid metals with extended features. In addition to introducing a novel atomistic modelling technique, this study also presents the effects of several parameters such as coating thickness and porosity on the thermodynamic stability of the coated nanoporous structures, which may be instructive especially for the experimental works focusing on the manufacturing of coated NPMs. Furthermore, for the purpose of validating the nanoporous models generated by the proposed method for their resembling the actual nanoporous materials, uniaxial tensile loading simulations were performed on the uncoated samples and results were compared with the experimental and numerical results from the literature.

2.1 Atomistic Modelling and Simulation Details

2.1.1 Voronoi-based atomistic modelling method

The algorithm of the modelling approach employed to generate atomistic models of coated and uncoated NPMs, which allows users to control the cross sectional dimensions (i.e. ligament size) and mass distribution along the longitudinal axes of the ligaments consists of mainly four steps as shown in Figure 2.1. In the first stage, a point cloud which is the collection of quasi-randomly located points is generated under some certain constraints. Then, in the second stage, the Voronoi tessellation technique is employed to generate line segments by using the point cloud as input data. In the following step, the line segments are converted into volumetric regions for the core and coating materials and finally those volumetric regions are filled in with the atoms created along the defined crystallographic directions.

2.1.2 Generation of random points

In order to create the line segments by using the Voronoi tessellation method, random points are required. However, it is known that the volume and shape of the Voronoi cells is dependent on the number of points per unit volume and the distance between the seed points. The degree of the randomness in the spatial distribution of the seed points is decreased by controlling the minimum distance between the Voronoi sites (i.e., dmin) to maintain a regular cell size distribution, which is partly discussed by Leonardi
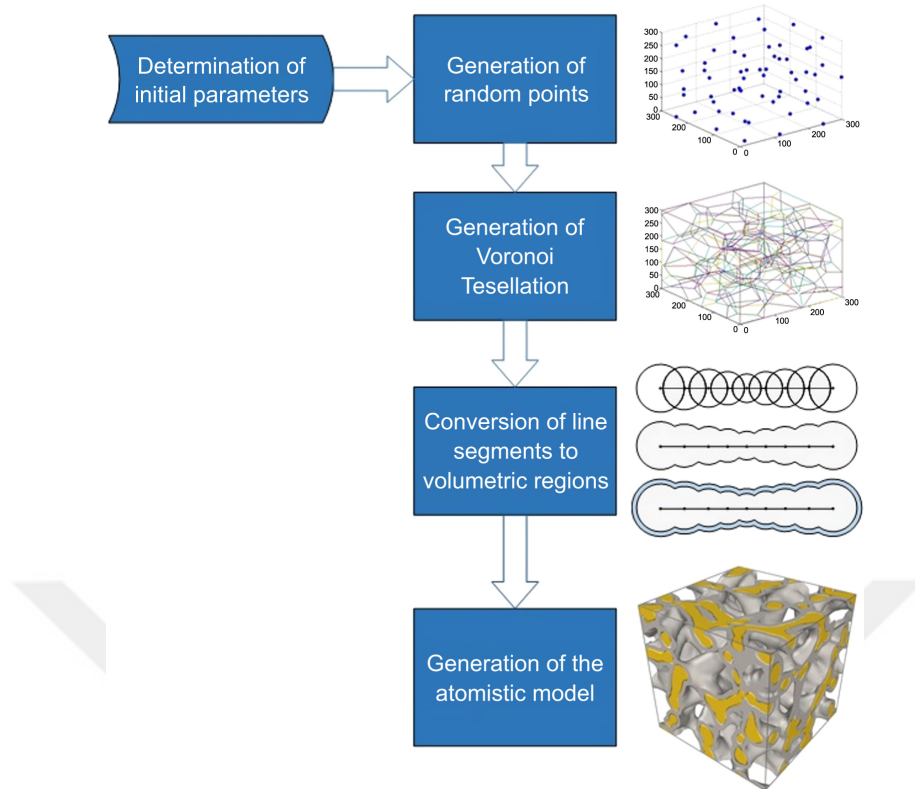
Figure 2.1 : Flowchart of the general algorithm [60].

et al [61]. Moreover, the idea of applying minimum distances between the generator points can be considered as a special case of the 'Voronoi Diagram in Laguerre Geometry' technique that is presented by Fan et al [62] and Wu et al [63]. While larger minimum distance between the seed points results in larger porosity at constant ligament size distribution, closer seed points yield smaller Voronoi cells with shorter ligament lengths. Therefore, local morphology of the nanoporous structures generated by this method is highly affected by the minimum distance between the seed points. Furthermore, boundaries of the seed points in the design space can also be constrained to obtain a porous model with desired shape. Therefore, while creating seed points that will be utilized in the Voronoi tessellation technique, minimum distance parameter is governed to control the porosity and ligament length indirectly.

In addition, for the purpose of generating periodic atomistic models, the point cloud generated for the Voronoi tessellation technique is replicated along all directions as shown Figure 2.2 [64]. After the generation of the Voronoi tessellation based on the replicated Voronoi sites, the core of the network which is corresponded to the original point seed is extracted as the periodic Voronoi skeleton that can be used in the MD
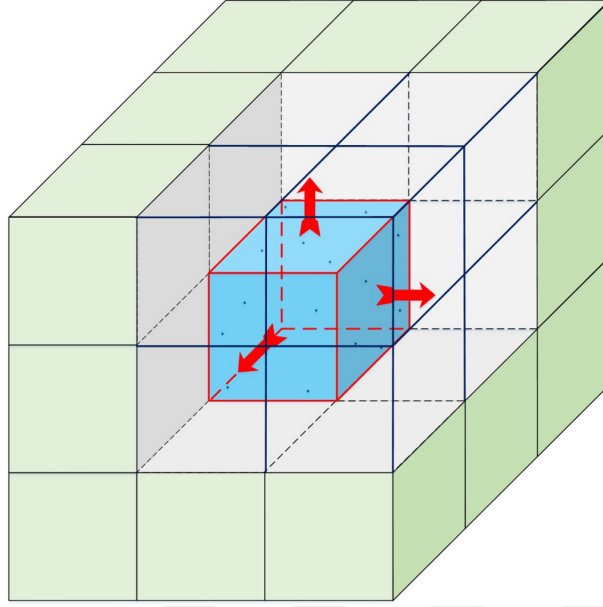
Figure 2.2 : Generation of the periodic atomistic models [60].

simulations. In this way, periodic boundary conditions can be employed efficiently to remove the size effects on the boundary surfaces of the atomistic models.

2.1.3 Generation of voronoi tessellation

The three dimensional (3D) Voronoi tessellation (VT) method, which is one of the stochastic tessellation techniques, is used to randomly divide a plane or a volume into non-overlapping sub-regions based on the distance between the seed points in a specific subset of the plane or volume [65–68]. Having different variants, the VT method has been utilized in different science and engineering fields [69, 70] such as materials science [71, 72], biology [73], astronomy [74], geography [75] and management [76]. In particular, the VT method and its variants have been widely used for the micromechanical modelling of cellular structures to investigate their mechanical properties [71, 72] as well as for the large-scale realistic micro-forming analyses of grain structures [77]. In general, a 3D Voronoi cell around a given generator seed point is specified as sub-region of space that is closer to that point than any other seed point defined for the generation of the tessellation. As a result of that, 3D space is partitioned into irregular polyhedral with flat faces and straight edges. The geometrical characteristics of the polyhedral cells including the number of cells, length of the edges and the areas of the faces can be described by their statistical distributions. In this study, straight edges of the VT models are employed to generate the ligaments of the

15
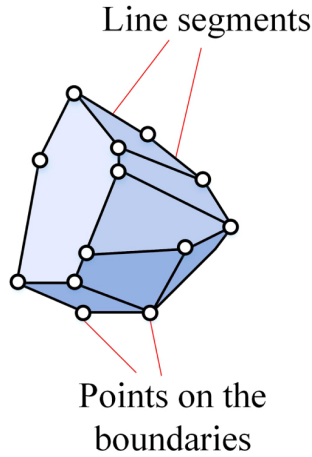
Figure 2.3 : A representative Voronoi cell [60].

nanoporous structures. There exist several open source VT codes that can generate the Voronoi cells as an output to the input of a point cloud [78–80]. In this study, as an open source code, Voro++ is used to obtain the Voronoi cells which are identified by the coordinates of the corner points and the line segments passing through those points (see Figure 2.3) [78].

Thus, as a result of this step, coordinates of the corner points and the corresponded line segment data are acquired.

2.1.4 Conversion of line segments into volumetric regions

For the purpose of generating the atomistic models of the NPMs with a specific crystal structure, a volumetric region is required. Therefore, in order to convert the line segments data into volumetric regions, volumes of which geometric centres are positioned on the line segments can be generated. In this study, spherical volumes are chosen to create volumetric regions and mass distribution of the ligaments is controlled by the radii of the spherical volumes. As mentioned before, the Voronoi Tessellation technique provides only the endpoints of line segments. Other points (i.e. central coordinates of the spherical volumes) on the line segments are calculated by using parametric line equations. If the spherical regions are created for each of the points that are determined on the line segments, individual volumetric regions appear as shown in Figure 2.4(a). At the first stage of the spherical volume generation process, the radii of the spheres at the endpoints of the line segments are determined by taking into account the lengths of all the line segments intersected at the corresponded endpoints. The radius of a sphere located at an endpoint is calculated based on the comparison
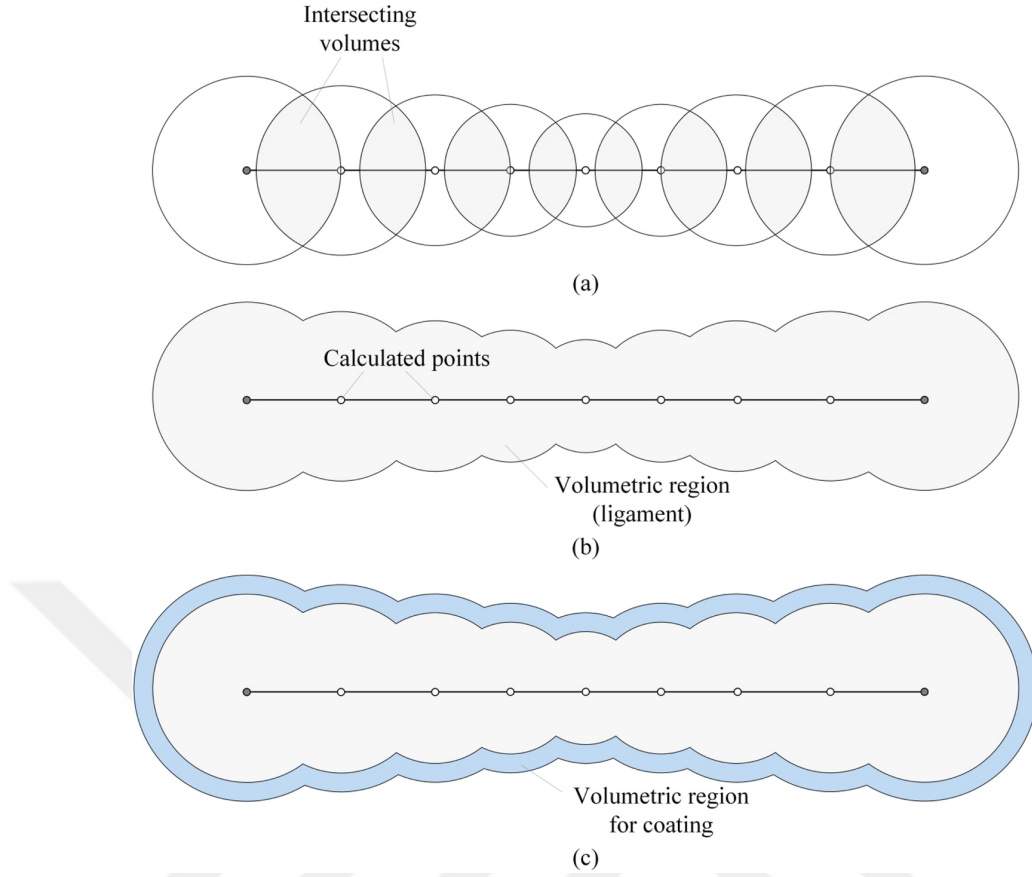
Figure 2.4 : Generating geometry of ligaments [60].

between the average and minimum length of the line segments intersected at that point for the sake of maintaining a smooth mass distribution across the intersecting line segments. After the radii of all the spheres centred at the end points, namely master radii, are established, radii of the other spheres centred on the line segments between the endpoints are calculated by linearly reducing the master radii down to the minimum radii value which can be specified according to the slenderness ratio of the ligament. Location of the sphere with minimum radius on a line segment can be easily controlled, which in turn provides more options to govern the mass distribution along the ligaments. Following the generation of all spheres, in order to create a single volumetric region, individual spherical regions are merged to remove overlapping volumes (see Figure 2.4(b)). The number of intersected spherical volumes on the same line segment can be adjusted to avoid rough surfaces at the initial atomistic configuration prior to thermalization process. As an alternative to spherical modelling, conical volumes aligned with the line segments can be utilized by defining two different radii at each end, which may be regarded as more efficient in terms of using less number of volumetric regions.

17

If the coated nanoporous model is generated, additional volumetric regions must be generated to account for the coating material. For this purpose, concentric spheres with larger radii are created at the core spherical centres previously determined. The radii of the new spherical regions must be equal to the sum of the radius and the thickness of coating. When the volumetric core regions created previously are subtracted from the new larger spherical regions, the volumetric region of coating can be obtained (see Figure 2.4(c)). For the generation of unified volumetric regions, pre-processing capabilities of several MD simulation codes such as LAMMPS (Large-scale Atomic/Molecular Massively Parallel Simulator) [26, 27], which is an open source code, can be used. Within LAMMPS, based on the data which comprise the radii of spheres and their central coordinates, volumetric regions can be created by using the command 'region' with the option 'sphere'. In case of utilizing conical volumes, the 'region' command should be accompanied with the option 'cone' by providing the axis of the cone as well as the cone radii at both ends. Then another option, namely 'union', of this command can be employed to join those spherical regions with each other to generate a single unified region. At the end of this pre-processing stage, the single volumetric region can be utilized to generate atomic coordinates of the desired metallic material.

2.1.5 Generation of atomistic coordinates

The last step of the algorithm aims to obtain the final configuration of the atomistic model. For this purpose, volumetric regions previously defined for the generations of atoms are defined within LAMMPS. The pre-processing capability of LAMMPS enables one to utilize spherical volumetric regions which may be composed of the union of simpler volumes. As the final output from the pre-processing in LAMMPS, atomic coordinates can be generated based on the selected lattice system and along the crystallographic directions. In the generation process, after the unified volumetric regions for core and coating structures are created, both core and coating atoms are generated coherently within the relevant volumes, respectively. Therefore, the crystal structure defined for the volumetric region is coherent over all ligaments. By the thermalization process applied to the atomistic configuration obtained through the pre-processing stage, roughness of the ligament surfaces due to an inadequate number

of intersected spherical regions is observed to vanish as a result of the equilibration process.

2.2 Simulation Details

In order to validate the functionality of the proposed method, several atomistic model samples of coated and uncoated NPMs were generated and examined for their thermodynamical stability via MD simulations. In this regard, Figure 2.5 illustrates two raw atomistic models at the state prior to thermal equilibration for both coated and uncoated NPMs, through which the minimum distance between Voronoi sites (dmin) is set as 100 Å. In the sample models presented in this section, gold and platinum are employed as the core and coating materials, respectively. As also depicted in Figure 2.5, the proposed modelling approach yields a nanoporous structure with randomly aligned ligaments along which a non-homogenous mass distribution is maintained, which is well matched with real structures of nanoporous materials. Furthermore, Figure 2.6 illustrates a visual comparison between the original SEM (i.e. scanning electron micrograph) image of nanoporous gold [81] and the atomistic model generated by the proposed method, which can be evaluated as a reasonable proximity between the morphology of the real nanoporous structure and the one represented by the numerical model. In addition to nanoporous gold used for the comparison in Figure 2.6, it must be mentioned that NPMs which are made with different ligament and pore size distributions can be also generated by adjusting the morphological parameters. In this regard, morphological parameters such as the number, length and Euler angles of the line segments, mass distribution along the line segments that can be traced easily within the proposed method significantly affect the physical properties of the NPMs. For instance, statistical distribution of the angle between the line segments (i.e. ligaments) and the mechanical loading direction is closely relevant with the mechanical response of the porous structure. Similarly, mass distribution along the ligaments, which directly govern the bending and axial stiffness of the ligaments, determine the mechanical behaviour of the nanoporous structure. Therefore, statistical information about these parameters is important to characterize the physical behaviour of NPMs. With this motivation, Figure 2.7 provides some statistical data for three cubic atomistic models that are generated by employing 34 Voronoi cells, while keeping the porosity constant

Model S100 - Uncoated   Model S100 – Coated (8 Å)
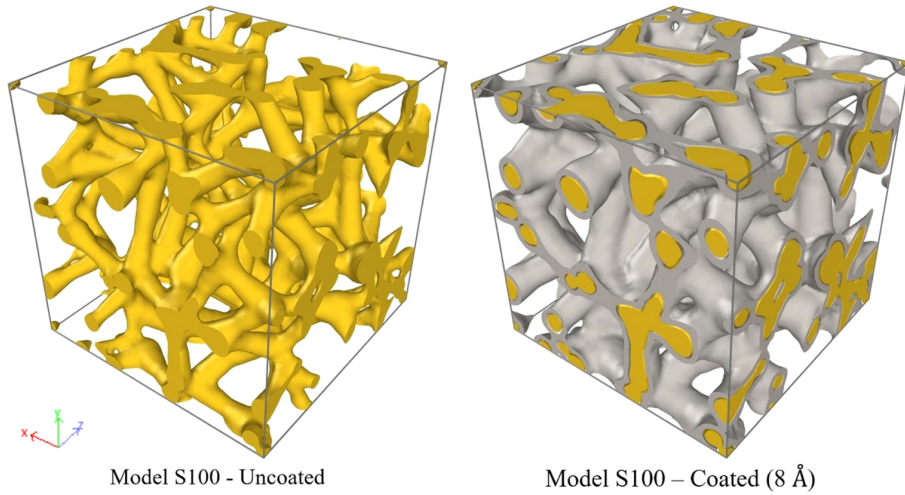
Figure 2.5 : Examples of uncoated and coated nanoporous metal models [60].

and varying the minimum distance between the Voronoi sites as 80, 100 and 120 Å. In this respect, depending on the minimum distance, the models are named as S80, S100 and S120, respectively. The dimensions of the cubic models S80, S100 and S120 are 250, 310 and 360 Å, respectively. These selected distance parameters measured between the Voronoi sites comply with the cell size that is reported as 100–10 000 Å for Au nanoporous materials in literature [82]. Moreover, in order to investigate the effects of coating thickness, these models are coated by platinum layers with different values of thickness as 8, 10 and 12 Å. Selecting those ultra-thin coating thickness values is mainly due to the limited computational resources while the ultra-thin coatings are also reported for nanoporous materials in literature [83, 84]. In addition, the minimum stable ligament size is reported as 17 Å for Au nanoporous materials in literature [44]. As shown in Figure 2.7(d), the average diameter of the ligaments within the generated models is approximately 21.3 Å for the uncoated atomistic models.

Although every Voronoi tessellation structure can be converted into the nanoporous atomistic models with the proposed method, thermodynamic feasibility of the numerical models must be ensured to demonstrate the validity of the model that is planned to be employed in the numerical experiments (e.g. MD simulations). Thermodynamic feasibility of the atomistic models is suggested by the energy profiles, because total configuration energies for the systems are minimized and remained stable over a long period of time (see Figure 2.8). In this context, free energy profiles are monitored during the thermalization process that is realized by performing classical MD simulations within LAMMPS at constant temperature (i.e. 300 K). The
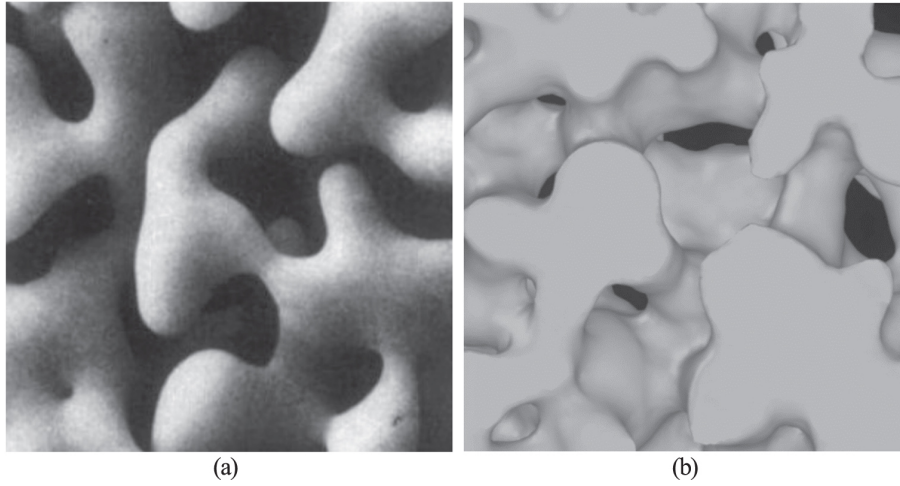
Figure 2.6 : The comparison of the SEM image of nanoporous gold with the generated model (a) SEM image of nanoporous gold [81] (b) A view of the generated model in grey tones [60].
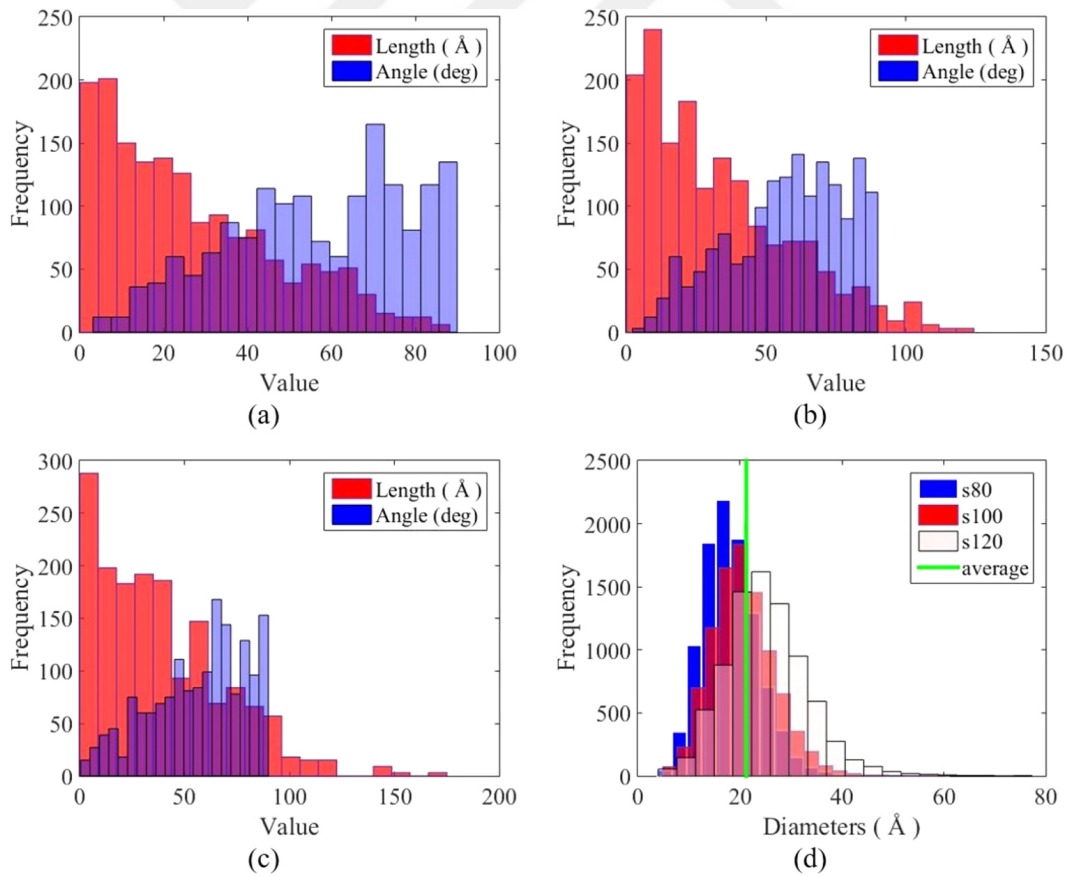
Figure 2.7 : Statistical information about the length and angular positions of the ligaments for the models; (a) model S80, (b) model S100, (c) model S120, and (d) distribution of the sphere diameters along the ligaments within the models [60].

interatomic potentials that describe the interactions between the different element types (i.e. Pt-Au) are created by utilizing the procedure of Zhou et al [85]. According to that procedure, EAM (embedded atom method) potentials for alloys can be calculated from the EAM potentials available for the single elements. Before the application of the thermalization process, static energy minimization is performed for all samples to adjust the raw atomic coordinates to the local minimum potential energy configurations. Following this, thermal equilibrium of the system is maintained at 300 K by the Nose–Hoover thermostat and isobaric ensemble (NPT) is assigned to the system as thermodynamic characteristic to keep the pressure at 0 bar. Periodic boundary conditions in all three directions are applied for all MD simulations through which the time step was set as 1 fs.

(a)

(b)
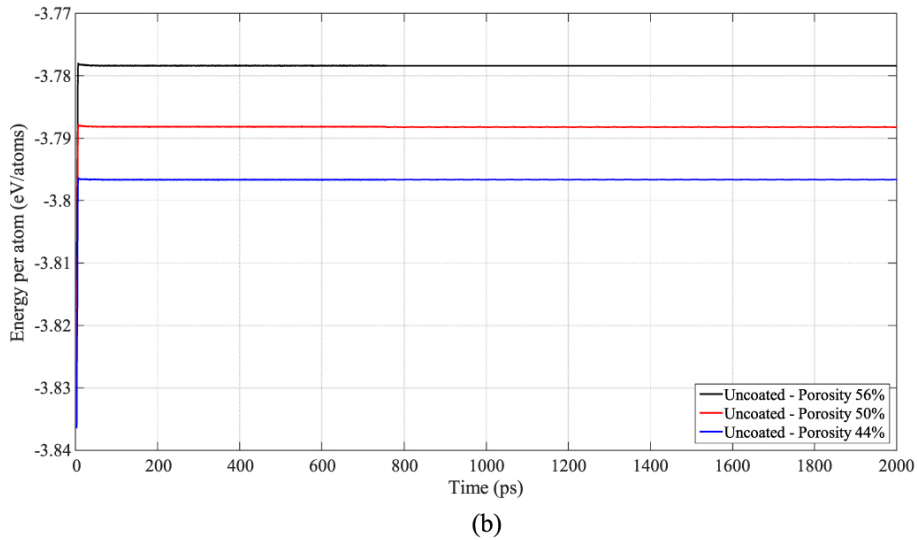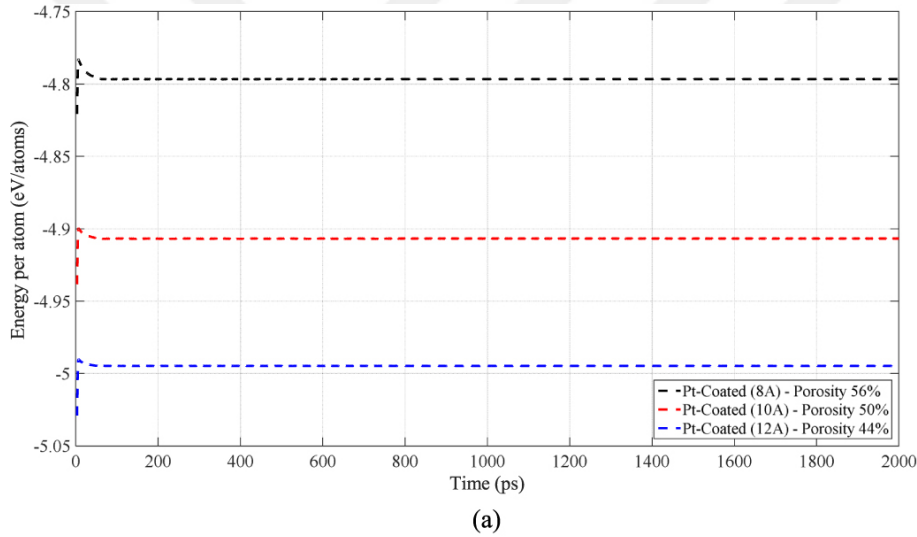
Figure 2.8 : The potential energy profiles for the coated and uncoated models for S100; (a) The uncoated models, (b) The coated models [60].

Following the thermalization step, the uncoated S100 nanoporous models are subjected to a uniaxial tensile loading along the y-direction (see Figure 2.5) with a constant strain increment of 0.1% in the NVT ensemble at 300 K temperature using the Nose–Hoover thermostat. All the atomistic models are stretched by 40% of their length (310 Å) and for each loading step, the atomic stresses are calculated by using the Virial Stress theorem [86].

2.3 Results and Discussions

2.3.1 Thermalization and stability

Figure 2.8 provides the energy profiles that are obtained through MD simulations performed for the thermal equilibration of the coated and uncoated versions of the model S100 with different coating thickness values. Initial steeper increment in the energy profile is due to the temperature increase from zero to the equilibration temperature, 300 K. Thus, the peak points are corresponded to the time stations at which the system reaches the equilibration temperature. After this point, the system is held at thermal equilibrium for a sufficiently long time period (i.e. 2 ns) to examine the thermodynamic stability. Although the energy profiles shown in Figure 2.8 demonstrate the advancement of the potential energy to the minimum energy levels within the thermalization period indicating the thermodynamic stability, it is observed that spatial atomistic arrangements prior to the thermalization, namely raw atomistic structures, experience volumetric shrinkage by coarsening of the ligaments. Those configurational alterations in the atomistic arrangements proceed with time until the minimum potential energy level is attained. Also illustrated in Figure 2.8, potential energy profiles of the all atomistic models generated with the proposed method reach to a minimum energy level. However, a close examination of the minimized configurations proves the coarsening of the models as a result of shrinking that is attributed to the surface relaxation phenomenon, which affects the mechanical stability of nanoporous materials with small ligament sizes, and that is also reported in several experimental studies [87–91].

Because of the fact that the raw atomistic models which are generated directly from the conversion of Voronoi tessellations do not incorporate any physical interpretation

of the atomic mass distribution, it is not surprising that the thermalization process modifies the spatial arrangement of the atomistic model to attain the minimum energy configuration. In accordance with this, some of the sample atomistic models exhibit a significant shrinking mechanism which is formed mainly by the decrease in pore volume and then integration of the neighbour ligaments to exploit larger ligaments (see Figure 2.9). Figure 2.9 illustrates the time evolution of a cross sectional view taken from the coated and uncoated samples that are generated by employing the same Voronoi site distance of 100 Å (i.e. S100) and maintaining the same porosity (i.e. 56%). It is obviously observed that within the thermalization process, the structural topology of the models can preserve their initial atomic configuration substantially. However, a careful comparison between the coated and uncoated sections indicates that the coated model presents a larger change in the cellular topology compared to the uncoated model, which can be referred to the tendency of the atomistic configurational change due to coating.

In order to reveal the effect of coating, adaptive common neighbour analysis [92–94] is also carried out for the coated and uncoated models. Stacking fault regions were identified based on the error in the local atom coordination as evaluated by using adaptive common neighbour analysis. For example, stacking faults that are attributed to the HCP atoms [95] can be determined and therefore the amount of HCP atoms can give information about the density of stacking faults. In this regard, the sequence of snapshots taken from the thermalization process of the models (i.e. the coated and uncoated S100 models-56% porosity) are shown in Figure 2.10. According to this, the coated model includes more stacking faults than the uncoated model, as a result the Lommer–Cottrel dislocation locks [96] can be encountered in the coated models enhancing the mechanical response of the coated models. In literature, Lommer–Cottrel locks are reported to be formed in the tensile deformation of the nanoporous aluminium structures [97] as a provider resistance to fracture of ligaments. Therefore, it can be concluded that while a very slight effect of coating is observed for the stability of the cellular topology, a more apparent modification on the mechanical properties of the nanoporous structures can be obtained by coating.

Another parameter affecting the configurational stability is the porosity of the model that can be managed by either controlling the ligament size or minimum Voronoi
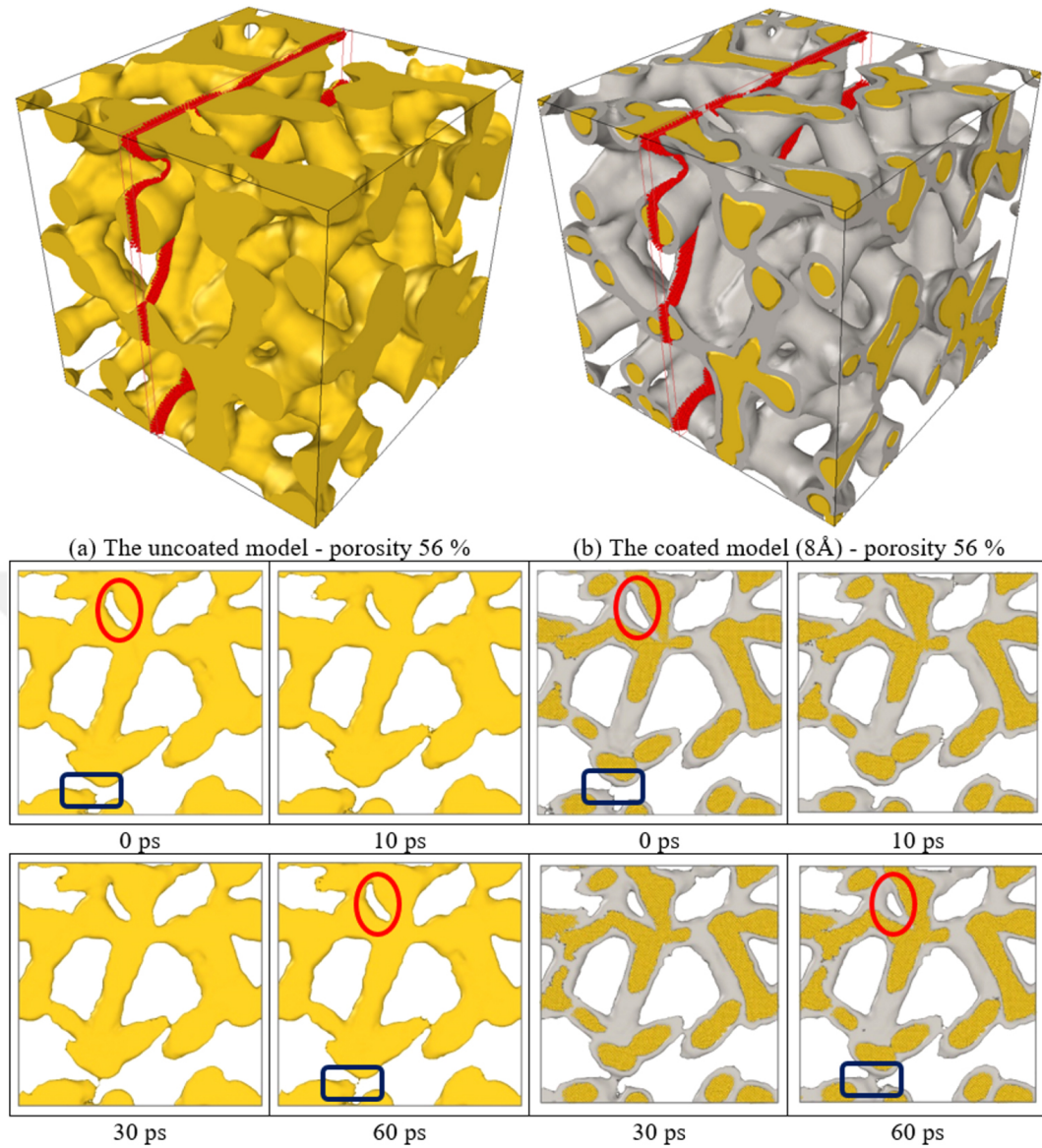
Figure 2.9 : Evolution of the cross sectional slices of the uncoated and coated model with 8 Å (56% porosity) [60].

distance. Figure 2.11 presents the structural evolution of two sample atomistic models built upon the same Voronoi skeleton (dmin = 100 Å) but different ligament sizes. The energy profiles of three models with different porosities (i.e. 40%, 60%, 80%) for the thermal equilibration process are also shown in Figure 2.12. Based on the comparison between the energy profiles and the structural evolution of the sample models, it is observed that the difference between the energy values at the peak and the plateau zones of the energy profile graphs is closely related with the magnitude of shrinking. In a quantitative manner, the percentage values for the surface shrinkage of the atomistic models are determined as 4.0, 0.90 and 0.90% for the porosities of 80, 60 and 40%, respectively. According to this, the model with larger ligament sizes
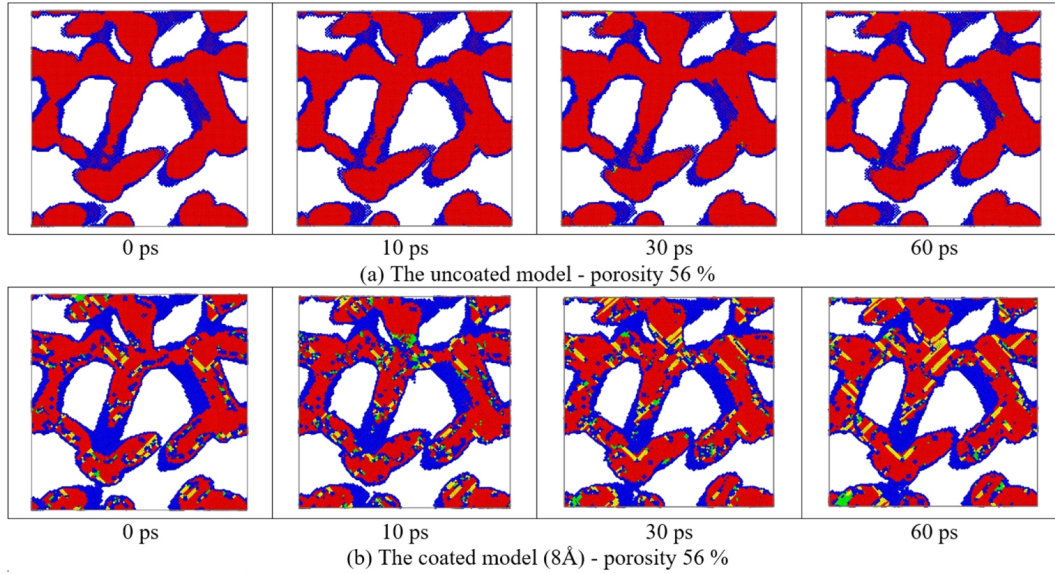
Figure 2.10 : A sequence of snapshots showing the adaptive common neighbour analysis during thermalization (red for fcc (face centred cubic) atoms, green for bcc (body-centred cubic) atoms, yellow for hcp (hexagonal close packed) atoms, and blue for indefinable atoms) [60].

(i.e. lower porosity) shows higher structural stability relative to the model with higher porosity. Similar results are also obtained for the other atomistic models generated by different Voronoi site distances (i.e. S80 and S120).

For the purpose of examining the effect of minimum Voronoi site distance (i.e., dmin) on the structural stability of the atomistic models, three different uncoated sample models are prepared by changing only the minimum Voronoi site distance as 80, 100 and 120 Å with the same porosity and same number of Voronoi cells. Minimum Voronoi site distance directly affects the Voronoi cell size, which in turn helps to control the cell size of the nanoporous structures. Energy profiles obtained through thermal equilibration of these models are shown in Figure 2.13. According to that, by comparing the peak and plateau energy differences, larger site distances provide higher structural stability.

2.3.2 Mechanical behaviour of nanoporous models

As a result of MD simulations of the uniaxial tensile loaded nanoporous gold samples, which were performed for the purpose of validating the correspondence of the atomistic models generated in the study with real nanoporous structures, effective Young's modulus (i.e. Enp/Ebulk where Enp and Ebulk are the Young's moduli of

(a) The uncoated model - porosity 80 %   (b) The uncoated model - porosity 60 %

0 ps   5 ps   0 ps   5 ps

10 ps   60 ps   10 ps   60 ps
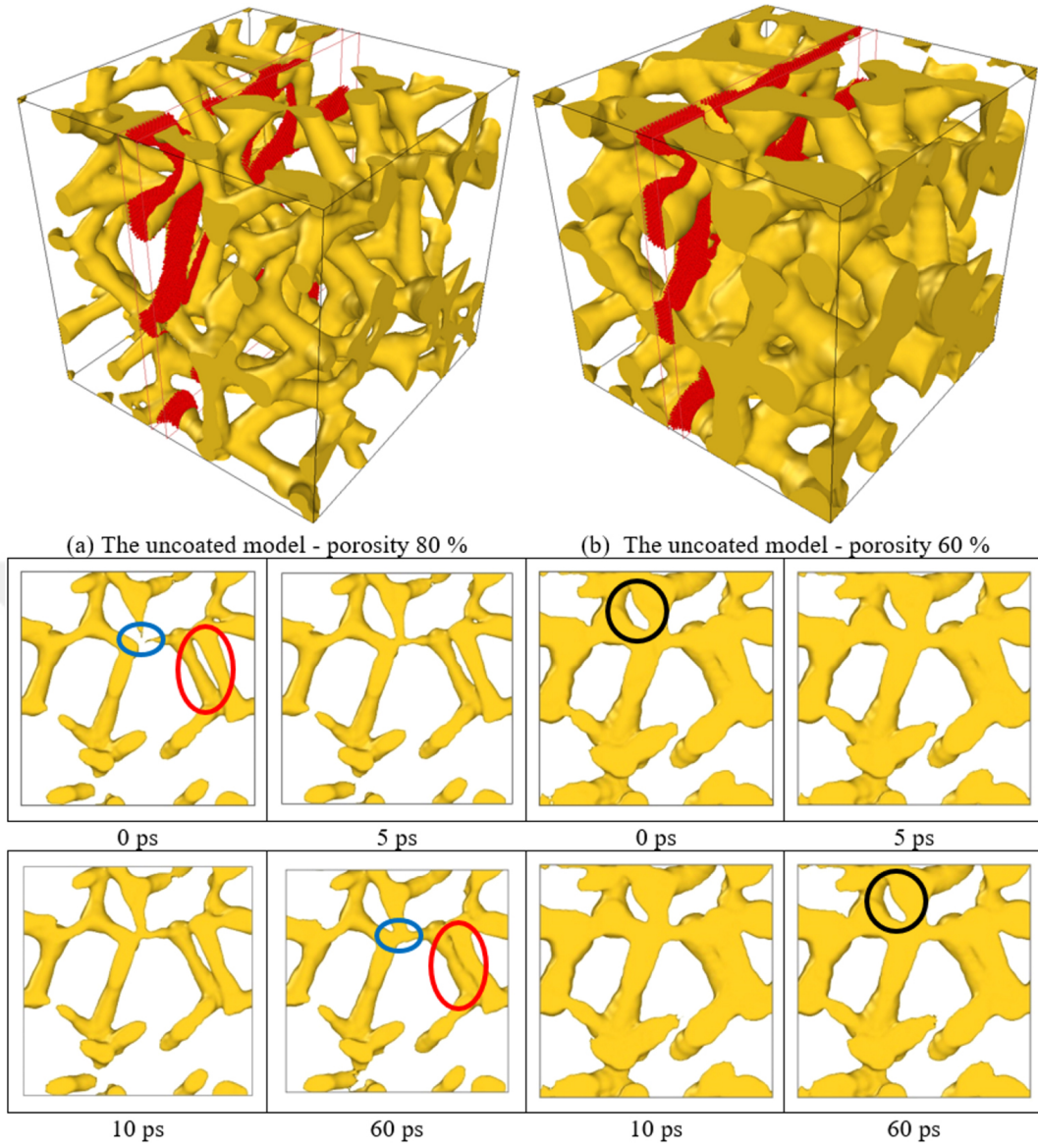
Figure 2.11 : Equilibration shrinkage of the uncoated models with porosity of (a) 80% and (b) 60% [60].
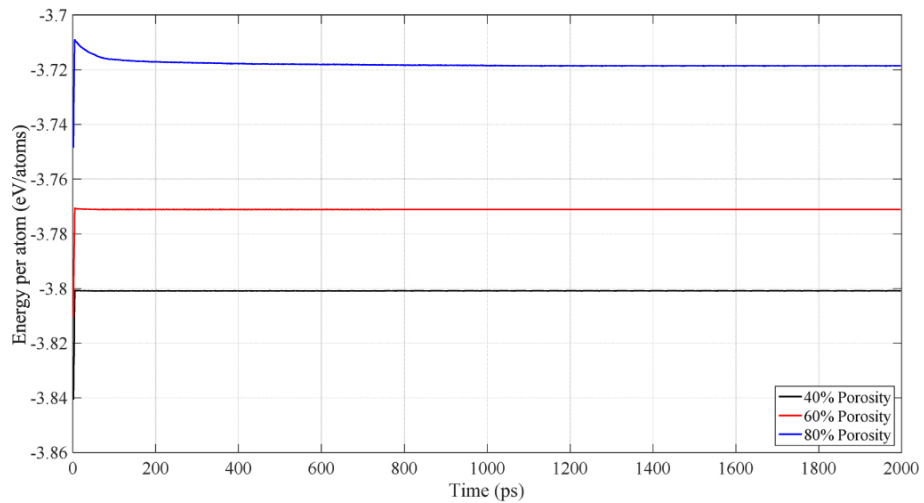
Figure 2.12 : Thermal equilibration energy profiles for different porosities of the model S100 [60].

27
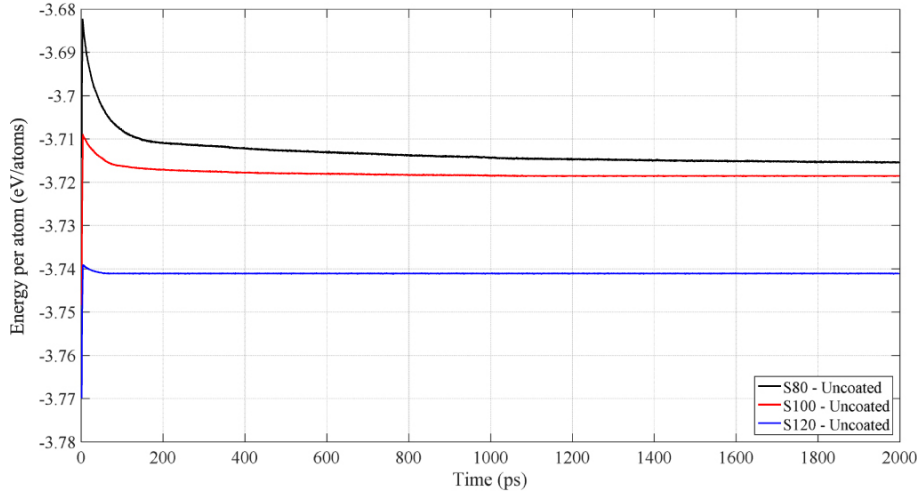
Figure 2.13 : Thermal equilibration energy profiles for the models with different minimum Voronoi site distances at constant porosity (i.e., 80%) [60].

the NPM sample and the bulk material of which NPM is made) values are evaluated and compared with the experimental and numerical results reported in literature.
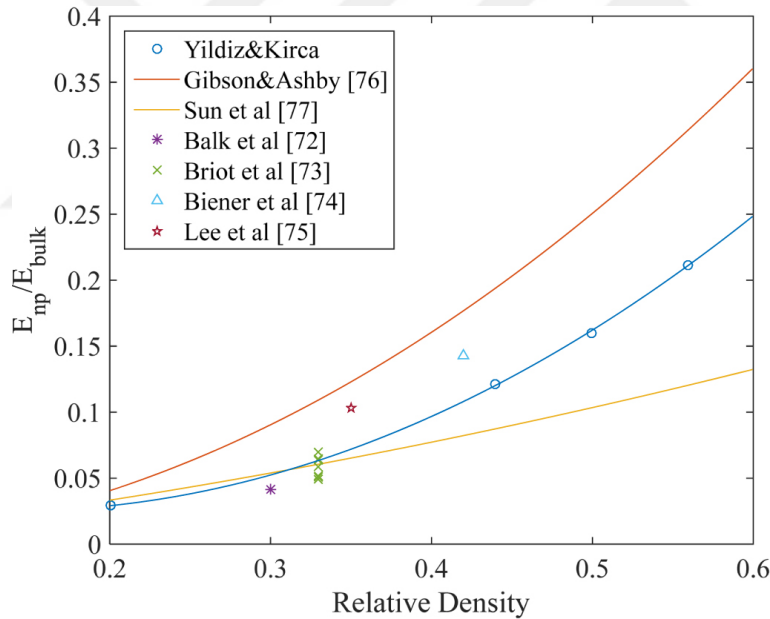
Figure 2.14 : Relationship between the effective Young's modulus and relative density [60].

In this regard, Figure 2.14 presents the data for the variations of the effective Young's moduli as a dimensionless parameter with respect to the relative density. Relative density values of the four samples used for the tensile loading simulations are 0.2, 0.44, 0.5 and 0.56. The experimental data for the effective Young's moduli that are found from the studies of Balk et al [98], Briot et al [99], Biener et al [100] and Lee et al [101] are shown as discrete points while the scaling law of Gibson and Ashby [102], which is well-known for open-cell foams and also commonly applied to NPMs, together with

28

the scaling law developed by Sun et al [103] are shown as curves. The parallelism with the Gibson–Ashby curve and the agreement with the experimental studies supports the reliability of atomistic models generated using the proposed approach.

3. THE MECHANICAL BEHAVIOR OF ULTRATHIN COATED NANOPOROUS GOLD

Due to their superior physical and chemical properties, it is noticed that research interest on nanoporous (np) materials which have great potential to serve as sensors [6, 8], electrocatalysts in fuel cells [7], catalysts [14] and actuators [104] is increasing day by day. Among different research subjects, depending on the fact that morphological properties of nanoporous metals (NPMs) significantly affect the functionality and performance [105] researchers attempt to control not only the porosity but also the pore and ligament size of the np structure [106]. In addition, another interesting issue is the coating of a np materials by another functional material to enhance their physical or chemical properties [20–22, 107]. At this point, it is vital to understand the mechanical characteristics of coated np materials for the efficient utilization in practical applications. However, it is both difficult and expensive to monitor the details of the deformation mechanisms within coated np structures experimentally [108]. Therefore, numerical techniques such as molecular dynamics (MD) simulations enable researchers to perform virtual mechanical tests on np specimens coated with different materials.

On the other hand, generating the atomistic models of the np structures, which is required for numerical simulations, is a seriously demanding work due to their complex bicontinuous morphology. In literature, there exist several methods developed for the atomistic modeling of np structures to be employed in numerical simulations. For instance, a phase field method [109] imitating the decomposition of a binary fluid mixture of two components is frequently used to obtain np atomistic models by solving the Cahn-Hilliard equation which describes the spinodal evolution of the decomposition [110]. In addition to that, within the context of another method presented by Kirca et al. [46] an ensemble of quasi-randomly distributed spherical volumes that are intersected with each other is extracted from a bulk volume to yield a bicontinuous cellular network formed by randomly oriented ligaments with non-uniform mass distribution. Recently, a new method based on the Voronoi

tessellation technique for generating realistic atomistic models of np materials has been presented by Yildiz and Kirca [60]. In addition to the advantage of being able to control the porosity, ligament size, and mass distribution along the ligaments, by the utilization of this method, coated np models with desired coating thickness can also be generated. There are numerous studies focusing on the mechanical behavior of both np and bulk crystalline materials. For instance, the mono-crystalline copper with and without defects is examined by Zhan et al. [111] through simulations of tension and nanoindentation. They report that Young's modulus is insensitive to surface and centro-plane defects, while the yield strength decreases significantly due to defects. In addition, Sun et al. [103] develop scaling laws for the mechanical properties of nanoporous gold (np-Au) by performing molecular dynamic simulations to understand the deformation mechanisms of np-Au subjected to tensile loading. Along the same line, Winter et al. [97] investigate the failure mechanisms of nanoporous aluminum (np-Al) by developing the scaling laws for the mechanical properties including Young's modulus, yield strength, and ultimate strength as functions of relative density and ligament diameter. Furthermore, To et al. [47] analyzed the mechanical behavior of np-Al materials with ultra-thin ligaments subjected to compressive loading through molecular dynamic simulations. They reported the softening behavior by underlining collective effects of ligaments and joints in porous network by using atomistic models which are generated by utilizing the stochastic modelling technique developed by Kirca et al. [46]. In another study, by using the same atomistic modelling approach, Giri et al. [48] investigated the deformation mechanisms of open-cell np-Au materials under compressive loading and identify three characteristic deformation phases: linear elastic, work hardening, and densification regimes.

There are also several studies all of which are experimental for the investigation of coated nanoporous materials. In one of those studies, Zeis et al. [20] fabricated platinum coated np-Au and investigated the characteristics of its fuel cell performance. Moreover, Ding et al. [14] presented the characterization of platinum coated np-Au structures by providing information about the manufacturing process. Another noteworthy study presented by Hodge et al. [21] focuses on the fabrication of silver coated np-Au using the method described by Chan et al. [22]. In their study, the morphology of the fabricated np material was also examined, and nanoindentation

32

testing was performed for different samples to demonstrate the effect of coating on the mechanical properties.

With the motivation of that there is no theoretical study about the effects of coating on the behavior of np materials, the main objective of this study is to investigate the effects of coating thickness and material type on the mechanical characteristics of np structures by utilizing molecular dynamics simulations. For the purpose of understanding the effect of coating material types, two different materials (i.e., Platinum - Pt and Silver - Ag) are examined as coating materials while the core material is selected as gold. By utilizing the atomistic modeling technique developed by Yildiz and Kirca [60] numerical specimens for the coated np structures are generated. Then, for each specimen with different coating thicknesses and materials, mechanical tests are performed to investigate the tensile, compression and shear behavior using the classical molecular dynamics simulations. Furthermore, in order to explain the mechanical behavior illustrated by stress-strain curves, adaptive common neighbor analyses (aCNAs) are carried out for the all coated and uncoated specimens, and deformation mechanisms are scrutinized by monitoring the evolution of the crystal defects in the deformation process.

3.1 Modeling and Simulation Details

3.1.1 Generation of atomistic models

As mentioned previously, the atomistic models of the coated np structures are generated by using the method proposed by Yildiz and Kirca [60]. This method consists of mainly four steps. In the first step, a point cloud is generated quasi-randomly with a certain control on the distance between the seed points. In order to generate periodic atomistic models of the np materials, the point cloud generated for the Voronoi tessellation technique is replicated as described in Ref. [64]. In the second step, line segments are generated from the point cloud data by using Voronoi tessellation technique. After the generation of the Voronoi skeleton, the core of the network which is corresponded to the original replicated point seed is extracted as the periodic np model that can be used within MD simulations. Then, in the following step, the line segments are converted into volumetric regions which are used to create the

atoms in preferred crystallographic organization for coated and uncoated np materials. Here, it should be mentioned that same crystallographic directions (i.e., [001]) are employed for the coating and core materials. After the coordinates of the atoms within the volumetric regions are determined for coating and core materials, these raw atomistic models are thermally equilibrated through molecular dynamics simulations to reach thermodynamically stable configurations, which can be employed in further mechanical simulations. For more detailed information about the atomistic modelling method, Ref. [60] can be reviewed.

In this study, three different atomistic models, called v01, v02, and v03, are generated to consider the effects of randomly oriented ligaments. The dimension of the cubic models is 310 Å. Beside this, the atomistic models are coated with Platinum (Pt) and Silver (Ag) with different coating thicknesses (i.e., 8 Å, 10 Å and 12 Å) to investigate the dependence of the mechanical behavior on the coating thickness. The main reason for selecting those ultra-thin coating thickness values is the limited computational resources while the ultra-thin coatings are also reported for several nanomaterial systems in literature [83, 84]. In one of these studies [83], gold nanoparticles are encapsulated with ultra-thin silica coating via a kinetically controlled process. In another study [84], ultra-thin coating processes for micro-electro-mechanical systems (MEMS) are described by demonstrating the applications of chemical vapour deposition (CVD) and atomic layer deposition (ALD) for the growth of ultra-thin films on polycrystalline silicon microstructures. The objective of these coating processes is declared to improve the reliability and performance of these microstructures.

For the purpose of illustrating the morphological characteristics of three numerical specimens, some statistical data are provided in Figure 3.1. By this way, distributions for the diameter, length, and angular orientation of the ligaments with respect to the loading direction (i.e., the y-direction) together with the number of atoms and the porosity of the atomistic models are given for each specimen. In this regard, all three specimens have approximately the same average ligament diameter, which is 22 Å [see Figure 3.1(d)], while minimum stable ligament size is reported as 17 Å for Au np materials [44].

Figure 3.1 : Statistical information about the length, diameter, and angular positions of the ligaments for the models: (a) Version-01, (b) Version-02, and (c) Version-03. (d) Distribution of the sphere diameters along the ligaments within the models. (e) Porosity and the number of atoms of the models.
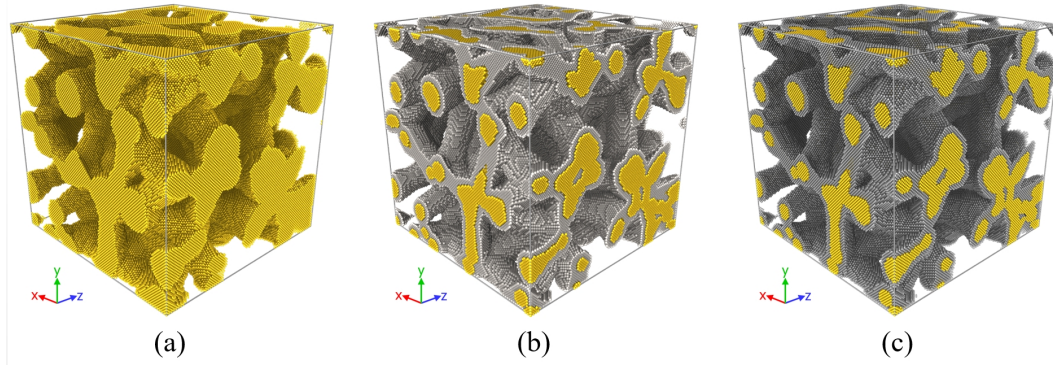
Figure 3.2 : Atomic configuration of the uncoated and coated np-Au sample: (a) the uncoated np-Au, (b) 8 Å platinum coated np-Au, and (c) 8 Å silver coated np-Au [112].

3.1.2 Simulation techniques

Classical molecular dynamic simulations are performed to investigate the deformation mechanisms of coated and uncoated np materials subjected to tensile loading by using the open-source code LAMMPS [26, 27]. The interatomic potentials employed to describe the interactions between the different element types (i.e., Pt-Au and Ag-Au) are created by following the procedure of Zhou et al. [85]. According to that procedure, Embedded Atom Method (EAM) potentials for alloys can be calculated from the EAM potentials of the individual elements. Periodic boundary conditions in all three directions are applied for all MD simulations for which the time step is set as 1 fs.

In order to initialize the atomistic specimens for a simulation run, a conjugate gradient technique is utilized to perform local energy minimization. After that, all the models are thermally equilibrated at 300 K for 60 ps by using the integrator of NPT (isothermal-isobaric) ensemble before applying the tensile loading. As an example, in Figure 3.2, an atomic configuration of the np-Au sample coated with 8 Å platinum after the thermal equilibration process is depicted. Following the thermalization step, each np sample is subjected to a uniaxial tensile loading along the y direction with a constant strain increment of 0.1% under NVT canonical ensemble with Nose-Hoover thermostat. All atomistic models are imposed until the strain reaches 0.40 and for each loading step, the atomic stresses are calculated by using Virial stress theorem [86]. In addition, the adaptive common neighbor analysis (aCNA) [93, 94] which is a computational analysis method to determine local

atomic arrangements in large-scale atomistic simulations of crystalline solids, is also performed to understand the deformation mechanisms of ligaments by monitoring the evolution of the microstructural defects within the np structure. As a result of the adaptive common neighbor analysis, atom types are colored differently [i.e., red for Face Centered Cubic (fcc) atoms, green for Body-Centered Cubic (bcc) atoms, yellow for Hexagonal Close Packed (hcp) atoms, and blue for free surface atoms] to understand the crystallographic structure and stacking faults. For instance, one type of the stacking faults can be identified as the hcp-like coordination observed in fcc structures [95].

3.1.3 Validation of the atomistic model

Reliability of the atomistic models generated by the Voronoi tessellation technique is examined by comparing the results obtained from the uniaxial tensile tests of uncoated np-Au models with the experimental [98–101, 113] and numerical [103] results reported in literature. For this purpose, atomistic models with different porosities (i.e., 0.2, 0.44, 0.5, and 0.56) are prepared and corresponding effective Young's modulus values (i.e., E_{np}/E_{bulk}, where E_{np} and E_{bulk} are the Young's moduli of nanoporous and bulk gold material, respectively) are determined by using the stress-strain data constructed through MD simulations. For the purpose of comparing the results to validate the acceptability of the atomistic models, Figure 3.3 presents the variation of the effective Young's moduli with respect to the porosity. In this regard, two scaling laws developed by Badwe [113] and Sun et al. [103] are depicted as continuous curves owing to their functional nature while the experimental results found from literature are shown by discrete data points. Considering the fact that for both experimental and numerical studies on the np materials highly depends on the geometry, crystallographic direction and structure, strain rate, surface-area-to-volume ratio, and ligament size, Figure 3.3 presents an adequate approximation to the available data in literature for np-Au. It is also noticed that the numerical results obtained from the proposed atomistic modeling technique are very satisfactory, especially at the low relative density. Furthermore, as a quantitative note, the range of Young's moduli calculated for the specimens generated by the proposed method is in the range of 9–17 GPa while the Young's modulus values of np-Au in literature are reported to
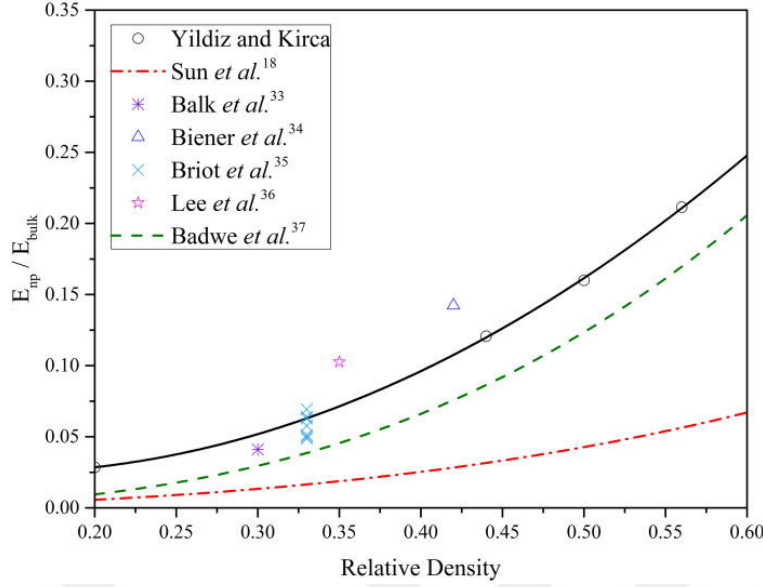
Figure 3.3 : Relationship between the effective Young's modulus and relative density [112].

be approximately in the range of 6–12 GPa [90, 100] which designates an acceptable correspondence of the atomistic models to the real np materials. As a result of that, it is concluded that the degree of the reliability of the atomistic models is shown to be sufficient for the further investigations about the effects of coating on the mechanical properties of NPMs.

3.2 The Tensile Behavior of Coated Nanoporous Gold

3.2.1 Effect of coating on the stress-strain behavior

As a result of MD simulations performed for the uniaxial loading of the atomistic models, stress-strain curves are constructed to demonstrate the effects of coating on the mechanical characteristics of np materials. In this regard, Figures 3.4(a) and 3.4(b) present the stress-strain curves of the uncoated and coated models with different porosities for platinum and silver coating, respectively. It is clearly noticed that both of the coating materials (i.e., platinum and silver) enhance the mechanical properties of np-Au such as Young's modulus and ultimate strength. For instance, as a quantitative note, when the np specimens are coated to a thickness of 8 Å, the ultimate tensile strength increases from 454 MPa to 604 MPa and to 493 MPa for platinum and silver, respectively. Furthermore, it can also be noted that the general trend of the stress strain curves are all similar in the manner of that a distinct linear regime is followed by the

38

yielding of the specimen. After the ultimate tensile strength point, all the specimens exhibit a softening behavior that is also reported by To et al. [47]. In order to eliminate the effect of porosity on the mechanical properties, both coated and uncoated samples are prepared to have the same porosity. As a result of comparison between the coated and uncoated models, it can also be conceived that by increasing the coating thickness, Young's moduli, ultimate tensile, and yield strengths of the np specimens increase systematically for both of the coating materials (i.e., silver and platinum).

In addition, while the improvements on the yield and tensile strength characteristics are more distinctive, especially for the Pt-coated np specimens, the enhancement on the elastic modulus values seems to be less remarkable and is approximately the same for both Pt- and Ag-coated specimens. However, owing to its much higher elastic modulus, coating with Pt can be expected to provide more significant improvement on the Young's modulus of np-Au. This observation can be explained by examining the crystal structure of the specimens. According to that, there is an obvious difference in the number of atomic defects noticed after thermalization, especially in Pt-coated models, which is elaborated thoroughly in Sec. 3.2.2. There are several factors affecting the initiation of those atomic defects. The first one is the pre-existing nano voids between the coating and the core materials due to different lattice constants (i.e., a_{Au}=4.0801, a_{Pt}=3.9200, and a_{Ag}=4.0896). As it is also known from previous studies, the nano voids have a reducing effect on yield strain [114]. Because of the larger difference between the lattice constants of gold and platinum, high strain concentrations, especially in the vicinity of the coating interface, are observed in platinum coated models, which results in dislocation emission from the free surfaces of voids. The second factor is the inward surface relaxation phenomenon which causes stress flow from the surface of the material to the inner region, stimulating the nucleation of dislocations starting from the surface. As also reported in literature [115], the surplus surface energy of platinum is a driving factor for the increase of dislocation density in platinum coated models. The other factor that may be affecting the formation of atomic defects within the coated samples is the difference in thermal expansion coefficients of coating and core materials. In this regard, higher density of dislocations observed for the coated models can be attributed to the difference between the thermal expansion coefficients of Au, Ag, and Pt which are 14.2, 18.9, and 8.9 (10^{-6}/K),
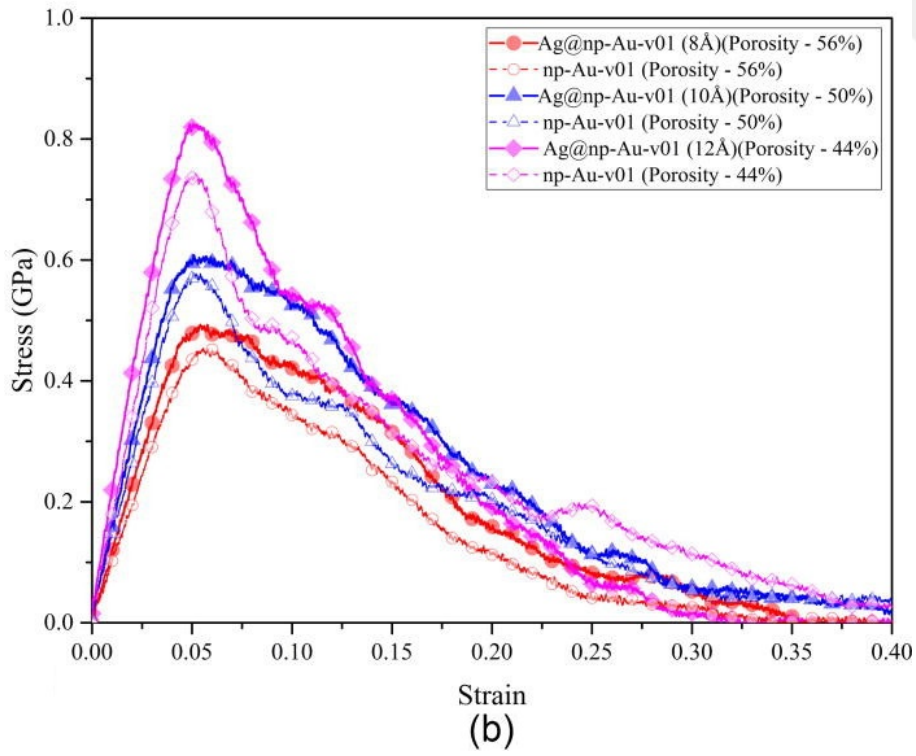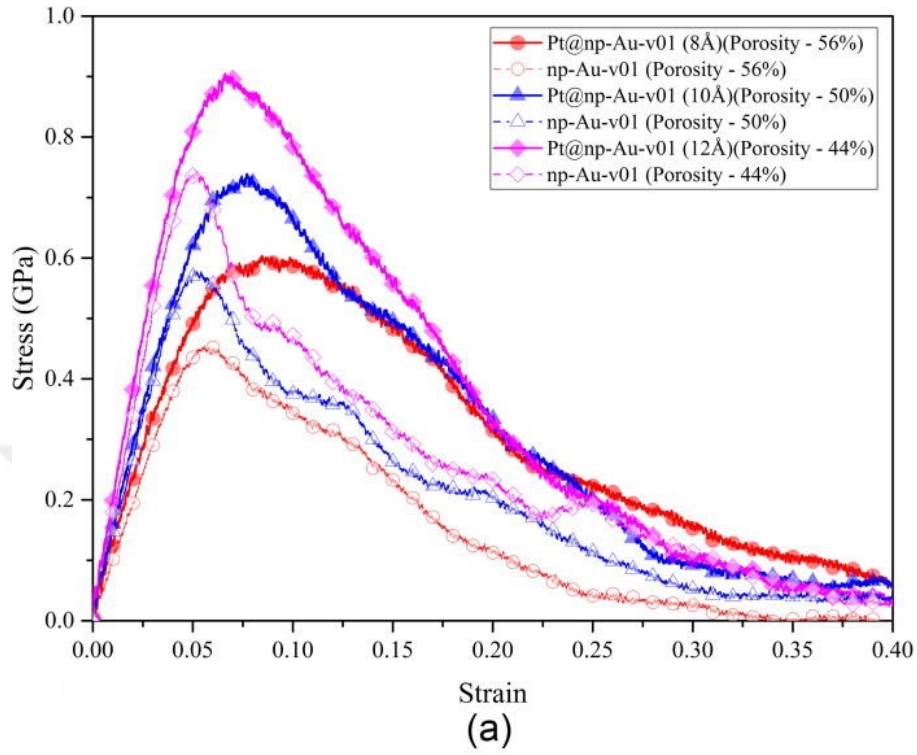
Figure 3.4 : The stress-strain curves of uncoated and coated np materials (v01): (a) Platinum coated np models and (b) Silver coated np models [112].

40

respectively [116]. As the thermal expansion coefficient of Pt is smaller than the one of Au, in the thermalization period, platinum coating acts as a volumetric barrier on the core material, which results in the higher density of dislocations. Besides, it is also known that single-crystalline structures turn into poly-crystalline structures due to high dislocation density [114, 117], which decreases the Young's modulus [118]. This fact explains the reason why Pt-coated specimens have lower Young's modulus than expected. As a further evaluation on this issue, Figure 3.5 provides comparisons between two uncoated specimens and one coated specimen at the same porosity (i.e., 56%). For instance, in Figure 3.5(a), stress-strain curves of uncoated Pt, Au np specimens, and coated Au specimen with Pt are illustrated. Similarly, Figure 3.5(b) presents the comparisons between the uncoated and coated specimens of Au and Ag. According to these, stress-strain curves of Pt- and Ag-coated models are found to be between those of uncoated specimens as expected. Moreover, it is determined that the Young's moduli of np-Ag and np-Pt, which are 11.77 GPa and 12.46 GPa, respectively, are close to each other, which can be used to justify the failure of Pt-coating to meet the expectation for stiffening the np-Au. Furthermore, despite the fact that both of the coating materials (i.e., platinum and silver) increase the ultimate tensile and yield strengths of np-Au, Pt coating provides a more significant increase than Ag coating. However, this improvement maintained by Pt-coating on the yield strength could be more significant, because uncoated np-Pt represents much higher yield strength as shown in Figure 3.5(a). Similar to the issue described for Young's modulus, lower yield strength of Pt-coated np-Au than expected can also be attributed to the high dislocation density. Besides, it must also be noted here that more remarkable improvement observed in the yield strength of the Pt-coated samples is accompanied by a relatively longer yield region, which in turn gives more ductility compared to the Ag-coated samples.

In order to present the effects of coating on the mechanical characteristics quantitatively, the parameters determined from the simulations including Young's modulus, yield, and ultimate tensile strengths of all specimens having different Voronoi skeletons (i.e., v01, v02, and v03) are summarized in Table I. It shows that the models with different Voronoi skeletons present approximately same results. The slight differences between their mechanical properties can be attributed to the differences
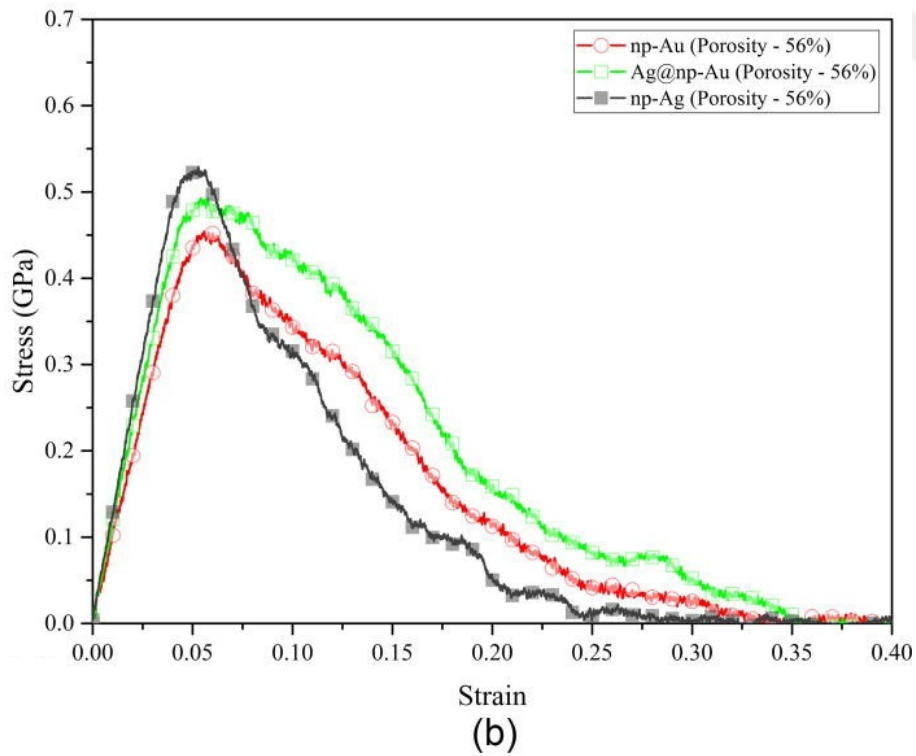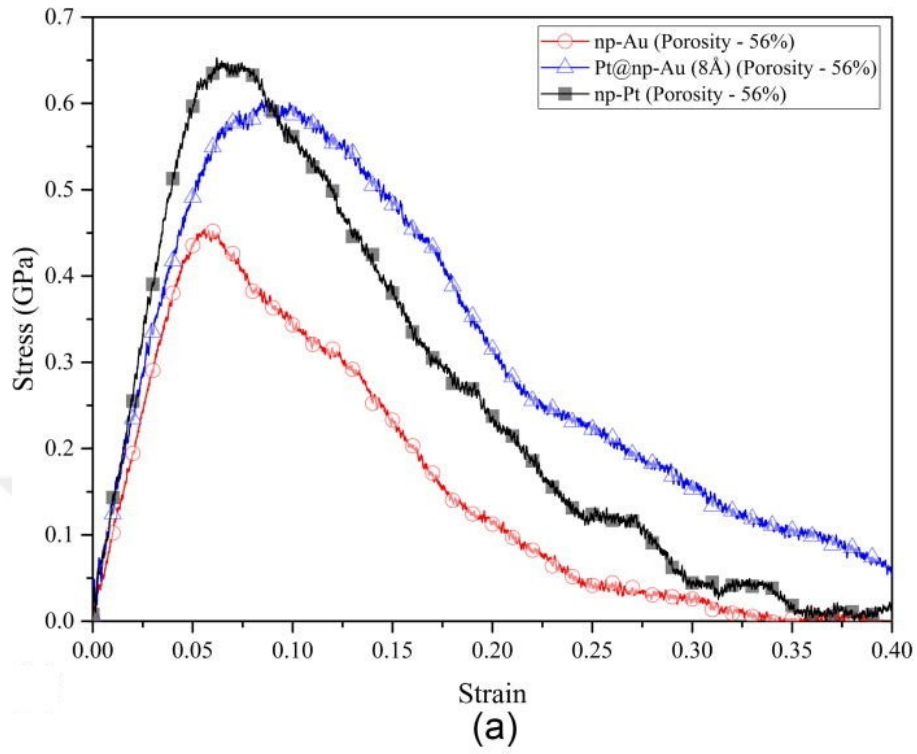
Figure 3.5 : The stress-strain curve comparison of uncoated and 8 Å coated np materials (v01): (a) for platinum coated np models and (b) for silver coated np models [112].

Table 3.1 : Mechanical properties of the uncoated and coated np materials [112].

	Uncoated Models								
Version type	v01	v01	v01	v02	v02	v02	v03	v03	v03
Thickness of coating (Å)	-	-	-	-	-	-	-	-	-
Young's modulus E (Gpa)	9.42	12.48	16.49	9.71	13.01	17.02	9.63	12.66	16.16
Yield Stress σ_y (Gpa)	0.42	0.53	0.69	0.42	0.54	0.70	0.42	0.52	0.70
Ultimate Stress σ_u (Gpa)	0.45	0.58	0.74	0.44	0.58	0.76	0.47	0.60	0.73

	Pt coated Models								
Version type	v01	v01	v01	v02	v02	v02	v03	v03	v03
Thickness of coating (Å)	8.00	10.00	12.00	8.00	10.00	12.00	8.00	10.00	12.00
Young's modulus E (Gpa)	10.20	12.93	17.56	10.60	13.96	18.67	9.57	12.33	16.71
Yield Stress σ_y (Gpa)	0.43	0.54	0.74	0.45	0.57	0.75	0.41	0.53	0.69
Ultimate Stress σ_u (Gpa)	0.60	0.74	0.90	0.64	0.76	0.89	0.60	0.70	0.85

	Ag coated Models								
Version type	v01	v01	v01	v02	v02	v02	v03	v03	v03
Thickness of coating (Å)	8.00	10.00	12.00	8.00	10.00	12.00	8.00	10.00	12.00
Young's modulus E (Gpa)	10.72	13.71	17.99	10.68	13.71	18.67	9.96	12.98	16.97
Yield Stress σ_y (Gpa)	0.46	0.57	0.73	0.45	0.55	0.77	0.43	0.52	0.68
Ultimate Stress σ_u (Gpa)	0.49	0.61	0.83	0.51	0.66	0.84	0.46	0.60	0.77

in angular orientation of quasi-randomly distributed ligaments. The numerical data supported by the visual comparison given in Figure 3.4, for the models coated with different coating materials, the change in Young's moduli, are approximately same for all models, while the yield and ultimate strengths of the silver coated specimens are relatively smaller compared to the specimens coated with platinum. The main deformation mechanisms underlying all these observations presented in this section are explored by examining the formation and evolution of the crystalline defects within the crystal structure of the specimens in the following section.

3.2.2 Effect of coating on the deformation mechanisms

For the purpose of understanding the effects of coating on the deformation mechanisms, the evolution of the microstructure and the atomic defect density are examined quantitatively by monitoring the fractions of hcp atoms, which are calculated as a result of aCNA. The fraction of hcp atoms, which is defined as the ratio of the number of hcp atoms to the number of all atoms, can give information about the density of stacking faults. In this respect, the fraction profile of hcp atoms within the tensile loading period is shown in Figure 3.6 along with the stress-strain graphs of the coated
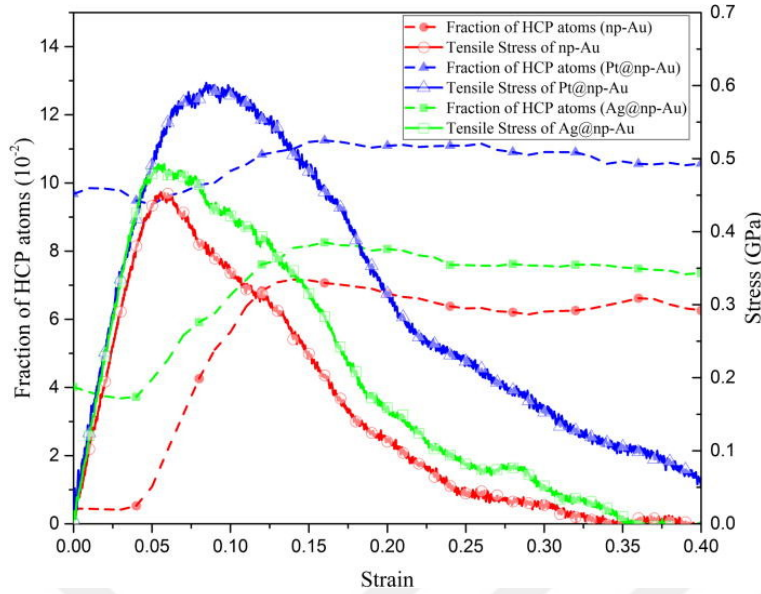
Figure 3.6 : Fraction profile of hcp atoms of coated and uncoated specimens with 56% porosity in the tensile loading process [112].

and uncoated specimens with the same porosity (i.e., 56%) to interpret the evolution of the defects through the deformation process.

Based on Figure 3.6, it is noticed that the fraction profiles of hcp atoms for the coated and uncoated specimens exhibit approximately similar behavior in the manner of that there are 4 distinct regimes along the profile. In the first regime, the fraction of hcp atoms remains approximately constant indicating that the deformation is mainly elastic and the stress increase is observed to be linear with the applied strain. In the second regime, as yielding commences, the hcp fraction increases nonlinearly with a positive slope, which indicates that the rise in the density of the stacking faults results in plastic deformation. In the third regime, the speed of the increase in the fraction of hcp atoms decreases, while some of the ligaments continue to necking and some of them rupture. Following the necking and ruptures of the ligaments, in the fourth regime, it is seen that the fraction of the hcp atoms decreases slightly as the number of unidentified atoms increases due to the effect of relaxation after the necking and rupturing of ligaments. Similar identification of the distinct regimes in the profile for the fraction of hcp atoms is also reported by Sun et al. [103] considering only uncoated np-Au. The main difference between the profiles of coated and uncoated specimens given in Figure 3.6 is the amount of inherent stacking faults formed after the minimization and thermalization periods, or just before the loading period. According to that, for the uncoated np model, the density of the hcp atoms is relatively very low compared to

44

the coated model and the stacking faults that are rarely observed are inherent to the thermalization process before the straining of the specimen. This observation for the uncoated model is compatible with the real NPMs manufactured through chemically dealloying process [119]. In Sec. 3.2.1, several reasons for the higher dislocation density observed in the coated models are discussed in detail.

For a further evaluation of microstructural evolution, aCNA results obtained for the several snapshots of the deformation process at different strain levels are illustrated in Figure 3.7 as cross sectional views. As also referenced by the profiles of hcp atom density in Figure 3.6, for the uncoated specimen, there are very few partial dislocations and stacking faults across the ligaments at the initial deformation stage, while in the coated specimens, the density of the defects including unidentified defects is higher [see Figure 3.7(a)]. Furthermore, the Lomer-Cottrell dislocation locks, which are formed due to reaction of two extended dislocations, are noticed to emerge earlier with a higher density at coated specimens, which results in improved tensile strength and energy absorption ability after yielding [see Figure 3.7(b) and 3.7(c)]. When the total strain exceeds 0.24, almost all ligaments are ruptured in the uncoated specimen, whereas Pt- and Ag-coated specimens have still more load bearing ligaments as shown in Figure 3.7(d). Having higher defect density across the ligaments and the junction areas, which plays an appreciable role to retard the ligament rupture, Pt-coated specimen is tougher than the other specimens.

It is also important to consider the microstructural evolution of individual ligaments considering that the mechanical response of each ligament affects the overall mechanical performance of the np structure. In this regard, as also observed by Sun et al. [103], the orientation of the ligaments with respect to the loading direction is crucial in terms of mechanical behavior of the ligaments. Because the applied strain is initially encountered by the ligaments oriented along the loading direction, the stacking faults cluster typically in the vertical ligaments while the horizontal ligaments generally do not include any defects in the preliminary phase of loading as demonstrated in Figure 3.8.

In order to realize the comparison of coated and uncoated structures at the ligament level, Figure 3.9 presents the sequential snapshots depicting the microstructural evolutions of the coated and uncoated ligament oriented along the tensile loading
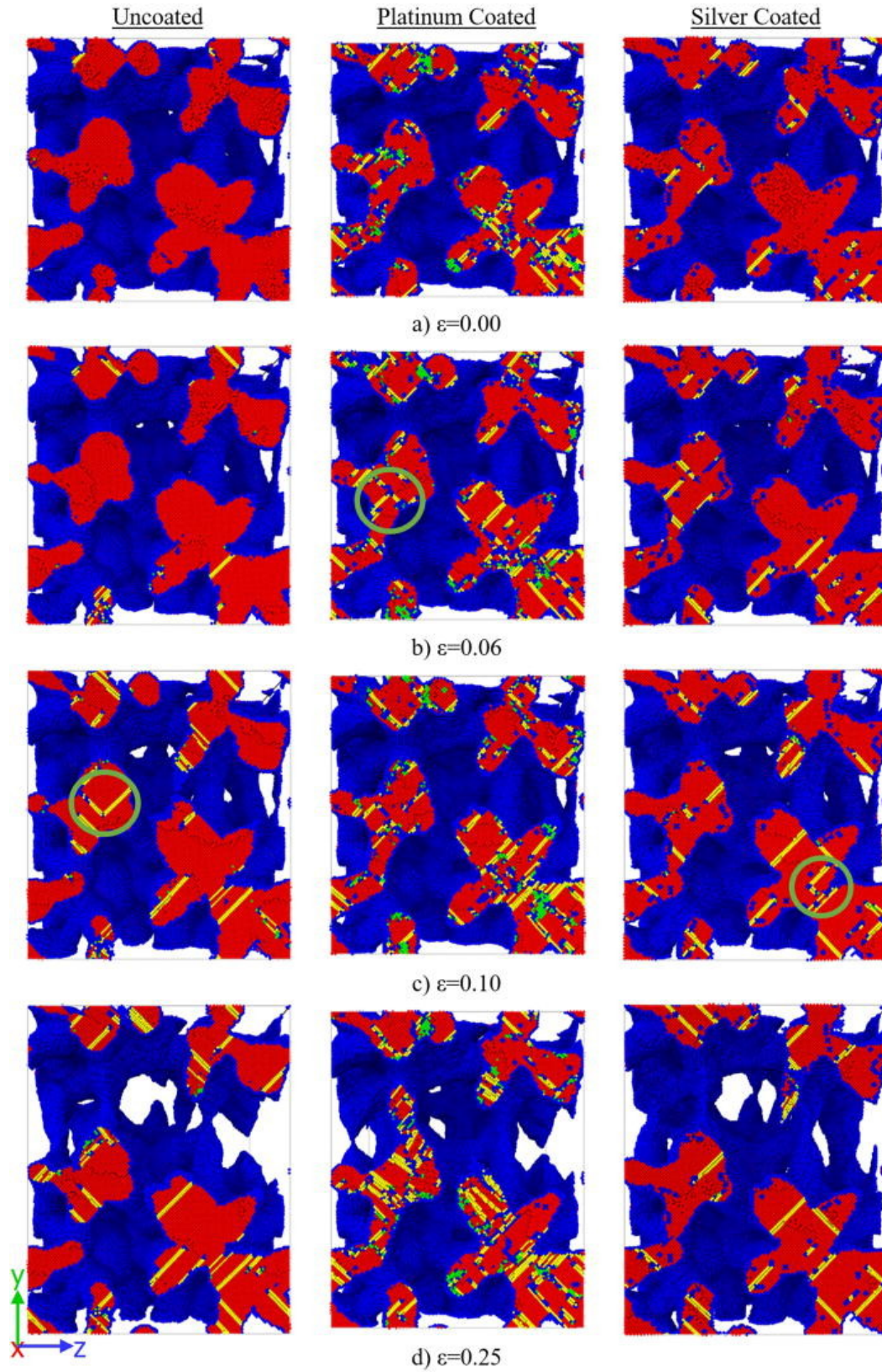
Figure 3.7 : A sequence of snapshots showing the cross sectional evolution of the defects within uncoated and coated np-Au (yz plane at x = 0) [112].
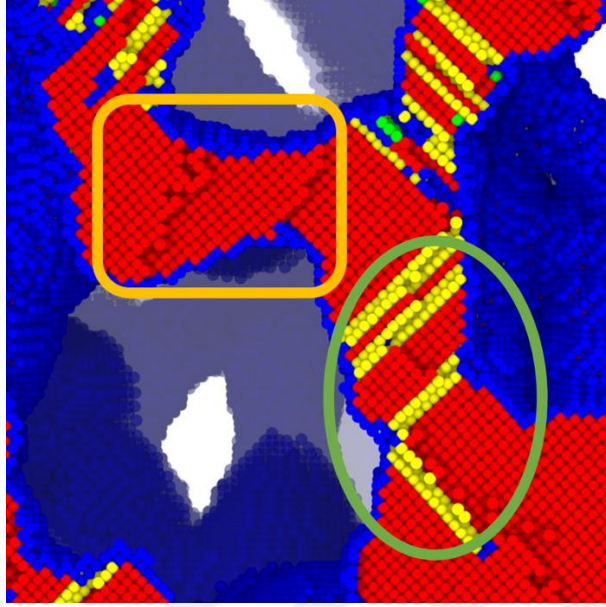
Figure 3.8 : The stacking faults in the horizontal and vertical ligaments ($\varepsilon = 0.10$, uncoated model-v01) [112].

direction and taken from the same location of the porous network. According to this, being compatible with the profiles of the hcp atom density given by Figure 3.6, at zero strain point, there is no defect in the uncoated ligament sample, while the defects across the coated ligaments inherently exist from the previous equilibration process. Despite the fact that the partial dislocations emerged within the uncoated ligaments are emitted from the free surfaces for the coated ligaments. The interface between the core and the coating material is noticed to be another source for the emission of the defects.

In summary, the main difference between the coated and the uncoated np materials is that the coated specimens contain much more crystallographic defects than the uncoated samples, and as mentioned before, those microstructural distinctions enhance the energy absorption ability of coated structures, especially after the yield point. Although the Pt-coated np specimens exhibit more ductile behavior than the Ag-coated specimens, this observation is not valid for all ligaments as indicated by the selected ligament in Figure 3.9. In this regard, the ligament sample of Ag-coated specimen shows a more ductile behavior owing to the higher number of slip planes [see Figures 3.8(c) and 3.8(d)] providing delayed rupture. This difference in the mechanical behavior of the individual ligaments is basically due to the angular orientation of the ligament throughout the porous network.
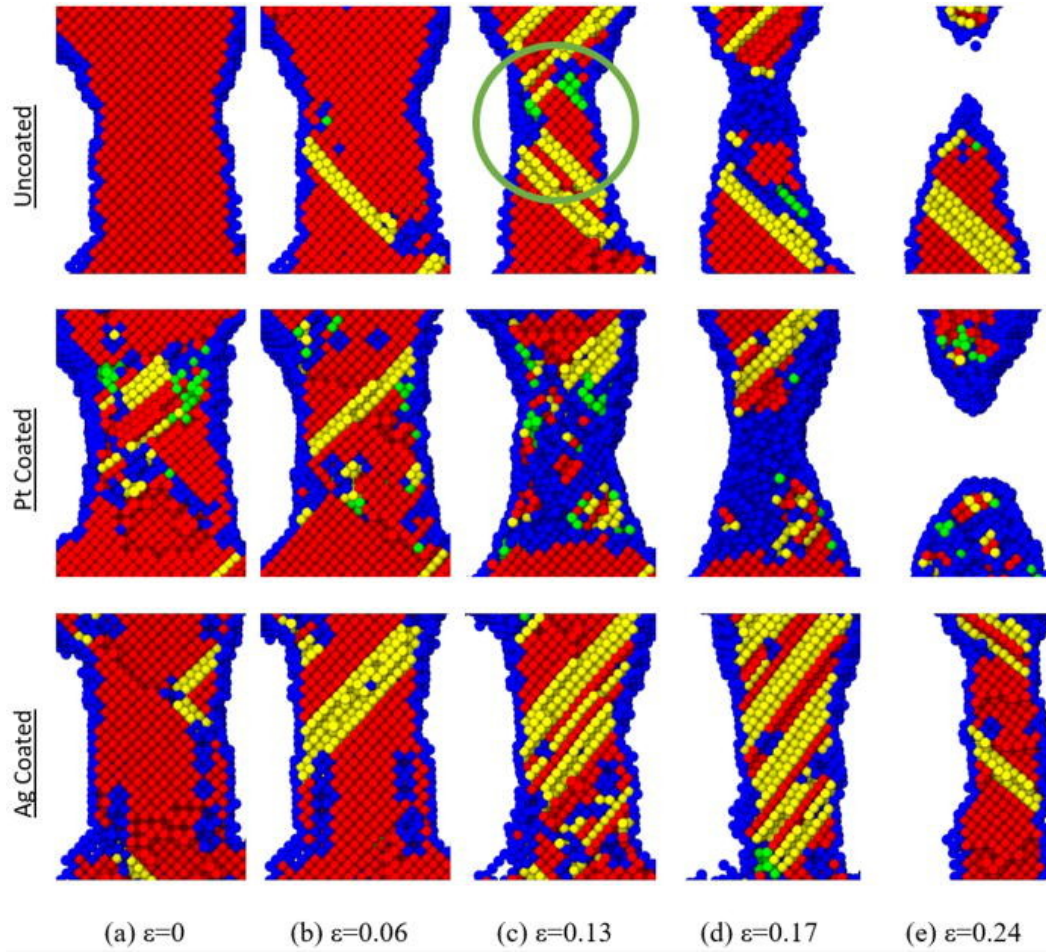
Figure 3.9 : A sequence of snapshots showing deformation of a representative ligament in the tensile direction for the coated and uncoated specimens [112].

3.3 The Compression Behavior of Coated Nanoporous Gold

The stress-strain curves of the models generated by using the Voronoi Tessellation technique under the uniaxial compressive loading are illustrated in Figure 3.10. Here, the stress-strain graphs of the coated and uncoated models with the same porosity are given for different coating materials.

First of all, it can be declared that all the stress-strain curves of the coated and uncoated nanoporous specimens follow three distinct regimes, namely, linear elastic, hardening, and densification, which are typical for cellular solids in compression, as also described in Giri et al. [48] Secondly, considering the previous study of the authors [112] presenting an investigation on the tensile behavior of coated/uncoated nanoporous gold, the compression-tension asymmetry, which is mainly due to the densification of
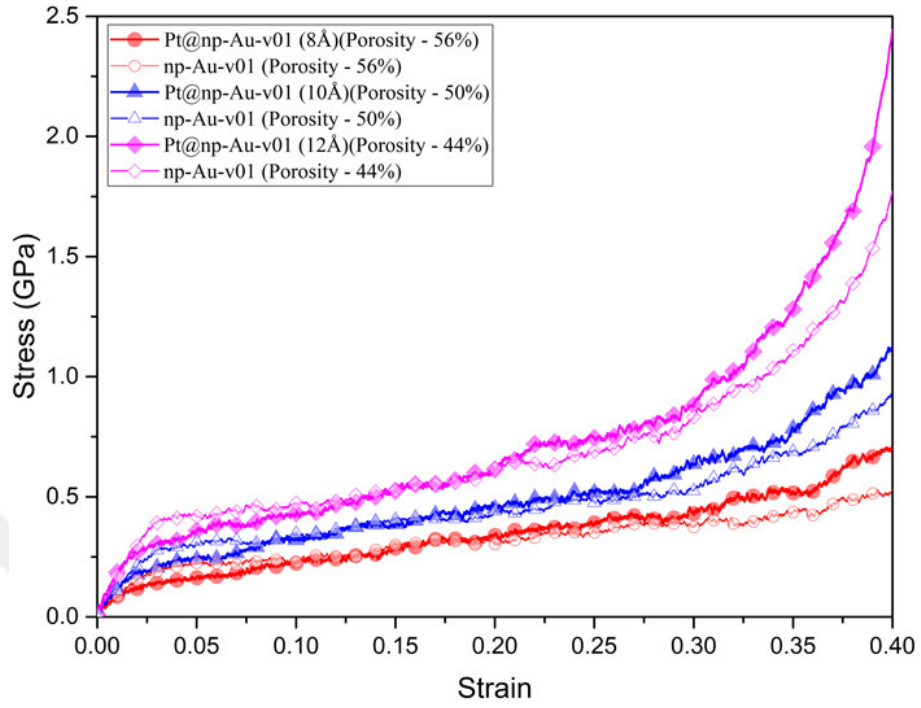
(a)
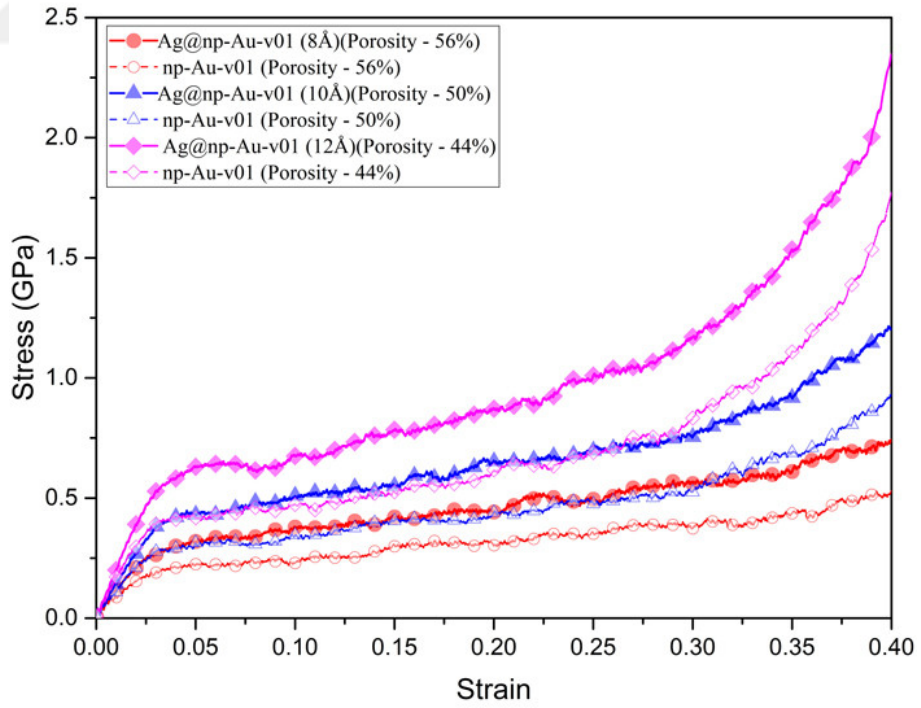
(b)

Figure 3.10 : Compressive stress-strain curves of the uncoated: (a) platinum and (b) silver coated nanoporous specimens (v01) [120].

the network subjected to uniaxial compression with no transverse strain [121, 122], can also be noticed. Therefore, being consistent with the previous investigations [121–123], strain hardening and softening under compressive and tensile loading, respectively, are observed. Finally, the mechanical properties of nanoporous gold with the silver coating are enhanced within all the three regimes. Additional conclusions can be drawn by comparing the stress-strain curves of coated and non-coated samples. For instance, an interesting observation is that the Ag-coated model with a thickness of 8 Å (56% porosity) shows the same strength as uncoated nanoporous gold with higher relative density (i.e., 50% porosity). However, a different situation is observed for the case of the platinum coating. According to this, the enhancement of the mechanical properties of the platinum coated models occurs only at the densification stage. In addition, it is also observed that the platinum coating does not show a reinforcement effect at the linear elastic regime and also reduces the yield strength [see Figure 3.10(a)]. Furthermore, it is intriguing that the tangents of the stress-strain curves in the densification regions are higher for the platinum coated models.

The reasons for the distinctive mechanical characteristics observed for the nanoporous gold material coated with Pt and Ag can be listed as follows:

 i Inward surface relaxation phenomenon

 ii Pre-existing nanovoids between the coating layer and the core.

 iii Differences in thermal expansion behavior.

The first one, the inward surface relaxation phenomenon, manifests itself as a high stress/strain concentration near the surface of the structure [124, 125]. For the purpose of verifying this reasoning, stress distributions within the coated and uncoated specimens after thermalization (i.e., before the loading) are examined as depicted in Figure 3.11.

The surface energy of platinum is known to be higher than the ones of silver and gold [115, 124]. As a result, when the stress states of the specimens at the thermalization stage are compared, it is observed that the surface stresses of the platinum coated specimens [see Figure 3.11(b)] are considerably higher compared to the silver coated and uncoated specimens [see Figures 3.11(a) and 3.11(c)]. Dislocation density is
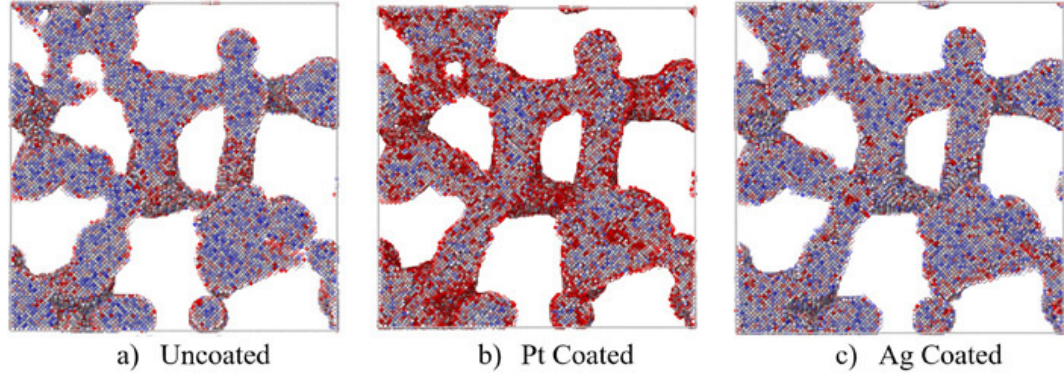
Figure 3.11 : Local stress distribution (von Mises stress) in a slice taken from coated and uncoated nanoporous models just after thermalization (i.e., $\varepsilon = 0$) [120].

expected to be higher in these specimens as the surface stress stimulates the nucleation of the dislocations from the surface or/and coating interface. Secondly, the nanovoids formed between the coating and the core materials due to their different lattice ratios (a_{Au}=4.0801, a_{Pt}=3.9200, and a_{Ag}=4.0896) can be considered as another root cause. In the literature, the mitigating effect of the nanovoids on the yield strain of the ultrathin films of face-centered cubic metals is shown through MD simulations [117]. According to this, the presence and effects of these nanovoids can be explored by utilizing several analysis techniques such as aCNA [93] and Centrosymmetry [126]. In this study, in order to examine the alterations caused by the nanovoids within the crystal structure thoroughly, Figure 3.12 provides the aCNA results of the pre- and post-minimization for a ligament section. For a better illustration of the phenomenon, only one selected ligament is examined, and the coating materials are shown as 50% transparent to demonstrate the emergence of the HCP sequences clearly. According to this, nucleation of the stacking faults from the coating interface due to nanovoids can be observed (circled in Figure 3.12).

In addition, the results of the aCNA convince that the density of the dislocations highly depends on the density of the atoms with the HCP sequence. For this purpose, the temporal evolution of the crystal defects through a cross-section is shown in Figure 3.13. According to the aCNA results, the number of atoms in the HCP sequence shown in yellow for the platinum coated models is much higher. The atoms in the HCP sequence cause a lower yield strain and increase the slope of the stress-strain curve in the hardening stage.
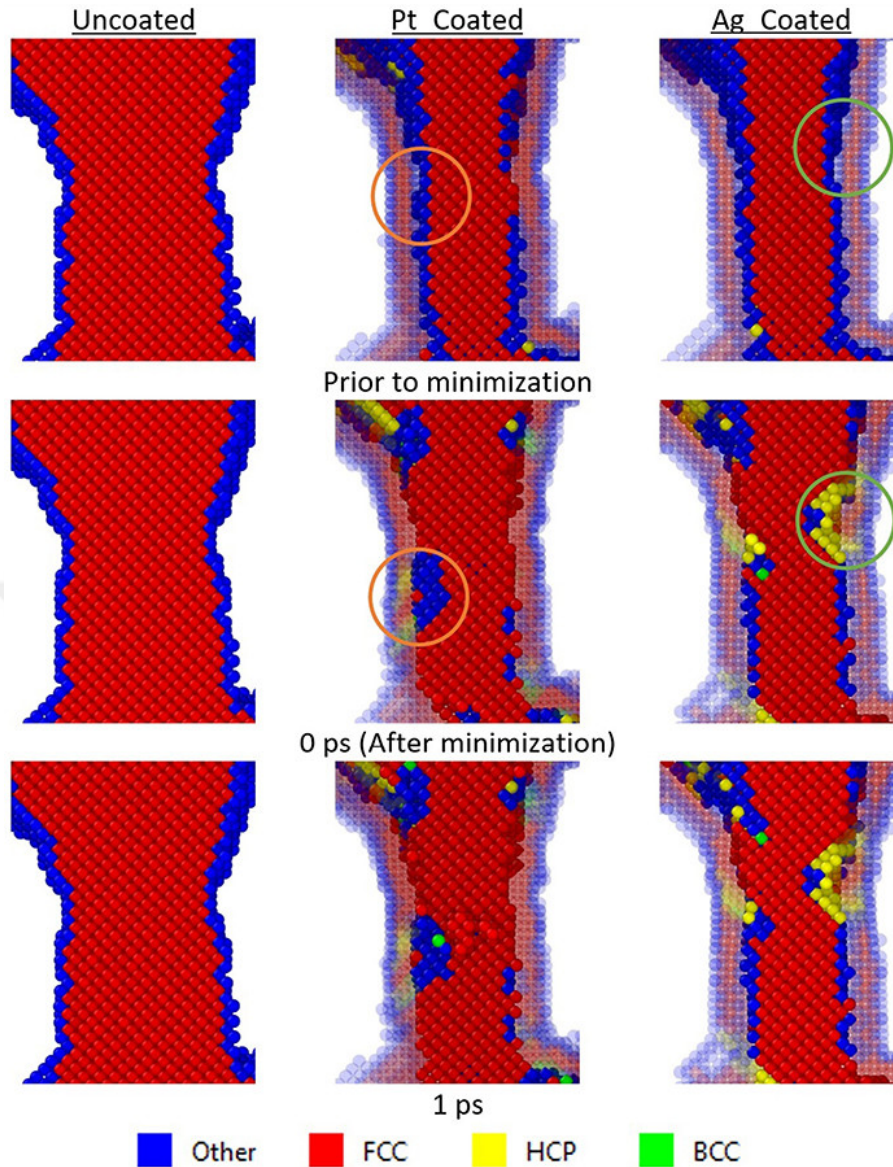
Figure 3.12 : A sequence of snapshots showing the cross-sectional evolution of the ligaments during energy minimization [120].

As mentioned before, the lattice ratios between gold and silver are very close. Thus, the nanovoid effect is quite small compared to the platinum coating. In addition, the lower surface energy of silver yields lower dislocation density in Ag-coated specimens compared to the Pt-coated models. Therefore, enhancements in the elastic modulus and yield strength values are observed for Ag-coated specimens, while approximately the same hardening rates with the uncoated specimens are maintained.

In order to explain the deformation behavior of the specimens based on the stacking faults, the evolution of the density of the HCP atoms and dislocation densities (ρ = total dislocation length/initial volume) obtained by the DXA (Dislocation Extraction Algorithm) [127, 128] are given in Figure 3.14 along with the stress-strain curves.

Uncoated   Pt Coated   Ag Coated

(a) ε=0.00

(b) ε=0.18

(c) ε=0.25

(d) ε=0.40
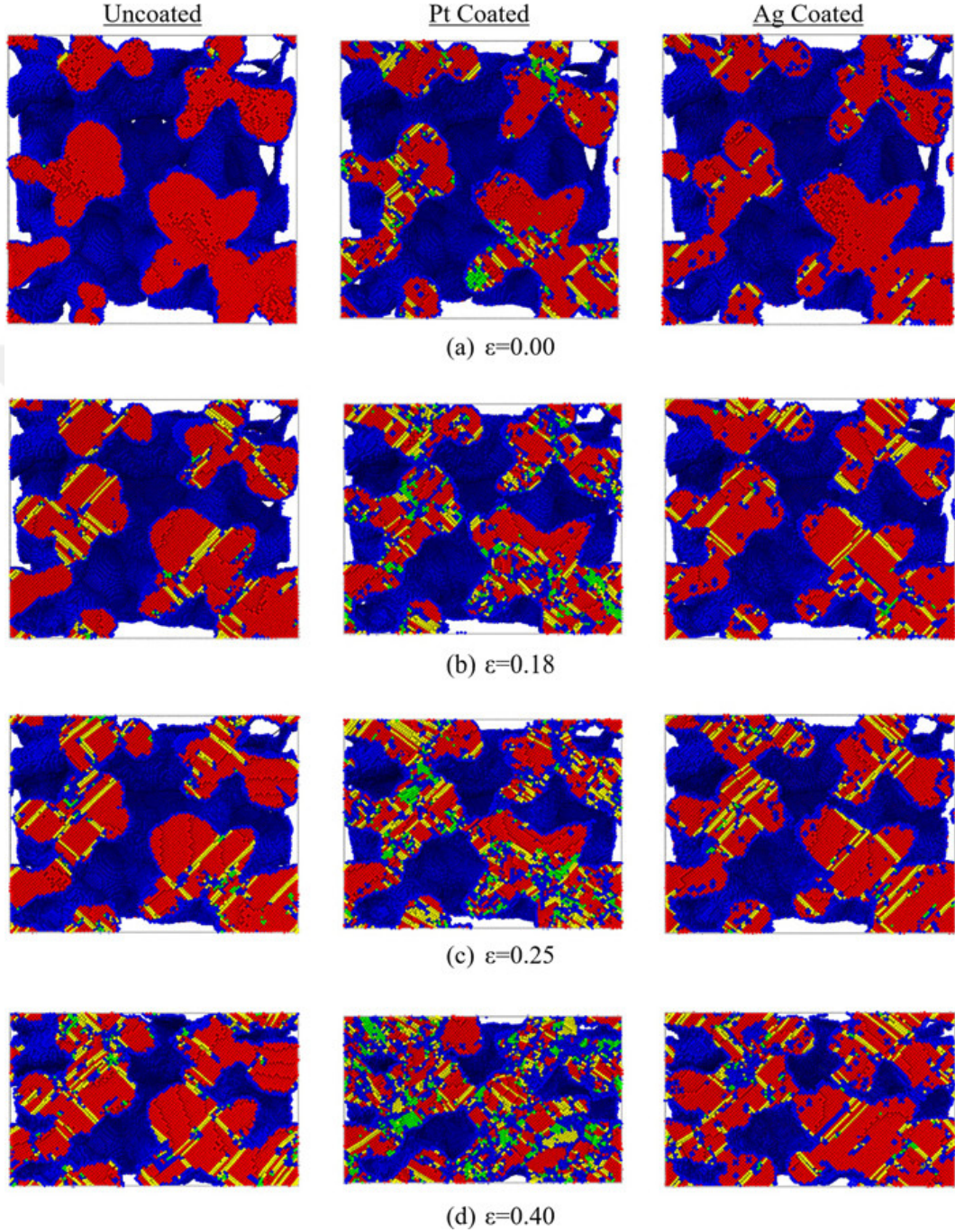
Figure 3.13 : A sequence of snapshots showing the cross-sectional evolution of the defects within uncoated and coated nanoporous gold during compressive loading (yz plane at x = 0) [120].

According to this multi-dimensional comparison, the highest densities of dislocations and HCP atoms are observed within the Pt-coated specimen. As the loading process proceeds, the densities of the dislocations and the HCP atoms increase for all of the coated and uncoated models. However, the rates of the increase in the dislocation and HCP atom densities are higher in the uncoated and Ag-coated specimens owing to the scarcity of the dislocations and HCP atoms formed just after coating.
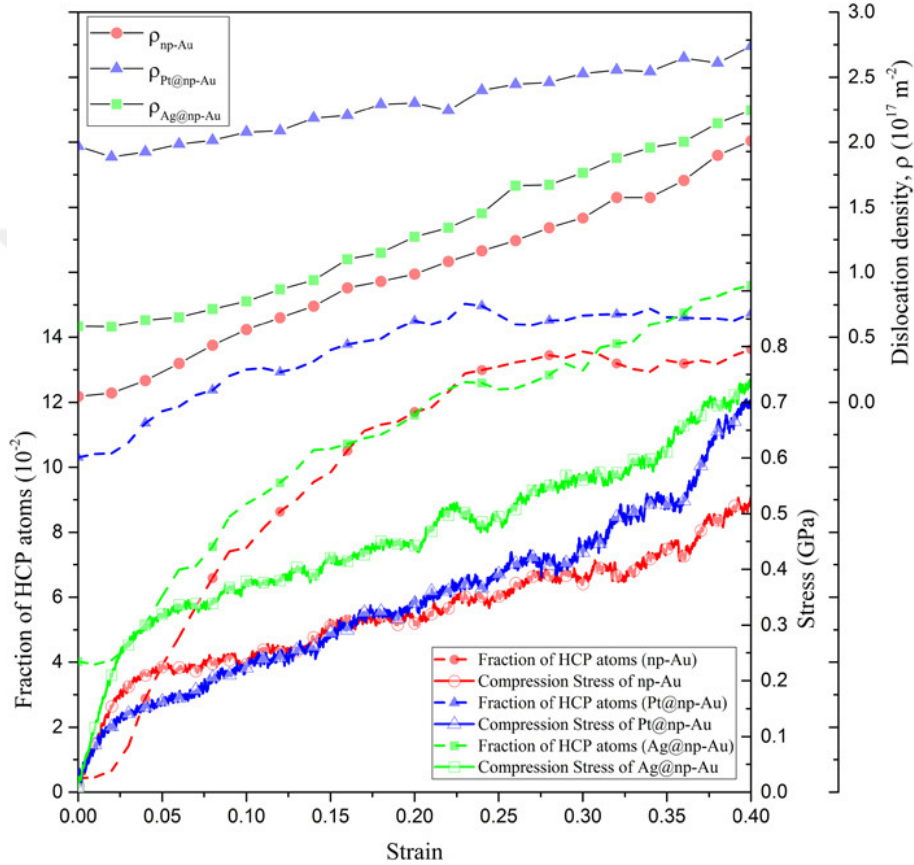
Figure 3.14 : Profiles for the fraction of HCP atoms and dislocation density of the coated and uncoated specimens with 56% porosity in the compressive loading process [120].

The third root cause mentioned before is the natural difference between the thermal expansion coefficients of the core and coating materials. During the thermalization period, as a result of heating up to 300 K, the ligaments of the nanoporous specimens expand depending on the thermal expansion coefficient. In this regard, because the thermal expansion coefficient of platinum (i.e., 8.9×10^{-6}/K) is much lower than that of gold (i.e., 14.2×10^{-6}/K), the platinum coating produces a pressure on the core material (i.e., gold) yielding a complex dislocation network within the material. However, the same phenomenon is not observed for the Ag-coated specimens since the thermal expansion coefficient of Ag (i.e., 18.9×10^{-6}/K) is higher than that of gold.

The high density of dislocations allows single crystalline ligaments to act as nanocrystalline structures, which is also observed in ultra-thin layered metals [114, 117]. By the increase in the dislocation density during the deformation process, the strength of the single crystalline nanoporous materials is reduced, as also seen in nanocrystalline materials [118]. The reason for the lower yield strength of Pt-coated specimens compared to the uncoated and Ag-coated specimens can be explained in this way. In addition, the higher hardening rate observed for the Pt-coated specimen is explained by the dominance of the effect of obstacles (i.e., sessile dislocations) in the dislocation network such as Frank, Hirth, and Stair-rod (Lomer-Cottrel) [96].

3.4 The Shear Behavior of Coated Nanoporous Gold

In order to examine the effects of coating on the shear properties, stress-strain curves of the specimens subjected to simple shear loading are obtained. The graphs for both coated and uncoated specimens are given in Figure 3.15 to realize a comparative examination.

As shown in Figure 3.15(a), significant changes in the yield strength and the post-yield behavior are observed, while no remarkable variation in the shear modulus is noticed for the Pt-coated specimens. As a special case, the yield strengths of Pt-coated specimens with 10 and 12 Å coating thickness are decreased, whereas the yield strength of the model with the thinnest (i.e., 8 Å) coating layer is increased. Furthermore, higher shear stress levels are observed in the softening zone of the coated specimens compared to the uncoated specimens, which improves the toughness. As mentioned previously, this phenomenon occurs due to high dislocation network formed within the specimens due to coating. While the high dislocation density reduces the shear modulus and yield strain of the coated nanoporous specimens, after the yielding point, the obstacles caused by the dislocations increase the strength. As a result, it is noticed that the Pt-coated models have higher toughness. In contrast to Pt-coated specimens, it is comprehended that the yield strengths of the Ag-coated specimens are significantly enhanced by coating and the degree of the enhancement seems to increase by the coating thickness [see Figure 3.15(b)]. Moreover, unlike the Pt-coated models, a slight increase in Young's moduli of the coated specimens are observed for the Ag-coated model with the thickness of 12 Å. Similar to Pt-coating, coating with Ag
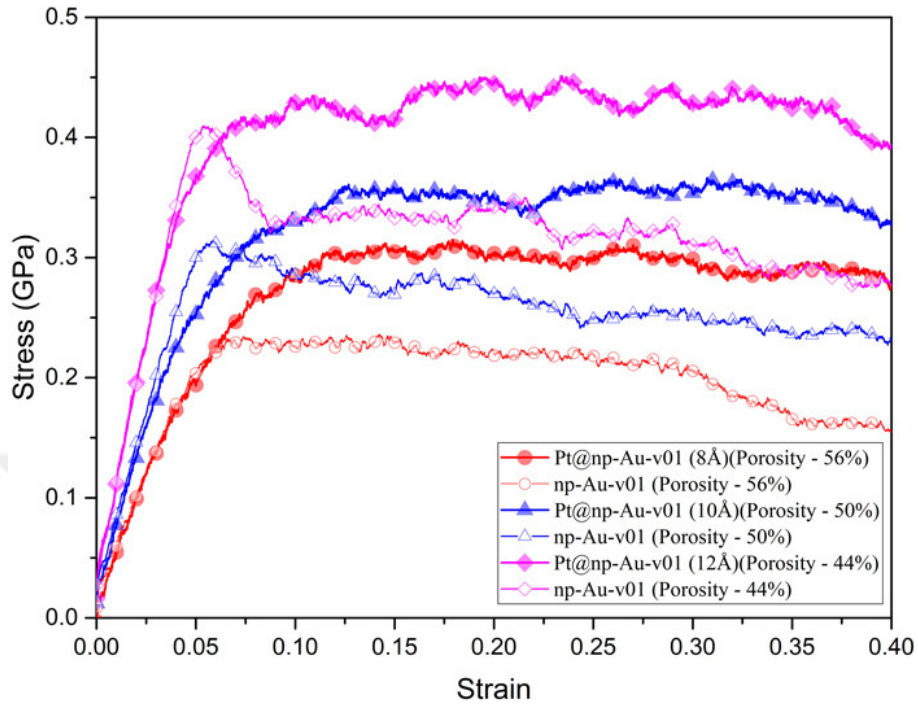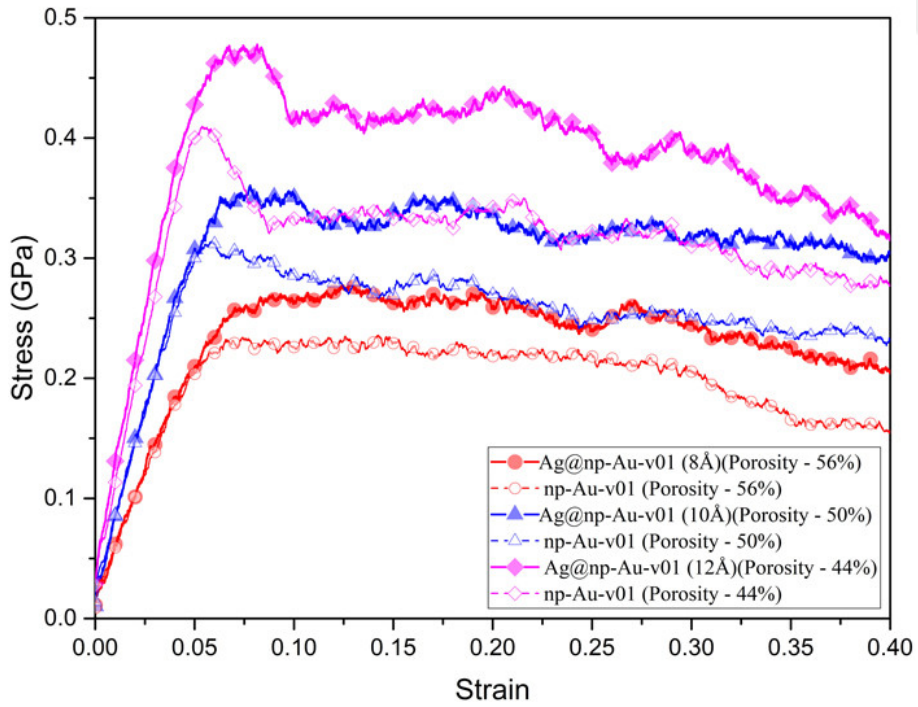
Figure 3.15 : Shear stress-strain curves of the uncoated: (a) platinum and (b) silver coated nanoporous specimens (v01) [120].

also improves the toughness of the nanoporous specimens owing to the higher capacity of load bearing within the post-yield regime.
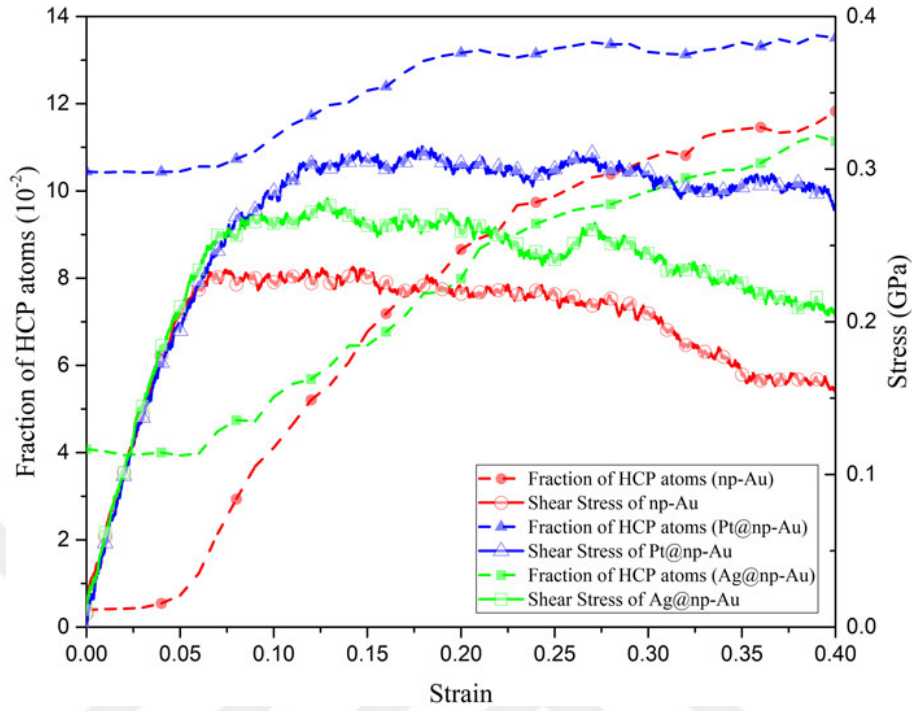
Figure 3.16 : Fraction profiles of HCP atoms for the coated and uncoated specimens with 56% porosity in the shear loading [120].

The aCNAs are also performed as depicted in Figure 3.16 to explain the stress-strain behavior of the nanoporous specimens subjected to simple shear loading. As a result of these analyses, the density of the HCP atoms remains approximately constant in the elastic region (see Figure 3.16) as also observed for the compressive loading, but it begins to increase with the initiation of the yielding. On the other hand, the density of the HCP atoms observed in the shear-loading specimens remains at a lower level compared with the compression specimens. It is entirely due to the different responses resulted from the internal dynamics of the structure depending on the type of loading. According to DXA analyses of the specimens subjected to shear loading, the surplus of dislocation density in Pt-coated specimens is noticed as in the case of compressively loaded specimens. Since this condition is structural alterations due to coating, it is also quite natural to observe it under the shear loading.

The aCNA results for the selected section (i.e., yz plane at x = 0) of the specimens under shear loading are given in Figure 3.17. As expected, the ligaments deform to be adjusted along the shearing direction. In this regard, the ligaments perpendicular to the yz section (i.e., along the x axis) are not affected considerably under shear loading
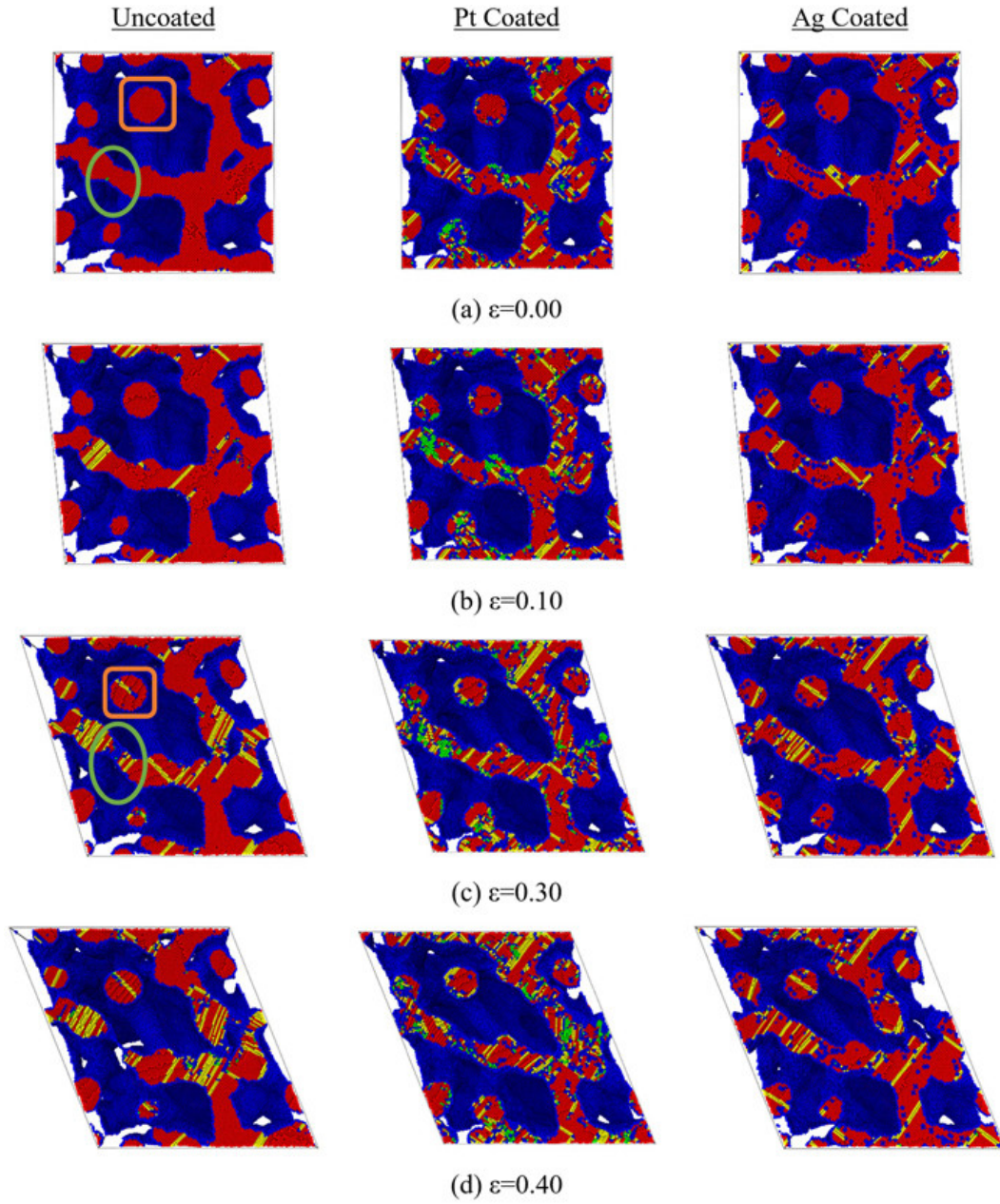
Figure 3.17 : A sequence of cross-sectional snapshots for the evolution of the defects within the uncoated and coated nanoporous specimen during shear loading (yz plane at x = 0) [120].

applied in the yz plane. This situation is demonstrated in Figure 3.17(a) by squaring such a ligament cross section. Hence, the orientation of the ligaments is very decisive for the mechanical response of the ligaments as in the case of compressive loading, which in turn affects the overall mechanical behavior of nanoporous structures.

4. THE BEHAVIOR OF NANO-CRYSTALLINE NANOPOROUS GOLD

Many studies regarding nanoporous metals (NPMs) have appeared in literature recently [6, 11, 129]. These studies are carried out in order to understand their fascinating mechanical, physical and chemical properties better. Although most of studies on NPMs are performed through experimental works [98–100, 130], NPMs' properties can also be investigated by numerical methods such as molecular dynamics (MD) simulations [103, 112, 120, 131, 132]. The experiments that are difficult to perform within laboratory conditions can be easily conducted through numerical simulations. As well known, the accurate results can be obtained by employing proper modeling and simulation techniques. Another fact is that it is quite difficult to generate atomistic models of NPMs due to their complex morphological structure.

Several modeling techniques developed for the numerical modeling of nanoporous structures can be found in literature. For instance, the phase field method [109] is one of the most common techniques used to obtain nanoporous structure models. This method simulates decomposition of a binary fluid mixture of two components by using Cahn-Hilliard equation which expresses a spinodal evolution of decomposition [110]. Another modelling technique, which is mainly employed to generate porous structures with spherical cells, is based on the extraction of an ensemble of randomly distributed spherical volumes intersected with each other from a bulk volume [46]. In a recent study, Yildiz and Kirca [60] proposed a new modeling technique based on the Voronoi Tessellation method, which unlike other studies helps significantly to control the structural morphology of NPMs. While all of these modeling techniques provide single-crystalline nanoporous structures, it is shown in literature that nanoporous structures produced by dealloying process are nano-crystalline [133]. With this motivation, Yildiz and Kirca [134] presented a new hybrid technique to generate atomistic models for nano-crystalline nanoporous materials for the first time. In general, this modeling technique has emerged as a composition of a nanoporous model, which is developed by Yildiz and Kirca [60], and a nano-crystalline bulk material

model based on Voronoi tessellation method [135]. Then, Xian et al. [131] presented a modeling technique similar to Yildiz and Kirca [134], which is a combination of the phase field method [109] and the bulk nano-crystalline model. Another study of Xian et al. [132] presented the tensile behavior of nano-crystalline nanoporous gold (nc-NPAu) with different grain sizes.

Even though some aforementioned numerical studies on nano-crystalline NPMs can be found in literature, to the best of the authors' knowledge, there is not any numerical investigation which may help to deepen the scope of the research on strain rate effects. On the other hand, strain rate and geometric scaling effects on the mechanical behaviour of nanowires can be found in literature [136, 137]. With this motivation, the ultimate goal of this study is to investigate strain rate effects on nc-NPAu structures subjected to tensile and compressive loading. For this purpose, firstly, atomistic models of nc-NPAu structures with different grain size are generated by using the modeling technique of Yildiz and Kirca [134]. Then, the generated models are subjected to tensile and compressive loading with different strain rates by employing classical molecular dynamics simulations. Simulation results are post-processed through adaptive common neighbor analysis (aCNA) to explain the observations by microstructural evolution.

4.1 Modeling and Simulation Details

4.1.1 Generation of atomistic models

The algorithm of the modeling method employed to generate atomistic models of nc-NPAu, which allows users to control cross sectional dimensions (i.e. ligament size) and mass distribution along the longitudinal axes of the ligaments, consists of five steps as shown in Figure 4.1. In the first step, an algorithm, which has been already used in literature, is chosen for the modeling of nano-crystalline bulk gold [135]. The bulk structure of nano-crystalline gold with periodic boundary condition can be generated by using this algorithm. In addition, it allows users to control some parameters such as grain and model size. The desired grain and model size can be provided as an input into this algorithm. The Voronoi cells formed according to the desired grain size constitute the granules of the nano-crystalline models. In the second stage,
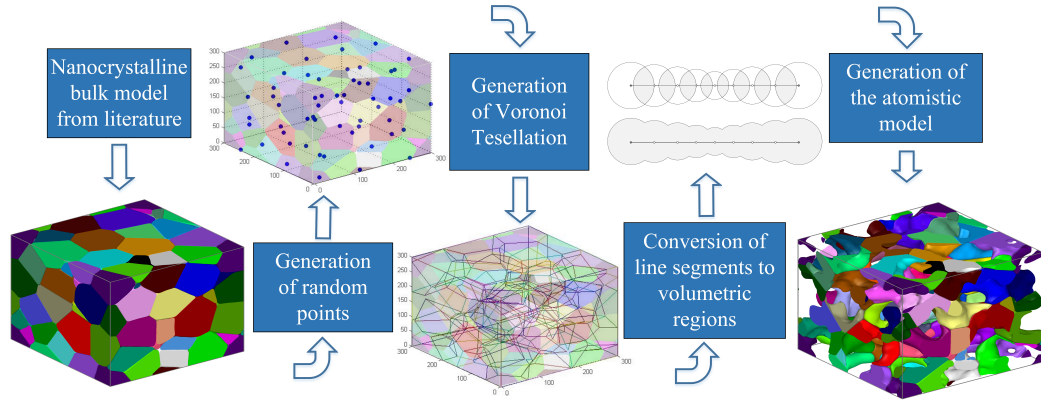
Figure 4.1 : Flowchart of the general algorithm.

another Voronoi tessellation process is initiated to define the volumetric region for the ligament network of the nanoporous structure. For this purpose, a point cloud is generated under certain constraints that will be employed for the establishment of the Voronoi tessellation, which results in randomly oriented and intersected line segments. Then line segment representation of the Voronoi tessellation is converted into a unique volumetric region by using the spherical regions. In order to maintain a smooth ligament surface, the number of spherical regions is adjusted carefully. Finally, the atoms exterior to this volumetric region are removed from the nano-crystalline bulk gold, which yields a periodic nc-NPAu structure. The method of generating atomistic models for nano-crystalline nanoporous structures can be found in detail in Yildiz and Kirca [134].

4.1.2 Simulation techniques

One of the main challenges faced by researchers investigating nanoscale systems is to define material properties. As known, mechanical properties of nano-crystalline materials are dominated by interfaces between atomic scale imperfections and crystalline regions. Therefore, parameters (i.e. grain size, grain number) are highly important as they affect the physical behavior of nano-crystalline NPMs. With this motivation, three cubic atomistic models with periodic boundary conditions are generated with different grain sizes while keeping the porosity constant (i.e. 56%). In this respect, depending on the grain size (i.e. 100 Å, 125 Å, 150 Å), the models are named as gs100, gs125 and gs150 respectively. In addition, a single-crystalline nanoporous gold (sc-NPAu) model is generated with the same porosity to be compared

(a) Single-crystalline   (b) Nano-crystalline
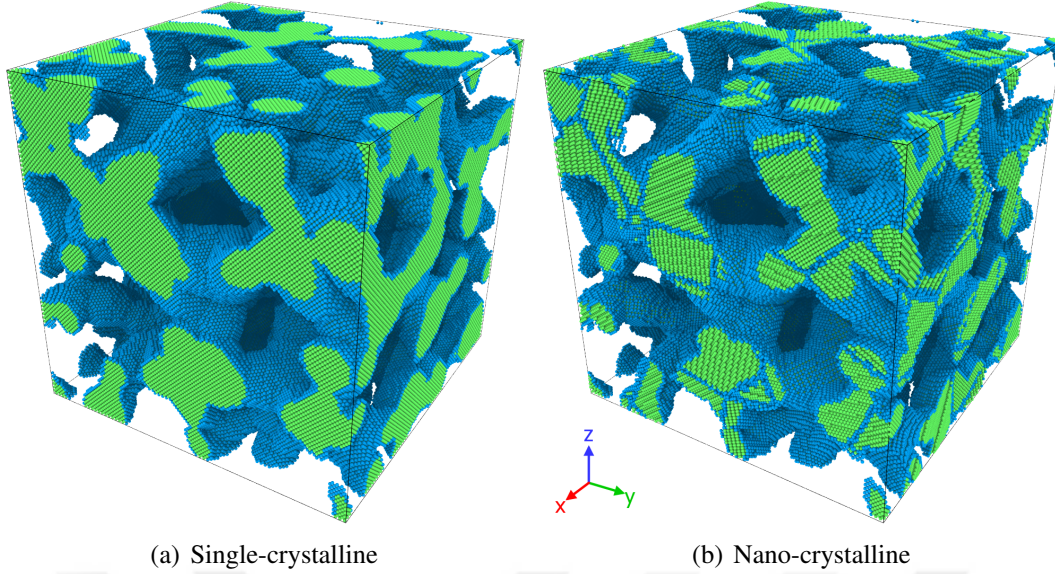
Figure 4.2 : Examples of single- and nano-crystalline nanoporous gold models.

with other nc-NPAu models. Figure 4.1 shows two raw atomistic models consisting of approximately 800 000 atoms prior to the thermal equilibration of sc- and nc-NPAu.

Molecular dynamics simulations used to analyze the generated atomistic models of nc-NPAu are performed by utilizing an open source code LAMMPS [26, 27]. In these simulations interaction between the gold atoms is determined by the corresponding potential based on the embedded atomic method (EAM), where the total potential energy consists of the embedding energy as a function of the atomic electron density and the pairwise interaction energy [138, 139], as follows:

$$E_i = f\left(\sum_{j \neq i} \rho(r_{ij})\right) + \frac{1}{2}\sum_{j \neq i} \varphi(r_{ij}) \tag{4.1}$$

where E is the total energy, f is the embedding energy function, ρ is the atomic electron density, φ is the pair-wise potential interaction and r_{ij} is the distance between atoms i and j.

The time step of the simulation is set as 0.001 ps while periodic boundary conditions are applied to the system in all orthogonal directions. After minimizing the energy of the system, all the models are thermally equilibrated at 300 K for 1 ns by utilizing the integrator of NPT (isothermal-isobaric) ensemble. Following the thermalization step, each nc-NPAu model is subjected to a uniaxial tensile and compressive loading along the y direction with different strain rates (i.e. 0.0005, 0.001, 0.002, 0.004 ps^{-1}) under

NVT canonical ensemble with a Nose-Hoover thermostat. All atomistic models are stretched and compressed by 50% of their length and the atomic stresses are calculated by using Virial stress theorem [86, 140] for each loading step, as follows:

$$\boldsymbol{\sigma}_{ij} = \frac{1}{V} \left(-m_i \dot{\boldsymbol{u}}_i \otimes \dot{\boldsymbol{u}}_i + \frac{1}{2} \sum_{j(\neq i)} \boldsymbol{r}_{ij} \otimes \boldsymbol{f}_{ij} \right) \tag{4.2}$$

where $\boldsymbol{\sigma}$ is the virial stress, V is the volume, m is the mass of a particle i, $\boldsymbol{u}_i$ is the displacement of ith relative to a reference position, $\boldsymbol{f}_{ij}$ is the force vector and $\boldsymbol{r}_{ij}$ is the distance between atoms i and j.

Furthermore, the adaptive common neighbor analysis (aCNA) [93, 94] which is a computational analysis method used to determine local atomic arrangements in atomistic simulations of crystalline structures, is employed by OVITO software to monitor the evolution of microstructural defects. As a result of the aCNA, atom types are colored differently [i.e., green for Face Centered Cubic (FCC) atoms, blue for Body-Centered Cubic (BCC) atoms, red for Hexagonal Close Packed (HCP) atoms, and gray for unidentified atoms (i.e. surface atoms)] to identify the crystallographic structure.

4.2 Results and Discussion

4.2.1 Tensile strength of nano-crystalline nanoporous gold

The stress-strain curves obtained by performing MD simulations on the nanoporous specimens with single- and nano-crystalline structures subjected to uniaxial tensile loading at varied strain rates are depicted in Figure 4.3. Furthermore, the mechanical characteristics such as the modulus of elasticity, the maximum stress, the yield strength, etc. are summarized quantitatively in Table 4.1.

While all the curves coincide at small strain within the stiffer linear regime, discrepancies are noticed toward yield strength points. After the ultimate tensile strength point, all the curves exhibit a softening behavior, which is a typical response of ductile materials. The findings point out that higher ultimate and yield strength values are obtained as the strain rates are increased. In addition, almost no variation is noticed on the elastic moduli of sc-npAu models with different strain rate, while the elastic

(a) Single-crystalline   (b) Nano-crystalline (gs100)

(c) Nano-crystalline (gs125)   (d) Nano-crystalline (gs150)
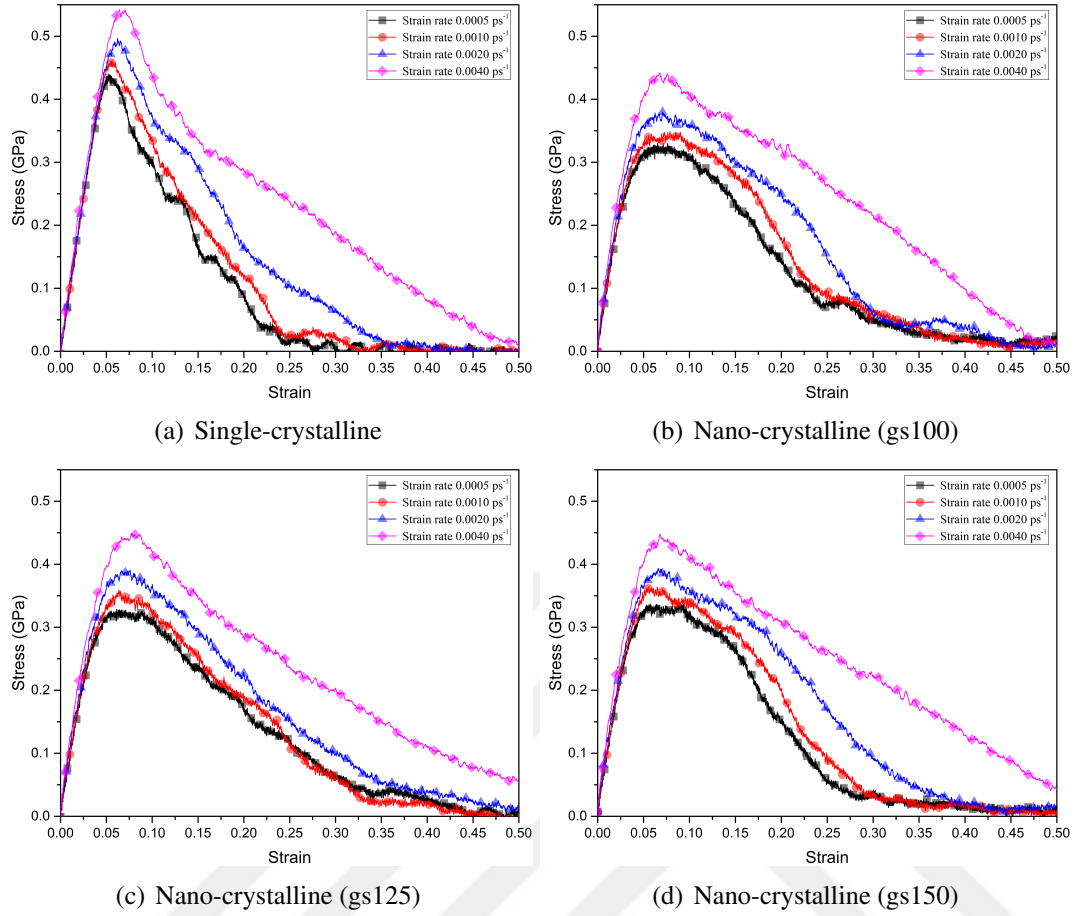
Figure 4.3 : Stress-strain curves at different loading rates for single- and nano-crystalline nanoporous gold.

moduli of nc-npAu specimens show sensitivity to the change in strain rate. Owing to this sensitivity, we can observe that the stress-strain curves of the nc specimens are clearly distinguishable from each other in the elastic zone, which is also proved by the quantitative results (see Table 4.1). These results clearly show that the nano-crystalline structure of the atomistic model has a remarkable effect on the mechanical properties.

As known, toughness is directly related to the energy absorption capacity of a material and integration of the area under the stress-strain curve can be used to calculate energy absorption. In this regard, based on the stress-strain curves it can also be concluded that the energy absorption capacity of all specimens increases with the strain rate, while it is known oppositely that the energy absorption capacity of nanowires drops dramatically at increased loading rates [137]. Furthermore it is also observed that nc-NPAu specimens absorb more energy compared to sc-NPAu models, especially after the yield point. This can be attributed to the fact that the grain boundaries in

Table 4.1 : Mechanical properties of single- and nano-crystalline nanoporous gold for uniaxial tensile loading.

	Model name	Strain rate	Max Strength (GPa)	Max Strain	Modulus of Elasticitiy (GPa)	Yield Strength[*] (GPa)	Yield strain
single crystalline	sc	0.0005	0.44051	0.05197	10.12302	0.35190	0.03766
	sc	0.0010	0.46191	0.05617	9.91136	0.36856	0.03905
	sc	0.0020	0.49643	0.06224	10.12150	0.38639	0.04066
	sc	0.0040	0.54192	0.06439	10.73027	0.41648	0.04203
nano crystalline	gs100	0.0005	0.33052	0.06539	7.63686	0.26995	0.03555
	gs100	0.0010	0.34854	0.07887	8.24728	0.28135	0.03523
	gs100	0.0020	0.37944	0.07064	8.79192	0.30342	0.03505
	gs100	0.0040	0.44212	0.06773	9.37828	0.35850	0.03925
	gs125	0.0005	0.32845	0.06143	7.69745	0.26640	0.03559
	gs125	0.0010	0.35942	0.06357	7.95033	0.27686	0.03527
	gs125	0.0020	0.39045	0.07605	8.14585	0.31508	0.03884
	gs125	0.0040	0.44895	0.07752	9.49934	0.31556	0.03509
	gs150	0.0005	0.33873	0.08894	7.95110	0.25797	0.03165
	gs150	0.0010	0.36516	0.05515	8.64378	0.26692	0.03187
	gs150	0.0020	0.39368	0.06603	8.49293	0.30193	0.03577
	gs150	0.0040	0.44781	0.06765	9.55910	0.31677	0.03362

[*] Determination of the yield strength is used the %0.2 offset method.

nc specimens prevent the material from shearing easily throughout the slip planes. So the material continues to deform with higher toughness after the yielding point.

As a further examination the stress-strain curves of sc- and nc-NPAu specimens at the strain rate of 0.5E-3 ps^{-1} can be compared (Figure 4.4) to give a better understanding of their mechanical behavior. According to Figure 4.4 and Table 4.1, as the grain size increases (i.e. as the number of grains decreases) the modulus of elasticity and the ultimate strength of nc-NPAu specimens get closer to those of sc-NPAu as expected. Moreover, nc-NPAu models exhibit more ductile behavior compared to the sc-NPAu especially at the lower strain rates, which is ensured by the observation that the nc-NPAu specimens rupture later than sc-NPAu ones. This phenomenon is evaluated in the following part of the study.

In order to provide a better understanding of the deformation mechanisms of nc-NPAu models, the evolution of the microstructure is investigated quantitatively by performing an aCNA. As previous studies also reported, stress-strain curves of nanoporous materials exhibit 4 distinct regimes (see Figure 4.5) considering the fraction of HCP
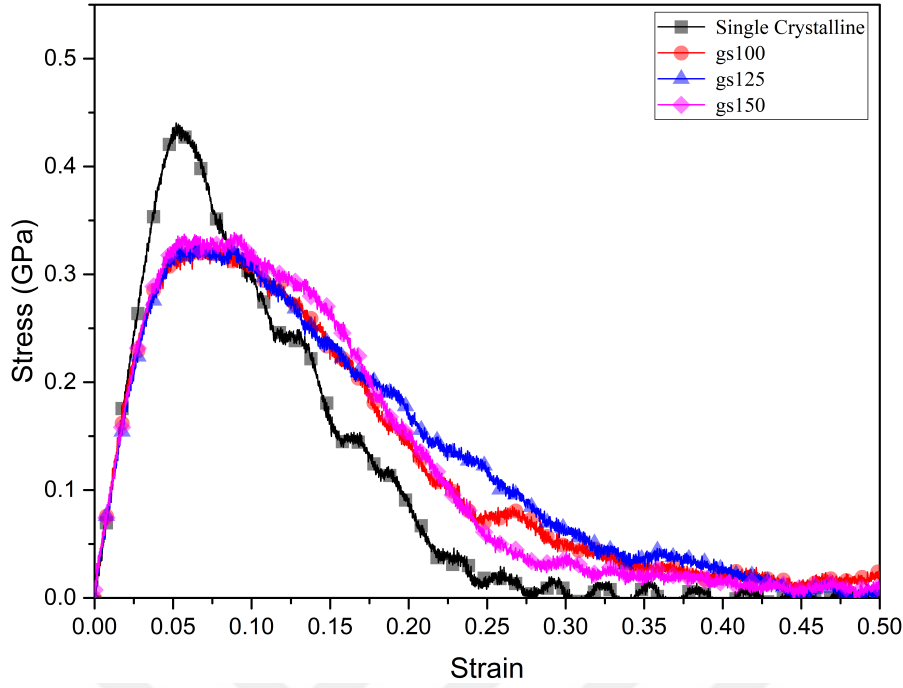
Figure 4.4 : Stress-strain curves at different grain size for sc- and nc-NPAu ($\dot{\varepsilon}$ = 0.5E-3 ps^{-1}).
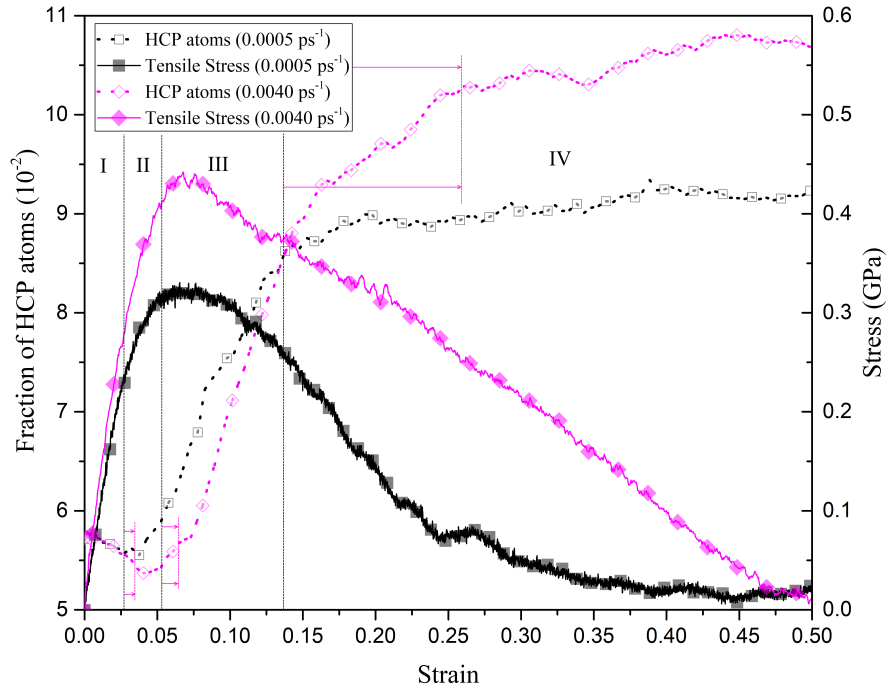
Figure 4.5 : Fraction of HCP atoms of nc-NPAu (gs100) at two strain rates under tensile loading.

atom profiles [47, 112]. In the first regime the proportion of HCP atoms that gives information about the density of stacking faults and partial dislocations remains approximately constant and it shows that the deformation takes place mainly in the elastic zone and the stress increases linearly with the applied strain. After the yield

point, in the second regime, the HCP proportion increases significantly pointing out the initiation of the plastic deformation. In the following regime, the increment rate in the proportion of HCP atoms increases, whereas some of the ligaments continue to necking and some of them rupture. In the last regime the growth of the HCP atom population decelerates and the number of unidentified atoms increases owing to the relaxation occurring after the rupturing of ligaments. Although the loading rate does not change the general trend of the HCP atom profiles, the number of the HCP atoms and so the stress-strain curves of the specimens are affected. Especially, the sharp increase of HCP proportion in the third regime indicates that the specimen gets tougher, which results in enhancement of the energy absorption capacity.
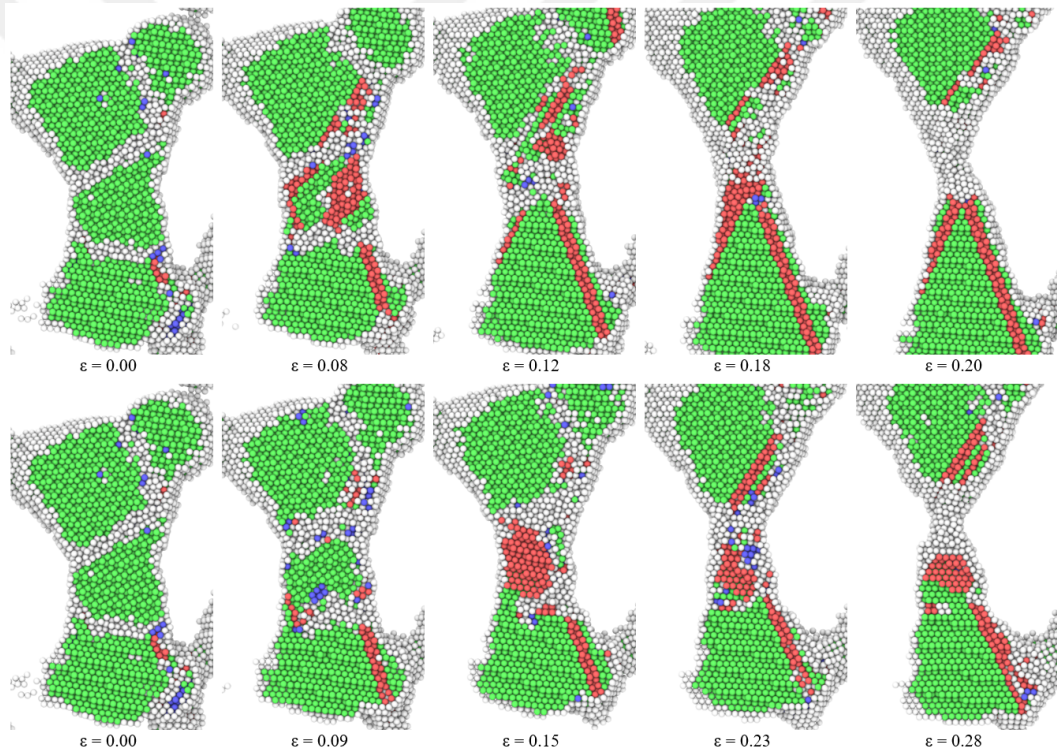
Figure 4.6 : A sequence of snapshots showing the deformation of a representative ligament in the tensile direction for nc-NPAu (gs100) at two strain rates.

For a better understanding of the deformation mechanism, microstructural evolution of a selected ligament is examined from the point of different strain rates by using the aCNA as depicted in Figure 4.6. According to the obtained aCNA results, ductility of the ligament is noticed to be higher at increased strain rate. The strain rate especially changes the direction and magnitude of atomic displacements as demonstrated in Figure 4.7, which presents the displacement vectors and aCNA results of the selected ligament at the same strain level (i.e. $\dot{\varepsilon} = 0.125$ ps^{-1}). The direction of the

69

atomic motion generates new obstacles for the slip planes, which elevates the energy absorption and as a result of this the rupture process is delayed.
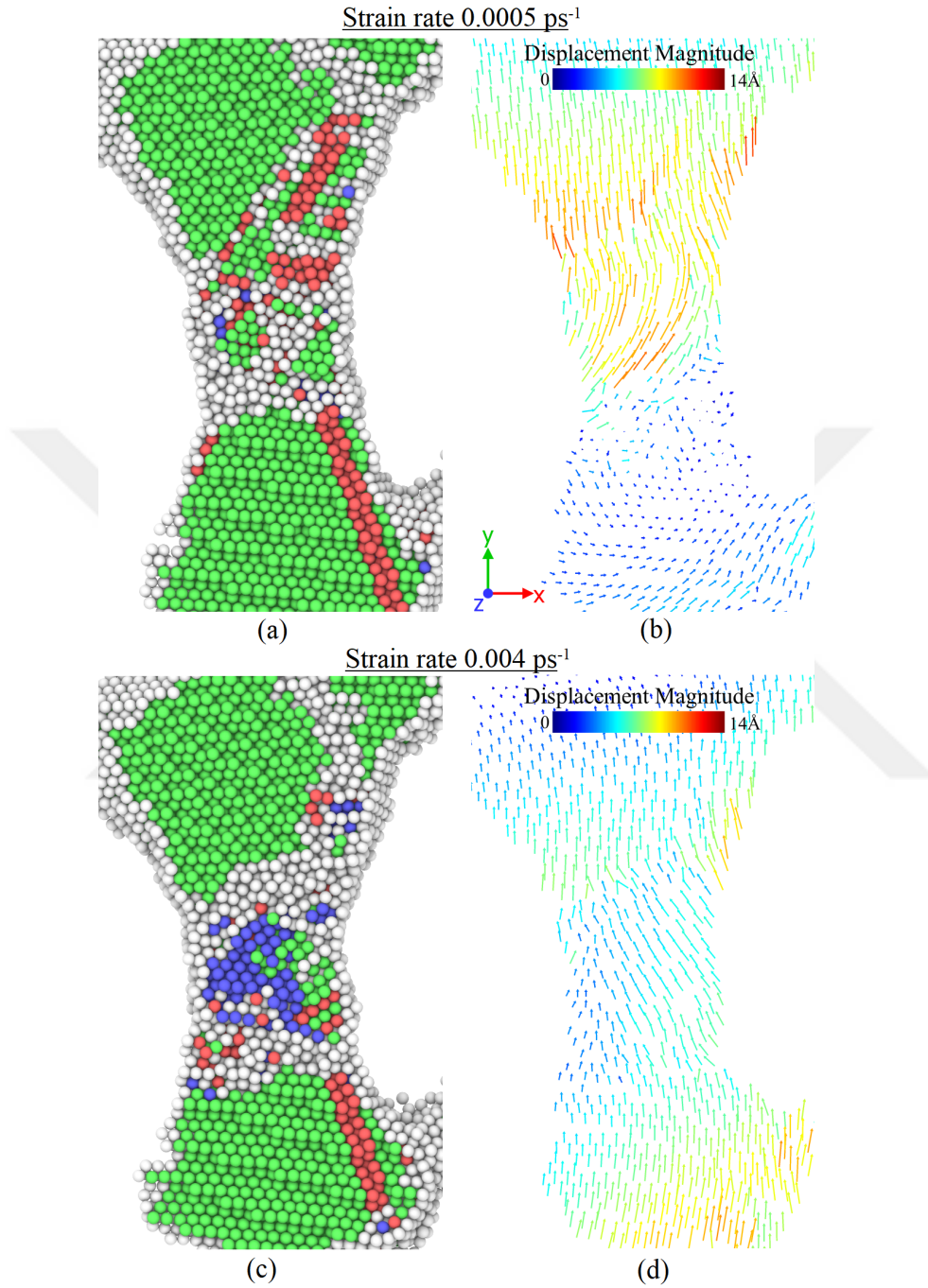
Figure 4.7 : Snapshots of a representative ligament at the same uniform strain level ε=0.125 ((a) and (c) show the results of aCNA analysis, (b) and (d) show the directions of atomic displacements)

It is also clear that the deformation mechanism consists of dislocation movements, grain rotations and grain boundary sliding as Xian et al. [132] mentioned as well. In addition to this fact, the grain boundary travelling is observed especially for the strain rate of 0.5E-3 ps^{-1} (Figure 4.6). Then the rupture is realized as a grain boundary

sliding. It should be noted that in-grain ruptures are rarely observed in the specimens during the investigation of the aCNA results.

4.2.2 Compressive strength of nano-crystalline nanoporous gold

In order to examine the effects of strain rate on the compressive strength, stress-strain curves of the atomistic models subjected to uniaxial compression loading are obtained and presented in Figure 4.8. Furthermore, calculated mechanical properties are given quantitatively in Table 4.2 to perform a solid comparison.

(a) Single-crystalline   (b) Nano-crystalline (gs100)

(c) Nano-crystalline (gs125)   (d) Nano-crystalline (gs150)
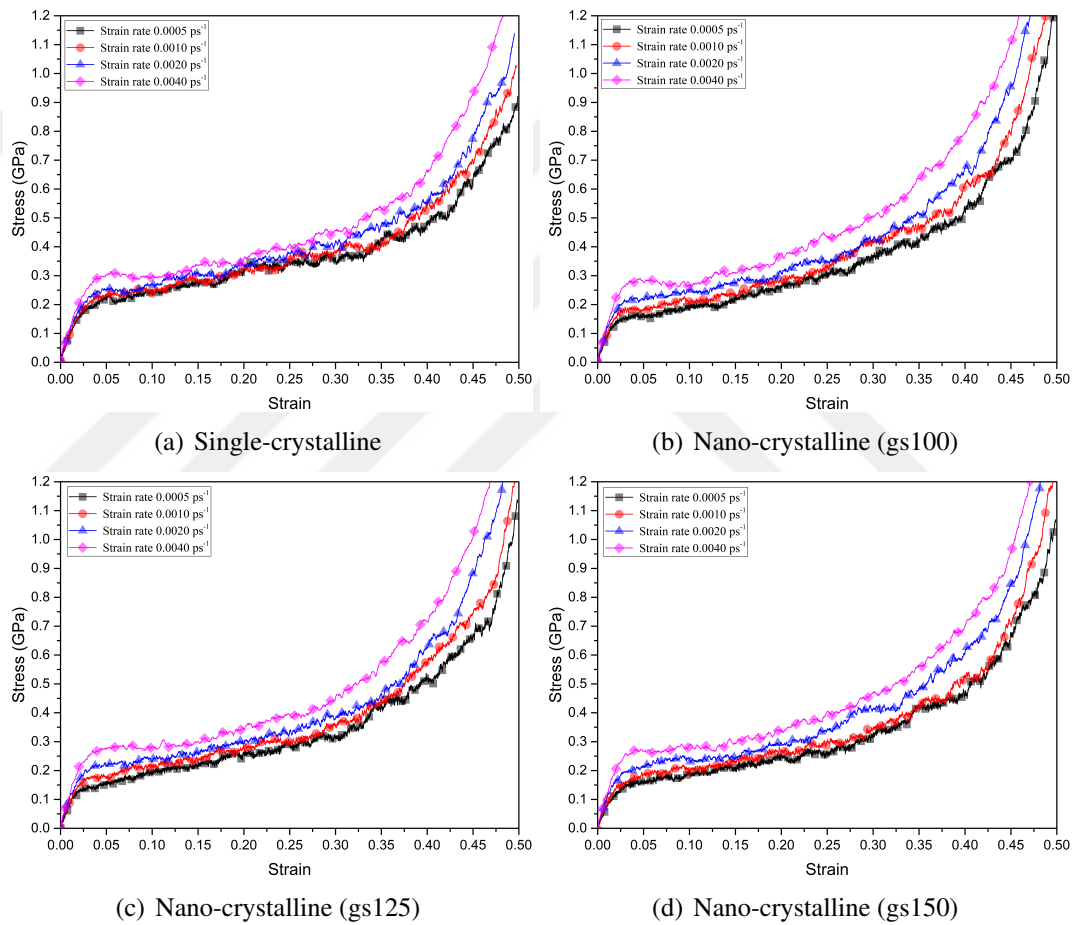
Figure 4.8 : Stress-strain curves at different loading rates for sc- and nc-NPAu.

As also mentioned in previous studies [48, 120], the stress-strain curves represent three distinct regimes which are typical for cellular solids in compression. These regimes are called linear elastic, hardening, and densification. It becomes clear that mechanical properties of all the specimens improved at higher loading rates. Furthermore, we would like to draw your attention to the grain size effect shown in Figure 4.9 where the stress-strain curves of the specimens with varied grain size at the same strain rate are presented. According to this, it can be inferred that the elastic moduli are

Table 4.2 : Mechanical properties of single- and nano-crystalline nanoporous gold for uniaxial compressive loading

	Model name	Strain rate	Modulus of Elasticitiy (GPa)	Yield Strength[*] (GPa)	Yield strain
single crystalline	sc	0.0005	8.05140	0.15457	0.02038
	sc	0.0010	8.62980	0.15822	0.01988
	sc	0.0020	9.83521	0.17951	0.01978
	sc	0.0040	10.55403	0.20791	0.02070
nano crystalline	gs100	0.0005	8.04763	0.12491	0.01721
	gs100	0.0010	8.30271	0.15557	0.02002
	gs100	0.0020	9.83708	0.17266	0.01891
	gs100	0.0040	10.80051	0.23139	0.02266
	gs125	0.0005	7.81709	0.10814	0.01587
	gs125	0.0010	8.23262	0.13485	0.01787
	gs125	0.0020	9.51950	0.16167	0.01867
	gs125	0.0040	10.42121	0.22355	0.02235
	gs150	0.0005	7.43435	0.09572	0.01544
	gs150	0.0010	8.22261	0.12185	0.01636
	gs150	0.0020	9.40953	0.16728	0.01994
	gs150	0.0040	10.44882	0.21722	0.02188

[*] Determination of the yield strength is used the %0.2 offset method.

not affected by the grain size considerably, while the yield stresses are much more sensitive. Moreover, the strain rate plays a huge role for the yield stress. According to stress-strain curves the yield point increases along with the strain rates. Another finding is that nc-NPAu specimens exhibit a good enhancement in the regime of hardening and densification compared with sc-NPAu. This enhancement is more noticeable for high strain rates.

In order to explain the deformation mechanisms of the specimens elaborately, the fractions of the HCP atoms during the compression loading are given in Figure 4.10 for two different loading rates. As mentioned before the density of HCP atoms is strongly related to the stacking faults and the density of partial dislocations. Therefore, according to the aCNA results, it can be noted that there is not any significant change in the quantity of the HCP atoms within the linear elastic regime of the specimens. However, in the hardening regimes, the proportions of the HCP atoms increase rapidly indicating the initiation of plastic deformation. In the following regime, namely the densification regime, the inflating rate of the HCP atom population decreases
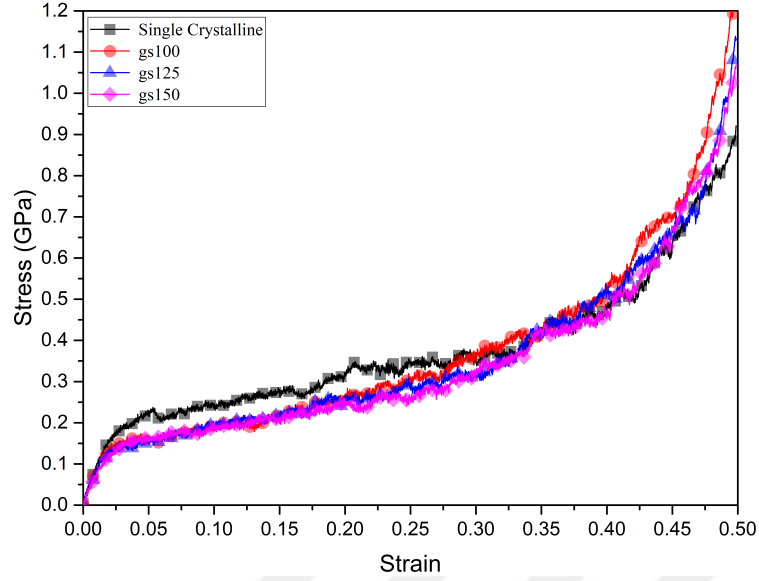
Figure 4.9 : Stress-strain curves at different grain size for sc- and nc-NPAu ($\dot{\varepsilon} =$ 0.5E-3 ps^{-1}.

and finally it turns out to be slightly negative. It should also be mentioned that the reduction in the fraction of the HCP atoms observed in the densification regime does not significantly affect the mechanical response, as densification dominates the behaviour through increasingly hardening.
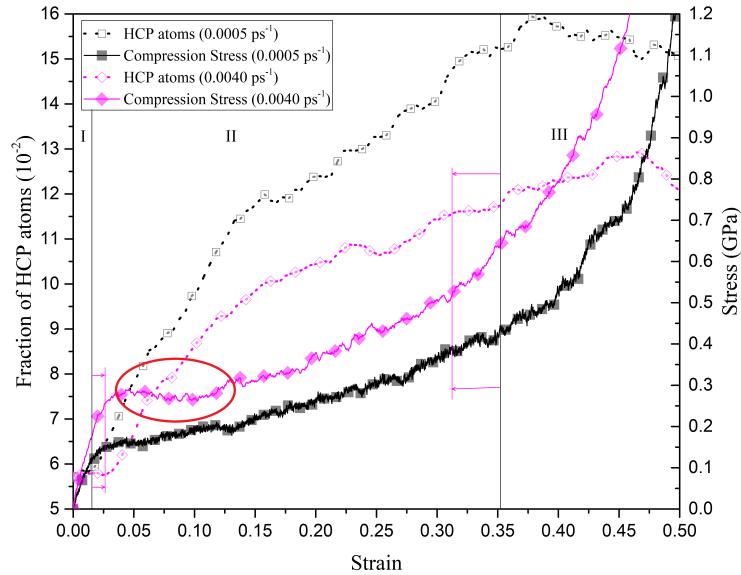
Figure 4.10 : Fraction of HCP atoms of nc-NPAu (gs100) at two compressive strain rates.

Considering the effects of the strain rate on the fractions of the HCP atoms, it is noticed that the high strain rate causes a more distinctive softening regime after the yield point (circled in Figure 4.10)) due to the lower extent of HCP atoms. After that regime, hardening of the specimens by the increase of the percentage of the HCP atoms is

observed. As a result of that the lower loading rate generates more stacking faults, the specimen subjected to the lower strain rate start to yield earlier.

5. ACOUSTICAL PROPERTIES OF PLATINUM AND SILVER COATED NANOPOROUS GOLD

Nanoporous (np) materials as a subset of nanostructured materials possess unique physical, chemical and mechanical properties. Owing to their distinctive properties compared with convential materials, np materials are attracting growing attention of the researchers. Although np materials have low density, their remarkable mechanical characteristics including high hardness and ductility are the most obvious advantages of these structures [28, 29]. Thanks to this advantage, np materials can be widely used in various applications in aviation and defense industries for which the materials with high strength/weight ratio are highly demanded [29]. In addition to this advantage, high surface area/volume ratio of np materials promotes them to be utilized in energy storage, sound insulation and catalysis applications [30,31]. Furthermore, np materials are considered to be well suited for high-end industrial applications such as energy absorber, electrodes and sensor/actuator [32].

Similar to other porous materials, np metals have good sound insulation properties while their thermal, chemical and mechanical properties are much more striking than the ones of other conventional porous materials as polymeric foam or mineral wool used in sound insulation [141]. Although the cost of standard materials used for sound insulation is lower than that of np metals, use of np metals is more advantageous as they provide other properties (i.e. thermal and chemical stability, mechanical strength) required for insulation [16]. In literature, several experimental and numerical studies on the acoustic properties of microporous materials can be found. For example, Pilon et al. experimentally showed that microporous metal foams, especially at high frequencies, were better soundproofing than conventional materials (i.e. fiberglass wool, polyurethane foam, cotton fiber panels, etc.) [141]. Furthermore, Perrot et al. investigated the effectiveness of open-cell aluminum foams for sound insulation at medium and high frequencies by following an optimization approach [142].

In addition to their remarkable properties, coating the free surfaces of np materials with a thin film layer of another functional material improves the physical and chemical performance [49–51]. For example, it is demonstrated that the coating of aluminum oxide with platinum changes its chemical and physical characteristics [52]. In another experimental study, np-gold is coated with copper for the purpose of investigating glucose identification and intuition performance [53].

Experimental studies on np materials and examination of their properties are difficult to carry out due to the high expense of testing equipment used, complexity of procedures and also required experience [36, 43]. For this reason, creating and implementation of atomistic models and numerical experiments are of great importance in the study of the properties and behavior of np materials. At this point, molecular dynamics (MD) simulation technique, which is widely used for the investigation of nanoscale structures, constitute an important numerical tool to examine the characteristics of np materials. In this regard, amongst limited number of numerical studies, Crowson et al. [44] and Kirca et al. [46] propose different atomistic modelling techniques used to determine the properties and mechanical behavior of np metals [45, 47, 48, 143]. The modeling technique, which is utilized in this study, was developed by Yildiz and Kirca [60]. It has a significant advantage of generating atomistic models of coated np structures with desired void ratio (porosity) compared to the other modeling techniques. Using this modeling technique, Yildiz and Kirca [112, 120] studied mechanical properties of np gold coated with platinum and silver by performing comparisons between the mechanical responses of the coated and uncoated specimens.

Although there are several experimental works on the acoustic behavior of np materials [144, 145], to the best of the authors' knowledge, in the literature there exist no numerical study about the acoustic behavior of np materials with or without coating. In fact, numerical modeling of the sound propagation through atomistic simulations is a very new subject. In this regard, Hadjiconstantinou and Garcia [146] presented the first study on this subject, in which the propagation of sound waves in a gaseous environment was examined by "Direct Simulation Monte Carlo" method and the results were compared with the other ones obtained via experimental and approximate analytical solution methods. Yano [147] demonstrated that a harmonic oscillation of a one-dimensional sound source could be investigated by employing Lennard-Jones
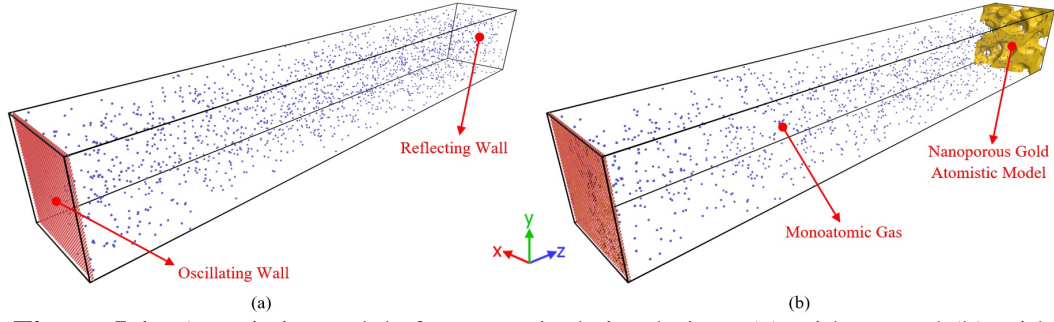
Figure 5.1 : Atomistic models for acoustical simulations (a) without and (b) with nanoporous specimen.

potential. In addition, Ayub et al. [148–150][29–31] studied the propagation of sound waves transmitted at different frequencies through a carbon nanotube by using molecular dynamic simulations.

As also mentioned previously, there are no studies in literature for the acoustic behavior of coated and uncoated np materials. With this motivation, in this study, the acoustic properties of the coated and uncoated np gold under a specific frequency are investigated by performing molecular dynamic simulations. For the purpose of examining the effects of coating, coated and uncoated models at constant porosity are subjected to the same sound frequency. The sound absorption characteristics are examined in a comparative manner by means of sound absorption coefficient-location graphs extracted through molecular dynamic simulations.

5.1 Modeling and Simulation Details

5.1.1 Generation of atomistic models

In order to validate the analysis procedure, at first, the acoustic properties of a monoatomic gas (i.e. argon) are determined and compared with the other studies in literature. For this purpose, a planar sound wave propagating through a monatomic gas within a rectangular domain of length L_z is generated as referenced in the study of Md Ayub [149, 150] (see Figure 5.1). An oscillating wall made of solid argon and a reflecting wall are defined in the simulation domain as shown in Figure 5.1. While the oscillating wall at one end of the simulation box excites the monoatomic gas by imposing a sinusoidally varying velocity, the reflecting wall at the other end reverses the normal component of the particle velocity.

Table 5.1 : Geometric parameters and material types of acoustic models.

Model No	Model Name	Porosity	Core Material	Coating Materials	Coating Thickness	Geometry of Nanoporous Model	Geometry of Acoustic Model
1	Monoatomic Gas (MG)	-	-	-	-	-	200x200x1500 Å
2	np-Au-01	65%	Au	-	-	200x200x100 Å	200x200x1500 Å
3	np-Au-02	50%	Au	-	-	200x200x100 Å	200x200x1500 Å
4	np-Au-03	42%	Au	-	-	200x200x100 Å	200x200x1500 Å
5	Pt@np-Au-01	50%	Au	Pt	4 Å	200x200x100 Å	200x200x1500 Å
6	Pt@np-Au-02	42%	Au	Pt	6 Å	200x200x100 Å	200x200x1500 Å
7	Ag@np-Au-01	50%	Au	Ag	4 Å	200x200x100 Å	200x200x1500 Å
8	Ag@np-Au-02	42%	Au	Ag	6 Å	200x200x100 Å	200x200x1500 Å

In order to examine the dependence of the acoustical property on the porosity and the coating material type, atomistic models of the coated and uncoated nanoporous specimens with different porosities are generated by using the algorithm proposed in the previous study of the authors [60]. Thus, the readers can find detailed information about the atomistic modelling method, which is based on Voronoi tessellation technique in that paper [60].

Three different atomistic models with porosities of 42, 50, 65% are utilized for the acoustic simulations by placing the specimens at the end of the simulation domain as shown in Figure 5.1. Furthermore, different specimens with porosity of 42 and 50% is prepared by coating the np-gold specimens with another metal (i.e. Platinum and Silver) to investigate the change in the acoustic characteristics due to coating as seen in Table 5.1.

5.1.2 Simulation techniques

The molecular dynamics (MD) simulations are carried out by using the open-source code LAMMPS [26, 27] to investigate the acoustic properties of coated and uncoated nanoporous materials subjected to high frequency sound in GHz range (i.e 2.57 GHz). Considering the computational expense, different frequency values are not tested to perform acoustical simulations. The interatomic potentials employed to model the interactions between the atom types (i.e. Argon-Argon, Argon-Gold, Argon-Silver) are described by Lennard-Jones (L-J) 12-6 as shown in Eq 5.1.

$$U(r_{ij}) = 4\varepsilon \left[\left(\frac{\sigma}{r_{ij}} \right)^{12} - \left(\frac{\sigma}{r_{ij}} \right)^{6} \right] \tag{5.1}$$

Table 5.2 : Lennard-Jones potential parameters for the interaction of Ar, Au, Ag and Pt [151–153].

Interaction pair	σ (Å)	ε (eV)
Ar - Ar	3.400	1.03E-02
Ar - Au	3.002	8.64E-03
Ar - Pt	2.940	6.83E-03
Ar - Ag	2.978	6.00E-03

where r_{ij} is the interatomic distance between the atoms i and j; ε and σ are the Lennard-Jones parameters which depend on the type of atom pairs (see Table 5.2). On the other hand, for the interactions between the metal atoms (i.e. Pt-Au, Ag-Au and Au-Au), the EAM (Embedded Atom Method) interatomic potentials are used [85,138]. Furthermore, the interactions between the oscillating wall atoms are described with Lennard-Jones potential, while the cut-off distance between the wall and the gas atoms is set to 3σ so that the oscillating wall behaves like a solid wall.

The oscillating wall moves harmonically along the z-direction. Likewise, the study of Md. Ayub [149, 150], the displacement and the velocity of the oscillating wall are described as a function of time in Eqs. (5.2-5.3).

$$Z_\omega (t) = a (1 - \cos\omega t)$$ (5.2)

$$V_\omega (t) = a\omega \sin\omega t$$ (5.3)

The motion of oscillating wall is governed by the amplitude a and the angular frequency ω.

Before applying the oscillation, the models are thermally equilibrated at 273 K for about 10 ns through the integrator of NVE (microcanonical) ensemble. After the equilibration, the propagating media (i.e. monoatomic gas Argon) is excited by the oscillating solid wall. After the system reaches steady state, the data necessary to calculate the acoustic parameters is collected through the simulation.

5.1.3 Validation of the atomistic model

According to Hadjiconstantinou and Garcia [146], propagation of the plane sound wave generated by the oscillating wall along the z-direction can be described by a spatial and temporal velocity variation given by Eq. 5.4:

$$v_i(z,t) = v_o exp\left[i(\omega t - kz) - mz\right] \tag{5.4}$$

where v_o is the peak value of the gas velocity, which is equal to the velocity of oscillating wall at the boundary (i.e. $v_o = a\omega$); $k = 2\pi/l$ is the wavenumber; l is the acoustic wavelength and m is the attenuation coefficient. Similarly, the plane sound wave reflected from the solid wall at the end of the simulation domain can be described as follow:

$$v_r(z,t) = -v_o exp\left[i(\omega t - k(2L - z)) - m(2L - z)\right] \tag{5.5}$$

If the equations of the incident and reflected waves are superposed, a standing wave of the form can be obtained as referenced in literature [146, 154]

$$v(z,t) = A(z)\sin\omega t + B(z)\cos\omega t \tag{5.6}$$

where

$$A(z) = v_o\left[e^{-mz}\cos kz - e^{-m(2L-z)}\cos k(2L - z)\right] \tag{5.7}$$

$$B(z) = -v_o\left[e^{-mz}\sin kz - e^{-m(2L-z)}\sin k(2L - z)\right] \tag{5.8}$$

The components of the velocity amplitude of the standing wave, which are A(z) and B(z), are stored by using the instantaneous velocity v (z_{jj}, t_{ii}) of the gas molecules within a number of slices taken perpendicular to the z-axis (i.e. along the box length) for each time-step. Here, z_{jj} and t_{ii} represent the position of the slice and the recorded time step, respectively. More details about the equations can be found in study of Hadjiconstantinou and Garcia [146].
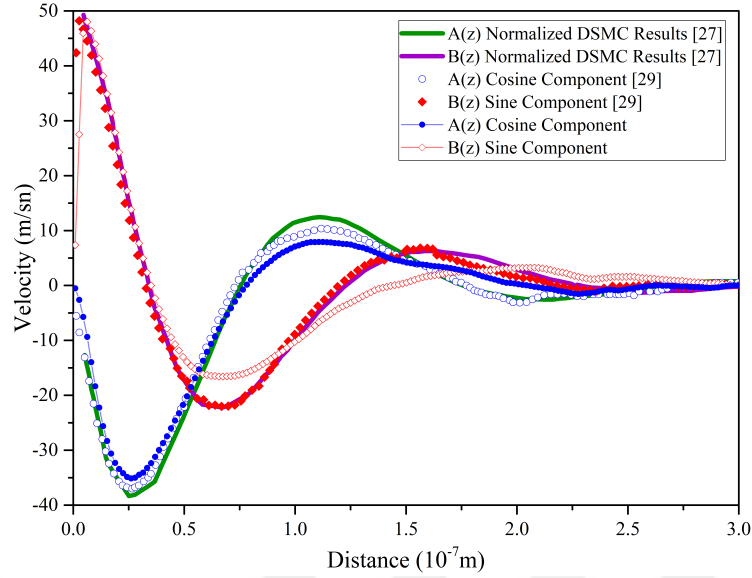
Figure 5.2 : Sine and cosine components of the velocity curves (2.57 GHz and R=0.5).

The velocity components of the standing sound wave obtained for 2.57 GHz frequency and for the acoustic Reynold's number R=0.5 are compared in Figure 5.2 with the results presented in other studies in literature. The preliminary studies show that the velocity components are influenced by many parameters such as amplitude, angular frequency and period of the transmitted sound wave, as well as the other variables such as the sound velocity at the analyzed temperature, gas density, dynamic viscosity, and so on. Although the trends in the velocity profiles are consistent with the other results, some discrepancies are observed in the sinus components which can be attributed to the fact that all of the aforementioned parameters are not explicitly provided in the benchmarking studies.

This comparison shows that the proposed methodology can be used for the acoustic analysis of nano-porous models with sufficient reliability. Although the selected parameters (i.e. sound velocity, gas density, dynamic viscosity etc.) are known to affect the results, the aim of the study is to investigate the effects of the porosity and coating on the acoustic properties. For this reason, same parameters are utilized for the all analysis models.

5.2 Results and Discussions

For the purpose of examining the sound wave propagation, several parameters including average velocity, pressure and temperature for the volumetric slices, which

are defined along the propagation axis of the sound, are collected by recording the position, pressure and velocity values of the atoms. After the average pressure and velocity of each slice in time domain are converted into the frequency domain by means of FFT (fast fourier transform), acoustic parameters (i.e. pressure and velocity profiles, sound absorption coefficient) are obtained by applying the procedure explained in the following paragraphs.

The propagation of the plane wave in a finite simulation box is defined in the frequency domain by Kuipers [155] by the pressure and velocity variations in frequency domain which are given by Eqns. 5.9 and 5.10, respectively.

$$p(z,f) = A_p(f) \; exp^{-ikz} + B_p(f) \; exp^{ikz} = A_p(z,f) + B_p(z,f) \tag{5.9}$$

$$v(z,f) = \frac{1}{\rho c} \left[A_p(f) \; exp^{-ikz} - B_p(f) \; exp^{ikz} \right] = \frac{1}{\rho c} [A_p(z,f) - B_p(z,f)] \tag{5.10}$$

where A_p and B_p are the complex pressure amplitudes of the incident and reflect waves, respectively; z is the spatial coordinate along the propagation direction of the wave; ρ is density of gas; c is velocity of sound; $k = \frac{2\pi f}{c}$ is the wave number and f is the frequency of the wave. Equations 5.9 and 5.10 are solved by Kuipers [155] as follows:

$$A_p(z,f) = \frac{1}{2} [p(z,f) + \rho c \; v(z,f)] \tag{5.11}$$

$$B_p(z,f) = \frac{1}{2} [p(z,f) - \rho c \; v(z,f)] \tag{5.12}$$

Here; $p(z,f)$ and $v(z,f)$ are the Fourier transforms of the expressions $p(z,t)$ and $v(z,t)$ at any position in the simulation domain. The incident and reflected sound intensities can be defined as a function of the A_p and B_p by the following expressions [155].

$$I_{in}(z,f) = \frac{\left| A_p(z,f) \right|^2}{2\rho c} \tag{5.13}$$

$$I_{ref}(z,f) = \frac{\left| B_p(z,f) \right|^2}{2\rho c} \tag{5.14}$$

Then, the sound absorption coefficient $\alpha_L(z)$, which is a function of the position along the propagation axis, can be calculated locally from the incident and reflective sound intensities [155].

$$\alpha_L(z) = 1 - \frac{I_{ref}(z)}{I_{in}(z)} \tag{5.15}$$

In this context, the velocity profiles of all models are illustrated in Figure 5.3 for the wave with 2.57 GHz and acoustic Reynolds number R = 0.5. The total velocity profiles, which refers to the magnitude of the velocities given by Eqn. 5.10, are provided in Figure 5.3.a, while the sine and cosine components of the velocity for each model are given in other graphs. According to Figure 5.3.a, it is noticed that as the porosity decreases, the total velocity (V_T) profiles shrink, which obviously indicates the dependence of the total velocity on the porosity of nanoporous specimens. This observation can be comprehended better by examining the profiles of the sine and cosine components given in Figure 5.3.b which depicts the alteration in the amplitudes of the velocity profiles due to the nanoporous structure placed the end of the simulation box. The nanoporous specimen tends to behave like a reflective material as the porosity decreases. This situation can also be explained by the phase shifts observed on the velocity component profiles, which can be attributed to the porosity change. Another implication of the fact that the surface of the nanoporous material facing with the incident wave acts as a reflector is the converging of the velocity profiles to zero just before the nanoporous structure. Furthermore, the decrease in the amplitude implies that the nanoporous material absorbs some of the sound wave energy. Although the reflective surface area increases at lower porosities, attenuation of the wave amplitude suggests that more energy is absorbed. Indeed, the total velocity curves depicted in Figure 5.3.a point out that there is no significant change as the porosity decreases from 65% to 50%, while the amplitude of the total velocity curve reduces dramatically when the porosity decreases to 40%. Therefore, it can be noted that the sound energy absorption is can be modulated through controlling the porosity.

Examining the response of the coated models given in Figs. 5.3.c and 5.3.d implies that the amplitudes of the velocity components are slightly higher than those of the uncoated models, which may be interpreted as that the coated nanoporous materials are less effective in sound absorption. However, in order to evaluate this situation comprehensively, total velocity (V_T) and pressure (P_T) profiles (see Figs. 5.3.a and 5.4.a) should be assessed together. In this regard, as the amplitude of the total velocity and pressure profiles of the coated specimens are less than those of the uncoated
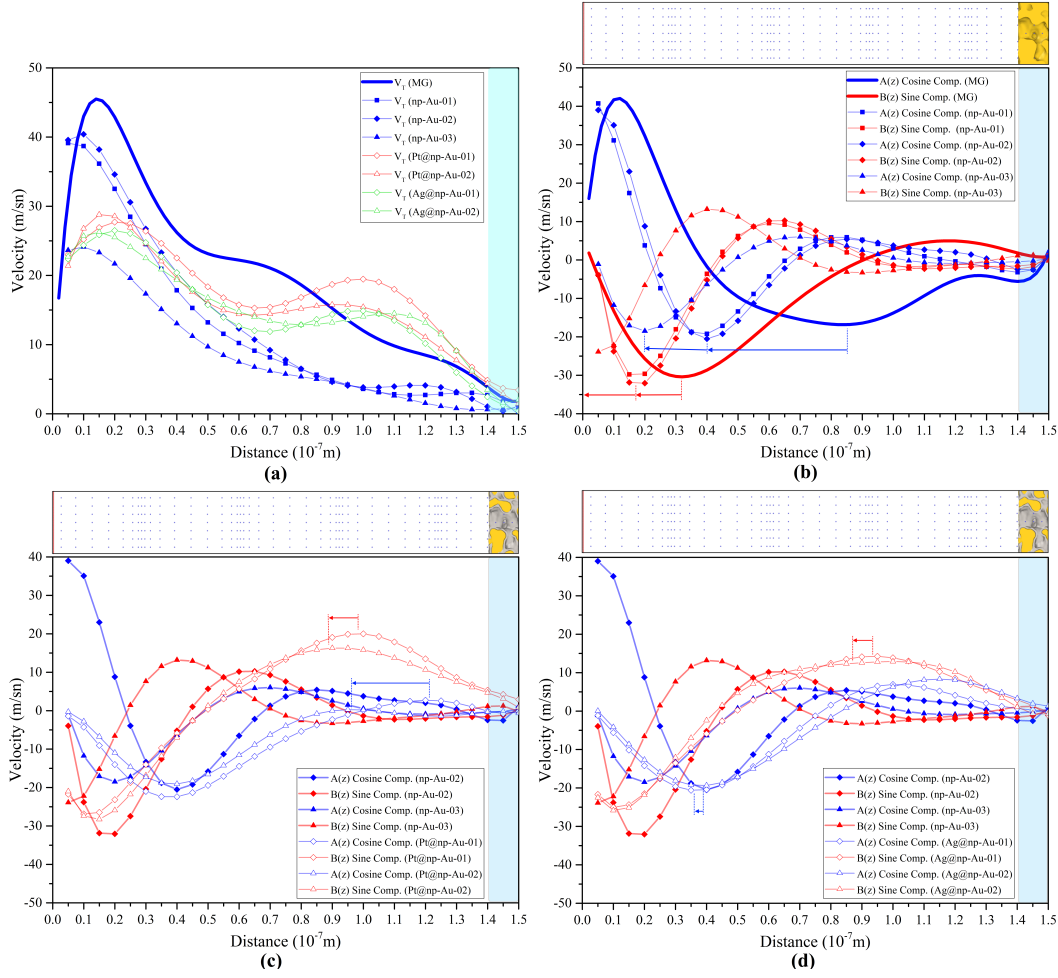
Figure 5.3 : a) Total velocity profiles, Velocity component profiles for b) Nanoporous gold, c) Pt coated nanoporous gold, d) Ag coated nanoporous gold.

specimens, it can be concluded that the sound absorption capacity of the coated specimens is higher.

According to the pressure profiles of the uncoated and coated nanoporous gold specimens presented in Figure 5.4, the coated models present lower amplitudes compared to the uncoated ones, which clearly indicates that the coated specimens absorb more energy. As a result of comparing the coated specimens with each other, it is noticed that the Ag coated models is slightly more efficient in sound absorption at 2.57 GHz frequency. Furthermore, according to the total pressure and velocity graphs, the amplitude is not affected significantly by the thickness of the coating material, which can be regarded as that the sound absorption capacity does not depend on the thickness of coating material. Here, in order to investigate the independent effect of coating material types, comparison is performed for the specimens with the same porosity. Therefore, the porosity differences between the coated models

84
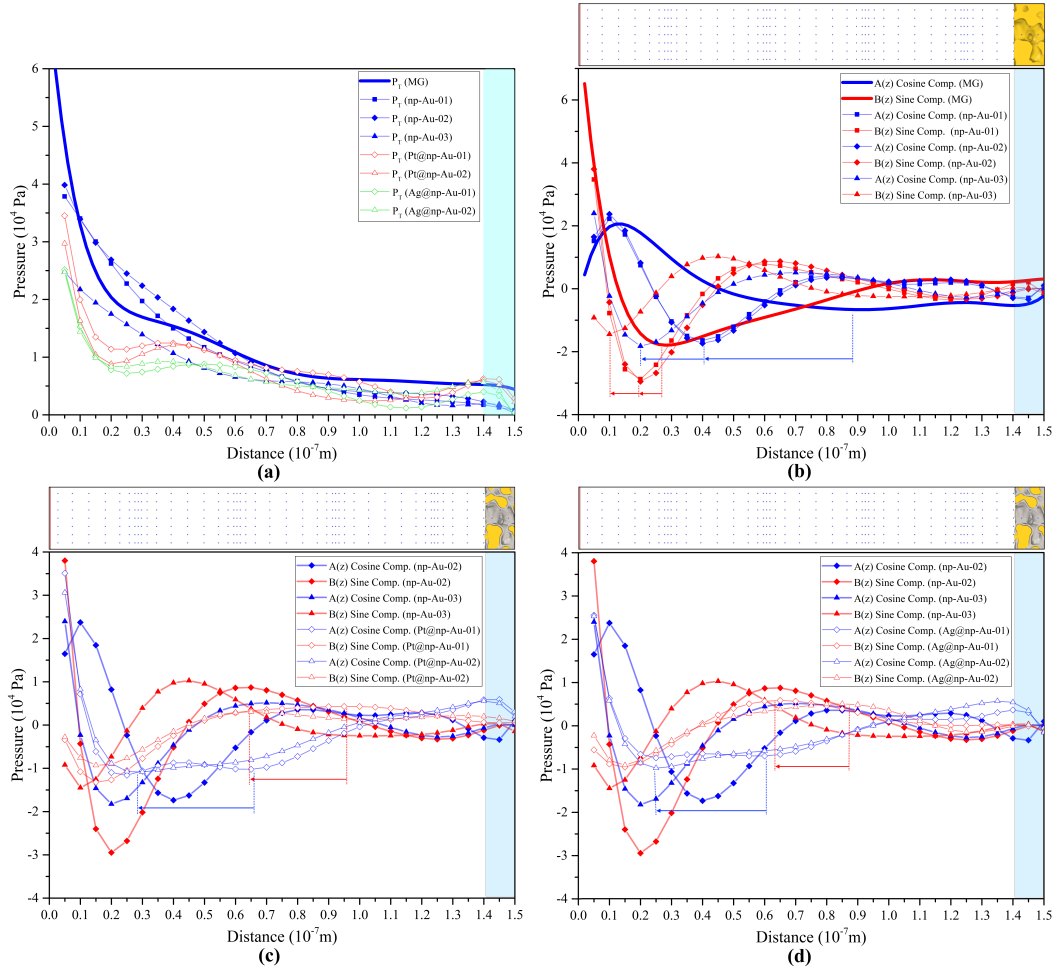
Figure 5.4 : a) Total pressure profiles, Pressure component profiles for b) Nanoporous gold, c) Pt coated nanoporous gold, d) Ag coated nanoporous gold.

(i.e. Pt@np-Au-01 and Pt@np-Au-02) are kept same with the uncoated models (i.e. np-Au-02 and np-Au-03). Although the uncoated model with 42% porosity seems to have a good sound absorption capacity, when the total speed and pressure curves are evaluated together, it is realized that the coated models provide improved sound absorption capacity compared to the uncoated specimens at the same porosity. Moreover, it must be remarked that the phase shifting can also been found in the coated models.

Additionally, spatial variations of the local sound absorption coefficients calculated using equation 5.15 are depicted in Figure 5.5. Here, it should be noted that the sound absorption coefficients are obtained for a single frequency (i.e 2.57 GHz) and for a certain time interval by averaging the results within a local region, which should be taken into account for the evaluation of the obtained results. In this regard, because of the turbulent region formed due to reflection in front of the nanoporous specimen,
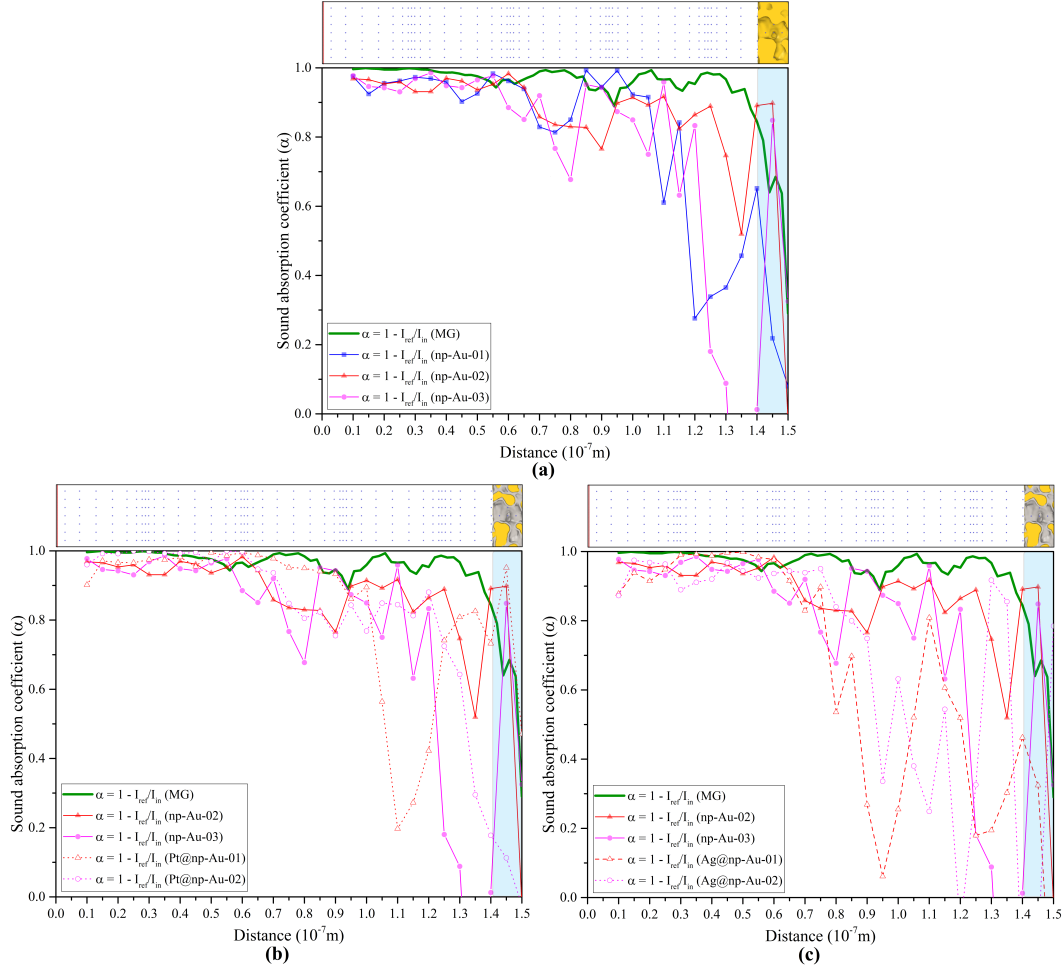
Figure 5.5 : The sound absorption coefficients (α), a) Nanoporous gold, b) Pt coated nanoporous gold, c) Ag coated nanoporous gold.

local sound absorption coefficient calculated for this region includes significant noise, which results in relatively larger fluctuations. Higher noise levels observed at higher porosities can be attributed to the increase of the reflective surface area. Moreover, after examining the variation of the local sound absorption coefficients of the coated models, it can be realized that porosity is not the only parameter affecting the sound absorption capacity but also the type of the coating/base materials play a prominent role.

The differences observed in the sound absorption capacities of Pt/Ag coated and uncoated np-gold, can be explained by considering the potential well width of the materials. As the width of the potential well represents the range of energy absorption [156], the amount of the kinetic energy transferred to the nanoporous structure is expected to be in accordance with the potential well width of the nanoporous material. In the literature [157], the widths of potential wells of Pt, Ag and Au line up as

Au<Pt<Ag which is the same order of the sound absorption capacities of those materials.

6. CONCLUSIONS AND RECOMMENDATIONS

A new method that is mainly based on the Voronoi tessellation technique is introduced to generate atomistic models of randomly structured NPMs. As the main advantage, the proposed method enables the researchers to perform numerical experiments for investigating the physical behavior of coated NPMs. The other important outcome of the method is that the random nature of the nanoporous structures can be imitated by incorporating randomly oriented ligaments and non-uniform mass distribution along the ligaments. Furthermore, statistical data such as length and cross sectional size distribution of ligaments in addition to the number, diameters and angular orientations of the ligaments which may affect the behaviour of the nanoporous structures can be simply traced to evaluate their influence on the material properties quantitatively. As a result of MD simulations performed on the sample atomistic models generated by the proposed method, it has been shown that the models with certain structural parameters keep their original configurations substantially. The parameters such as porosity, minimum Voronoi site distance and coating thickness are investigated as the structural parameters having impact on the conservation of the atomistic configuration and thermodynamic stability.

The proposed atomistic modelling technique can be utilized to generate both uncoated and coated nanoporous structures with highly complex cellular topology by adjusting several parameters including porosity, coating thickness and the minimum Voronoi site distance. Although several numerical approaches exist in literature to obtain the atomistic models of uncoated nanoporous structures, there is no proposed modelling approach to generate coated nanoporous architectures, which gives the opportunity to investigate the effects of coating on the mechanical, thermal and chemical properties of those materials. Besides that, being able to control the cross sectional dimensions and length of the ligaments as well as the thickness of the coating layers can extend the functionality degree of the proposed method. Therefore, based on these advantageous characteristics of the proposed method, it can be efficiently utilized by

future numerical studies with the objective of investigating the effect of coating and structural parameters on the physical properties. Altogether, being aware of the fact that the results of MD simulations must be used with caution when comparing with experiments due to high sensitivity on the mismatch between the real life conditions and the atomistic model. Demonstrated results of this study such as the effects of the coating thickness and porosity on the thermodynamic and structural stability of the specimens can give an idea about the experimental studies focusing on the manufacturing of stable coated and uncoated nanoporous specimens.

After modeling section, the tensile deformation characteristics of coated and uncoated np-Au are obtained through molecular dynamics simulations. In this regard, the effects of coating thickness and material type on the mechanical behavior are examined. Following the MD simulations of uniaxial tensile loading, it is demonstrated that the mechanical properties of np-Au can be enhanced through coating by a different metal. Furthermore, it is also shown that platinum coating provides more significant improvements on the mechanical properties such as toughness and ultimate strength than silver coating. This fact is attributed to the higher density of stacking faults and Lomer-Cottrell locks that act as effective barriers to sessile dislocations resulting in the improvement of the ductility. When considering the deformation at the level of individual ligament, it is mentioned that the orientation of the ligaments with respect to the loading direction is greatly important for the evolution of the defects. In this regard, plastic necking and rupture primarily begin within the ligaments which are aligned with the tensile loading direction. In conclusion, this study provides not only useful insights on the understanding of mechanical behavior and deformation mechanisms of coated and uncoated np-Au but also may present a helpful guide for the further experimental investigations on coating of np materials.

In addition, this study also presents a numerical investigation for the effects of coating on the mechanical behavior and deformation mechanisms of coated nanoporous gold subjected to compression and shear loading by examining the effects of the type and thickness of the coating material. Being independent of the coating material and loading type, the coating thickness is found to cause a favorable effect on the mechanical properties including elastic and shear modulus, yield strength and toughness. The shearing tests show that the enhancement on the shear modulus

maintained by coating is not clearly apparent, especially for Pt-coated specimens. Furthermore, the compression tests demonstrated that the silver coating enhances the mechanical characteristics at all deformation regimes (i.e., linear elastic, softening, densification), while the platinum coating with the same coating thickness produces a negative effect on the yield strength due to the effect of high dislocation density. Therefore, it can be concluded that the compressive and shear properties of coated nanoporous gold are critically dependent on the type of coating material, while the choice of the coating and core materials primarily depends on the purpose of use.

Furthermore, in order to obtain the atomistic model of nanocrystalline nanoporous materials, the proposed modeling technique is enhanced. nc-NPAu atomistic models are generated by using this developed generation algorithm. In order to ensure that that all atomistic models are stable, thermalization was subjected prior to the loading process. Following the thermalization step, each nanoporous sample was subjected to a uniaxial tensile and compressive loading with a constant strain increment. All atomistic models were stretched by 50% of their length and for each loading step, the atomic stresses were calculated by using Virial Stress theorem. In this way, the tensile and compressive behavior of these materials was obtained. As a result, toughness, ultimate and yield stresses show an enhancement with increasing strain rate for both loading type. The small changing on the elastic modulus of nc-NPAu is revealed for the different strain rates. Moreover, the study points out that the deformation mechanism is not only a combination of dislocation movements, grain rotations, and grain boundary sliding but also additionally grain traveling. The mentioned new atomistic modeling technique can be used to generate not only nanoporous gold materials, but also other nano-crystalline NPMs. In this way, this technique gives an opportunity to investigate the mechanical, thermal and chemical properties of the granular structures. This method can be efficiently used in future numerical studies to investigate the effect of the granular structure of nanoporous metals.

Finally, the acoustical properties of the Pt and Ag coated and uncoated np-Au are presented in this dissertation. According to acoustical analyses, the velocity and pressure profiles, the local sound absorption coefficients are calculated for all models. The obtained findings indicate that the nanoporous materials absorb the sound energy from the simulation domain despite the fact that they behave like a reflector and it

shows that the proportional of energy absorption relies on the porosity of nanoporous material. In addition, the coating materials also play a huge role in the sound energy damping. The silver coating is slightly more effective to decrease the sound level compared with the platinum one. The different thicknesses of coating materials do not show a remarkable enhancement on the sound absorption performance. The local sound absorption coefficient graphs caused by the uncoated/coated nanoporous material shows big fluctuations in front of the nanoporous model. These fluctuations are increased with the porosity of the atomistic model. For a better understanding of the acoustic properties of these materials, similar analyses can be performed with different frequencies. For the time being, the computer facilities are very limited for these analyses. The author believes that the evolving computer facilities will give many opportunities in this field.

In the future, nanoporous materials with different materials and thicknesses can be modeled by using the developed modeling method. Furthermore, except for determining the mechanical and acoustical properties, many properties such as thermal and electrical conductivity can be also detected.

REFERENCES

[1] **Rizvi, S.A.A. and Saleh, A.M.** (2018). Applications of nanoparticle systems in drug delivery technology., *Saudi pharmaceutical journal : SPJ : the official publication of the Saudi Pharmaceutical Society*, *26*(1), 64–70.

[2] **Patra, J.K.**, **Das, G.**, **Fraceto, L.F.**, **Campos, E. and Vangelie, R.** (2018). Nano based drug delivery systems: recent developments and future prospects, *Journal of Nanobiotechnology*, *16*(1), 71.

[3] **Kumar, A.**, **Gupta, K.**, **Dixit, S.**, **Mishra, K. and Srivastava, S.** (2018). A review on positive and negative impacts of nanotechnology in agriculture, *International Journal of Environmental Science and Technology*, 1–10.

[4] **Zhang, Q.**, **Bai, Z.**, **Du, F. and Dai, L.** (2019). Carbon Nanotube Energy Applications, *Nanotube Superfiber Materials*, 695–728.

[5] **Jibowu, T.** (2016). A Review on Nanoporous Metals, *Frontiers in Nanoscience and Nanotechnology*, *2*(4).

[6] **Zhang, J.**, **Li, C.M. and Erlebacher, J.** (2012). Nanoporous metals: fabrication strategies and advanced electrochemical applications in catalysis, sensing and energy systems, *Chemical Society Reviews*, *41*(21), 7016.

[7] **Lang, X.**, **Hirata, A.**, **Fujita, T. and Chen, M.** (2011). Nanoporous metal/oxide hybrid electrodes for electrochemical supercapacitors, *Nature Nanotechnology*, *6*(4), 232–236.

[8] **Biener, J.**, **Wittstock, A.**, **Zepeda-Ruiz, L.A.**, **Zialesk, V. and Kramer, D.** (2009). Surface-chemistry-driven actuation in nanoporous gold, *Nature Materials*, *8*(1), 47–51.

[9] **Boomsma, K.**, **Poulikakos, D. and Zwick, F.** (2003). Metal foams as compact high performance heat exchangers, *Mechanics of Materials*, *35*(12), 1161–1176.

[10] **Lu, T.**, **Stone, H. and Ashby, M.** (1998). Heat transfer in open-cell metal foams, *Acta Materialia*, *46*(10), 3619–3635.

[11] **Juarez, T.**, **Biener, J.**, **Weissmüller, J. and Hodge, A.M.** (2017). Nanoporous Metals with Structural Hierarchy: A Review, *Advanced Engineering Materials*, *19*(12).

[12] **Banhart, J.** (2013). Light-Metal Foams-History of Innovation and Technological Challenges, *Advanced Engineering Materials*, *15*(3), 82–111.

[13] **Gama, B.A.**, **Bogetti, T.A.**, **Fink, B.K.**, **Yu, C.J.**, **Dennis Claar, T.**, **Eifert, H.H. and Gillespie Jr, J.W.** (2001). Aluminum foam integral armor: a new dimension in armor design, *Composite Structures*, *52*(3-4), 381–395.

[14] **Ding, Y.**, **Chen, M.**, **Polarz, S. and Smarsly, B.** (2009). Nanoporous Metals for Catalytic and Optical Applications, *MRS Bulletin*, *34*(08), 569–576.

[15] **Schaedler, T.A. and Carter, W.B.** (2016). Architected Cellular Materials, *Annual Review of Materials Research*, *46*(1), 187–210.

[16] **Lefebvre, L.P.**, **Banhart, J. and Dunand, D.** (2008). Porous Metals and Metallic Foams: Current Status and Recent Developments, *Advanced Engineering Materials*, *10*(9), 775–787.

[17] **Zhou, J.** (2007). *Porous Metallic Materials*, CRC Press.

[18] **Erlebacher, J.** (2004). An Atomistic Description of Dealloying, *Journal of The Electrochemical Society*, *151*(10), C614.

[19] **Guan, C. and Wang, J.** (2016). Recent Development of Advanced Electrode Materials by Atomic Layer Deposition for Electrochemical Energy Storage, *Advanced Science*, *3*(10).

[20] **Zeis, R.**, **Mathur, A.**, **Fritz, G.**, **Lee, J. and Erlebacher, J.** (2007). Platinum-plated nanoporous gold: An efficient, low Pt loading electrocatalyst for PEM fuel cells, *Journal of Power Sources*, *165*(1), 65–72.

[21] **Hodge, A.**, **Doucette, R.**, **Biener, M.**, **Biener, J. and Hamza, A.V.** (2009). Ag effects on the elastic modulus values of nanoporous Au foams, *Journal of Materials Research*, *24*(04), 1600–1606.

[22] **Chan, S.**, **Kwon, S.**, **Koo, T.W.**, **Lee, L. and Berlin, A.** (2003). Surface-Enhanced Raman Scattering of Small Molecules from Silver-Coated Silicon Nanopores, *Advanced Materials*, *15*(19), 1595–1598.

[23] **Chen, A.Y.**, **Shi, S.S. and Wang, J.W.** (2016). Microstructure and electrocatalytic performance of nanoporous gold foils decorated by TiO_2 coatings, *Surface and Coatings Technology*, *286*, 113–118.

[24] **Frenkel, D. and Smit, B.** *Understanding molecular simulation : from algorithms to applications*.

[25] **Verlet, L.** (1967). Computer "Experiments"; on Classical Fluids. I. Thermodynamical Properties of Lennard-Jones Molecules, *Physical Review*, *159*(1), 98–103.

[26] **Plimpton, S.** (1995). Fast Parallel Algorithms for Short-Range Molecular Dynamics, *Journal of Computational Physics*, *117*(1), 1–19.

[27] **LAMMPS**, `http://lammps.sandia.gov/`, alındığı tarih: 2019.

[28] **Rao, C.N.R. and Cheetham, A.K.** (2001). Science and technology of nanomaterials: current status and future prospects, *Journal of Materials Chemistry*, *11*(11), 2887–2894.

[29] **Rodriguez-Nieva, J.F.**, **Ruestes, C.J.**, **Tang, Y. and Bringa, E.M.** (2014). Atomistic simulation of the mechanical properties of nanoporous gold, *Acta Materialia*, *80*, 67–76.

[30] **Lu, G.Q. and Zhao, X.S.** (2004). *Nanoporous Materials - An Overview*, Imperial College Press.

[31] **Kim, S.C.**, **Kim, D.S.**, **Oh, S.S.**, **Lee, D.K. and Yang, Y.K.** (2003). *Science and Technology in Catalysis 2002, Proceedings of the Fourth Tokyo conference on Advance Catalytic Science and Technology*, volume145 of *Studies in Surface Science and Catalysis*, Elsevier.

[32] **Logar, N.Z. and Kaučič, V.** (2006). Nanoporous materials: from catalysis and hydrogen storage to wastewater treatment, *Acta Chimica Slovenica*, *53*, 117–135.

[33] **Biener, J.**, **Hodge, A.M.**, **Hayes, J.R.**, **Cynthia, A. and Luis, A.** (2006). Size effects on the mechanical behavior of nanoporous Au, *Nano letters*, *6*(10), 2379–2382.

[34] **Punzhin, S.**, **Detsi, E.**, **Kuzmin, A. and De Hosson, J.T.M.** (2014). Deformation of nanoporous nanopillars by ion beam-induced bending, *Journal of Materials Science*, *49*(16), 5598–5605.

[35] **Uchic, M.D.**, **Dimiduk, D.M.**, **Florando, J.N. and Nix, W.D.** (2004). Sample Dimensions Influence Strength and Crystal Plasticity, *Science*, *305*(5686).

[36] **Erhart, P.**, **Bringa, E.M.**, **Kumar, M. and Albe, K.** (2005). Atomistic mechanism of shock-induced void collapse in nanoporous metals, *Physical Review B*, *72*(5), 52104.

[37] **Reisman, D.B.**, **Wolfer, W.G.**, **Elsholz, A. and Furnish, M.D.** (2003). Isentropic compression of irradiated stainless steel on the Z accelerator, *Journal of Applied Physics*, *93*(11), 8952.

[38] **Gurson, A.L.** (1977). Continuum Theory of Ductile Rupture by Void Nucleation and Growth: Part I—Yield Criteria and Flow Rules for Porous Ductile Media, *Journal of Engineering Materials and Technology*, *99*(1), 2.

[39] **Wen, J.** (2005). The modified Gurson model accounting for the void size effect, *International Journal of Plasticity*, *21*(2), 381–395.

[40] **Bhatia, M.A.**, **Solanki, K.N.**, **Moitra, A. and Tschopp, M.A.** (2012). Investigating Damage Evolution at the Nanoscale: Molecular Dynamics Simulations of Nanovoid Growth in Single-Crystal Aluminum, *Metallurgical and Materials Transactions A*, *44*(2), 617–626.

[41] **Traiviratana, S.**, **Bringa, E.M.**, **Benson, D.J. and Meyers, M.A.** (2008). Void growth in metals: Atomistic calculations, *Acta Materialia*, *56*(15), 3874–3886.

[42] **Tang, Y.**, **Bringa, E.M. and Meyers, M.A.** (2012). Ductile tensile failure in metals through initiation and growth of nanosized voids, *Acta Materialia*, *60*(12), 4856–4865.

[43] **Crowson, D.**, **Farkas, D. and Corcoran, S.** (2007). Geometric relaxation of nanoporous metals: The role of surface relaxation, *Scripta Materialia*, *56*(11), 919–922.

[44] **Crowson, D.A.**, **Farkas, D. and Corcoran, S.G.** (2009). Mechanical stability of nanoporous metals with small ligament sizes, *Scripta Materialia*, *61*(5), 497–499.

[45] **Farkas, D.**, **Caro, A.**, **Bringa, E. and Crowson, D.** (2013). Mechanical response of nanoporous gold, *Acta Materialia*, *61*(9), 3249–3256.

[46] **Kirca, M.**, **Gul, A.**, **Ekinci, E.**, **Yardım, F. and Mugan, A.** (2007). Computational modeling of micro-cellular carbon foams, *Finite Elements in Analysis and Design*, *44*(1-2), 45–52.

[47] **To, A.C.**, **Tao, J.**, **Kirca, M. and Schalk, L.** (2011). Ligament and joint sizes govern softening in nanoporous aluminum, *Applied Physics Letters*, *98*(5), 51903.

[48] **Giri, A.**, **Tao, J.**, **Wang, L.**, **Kirca, M. and To, A.C.** (2014). Compressive Behavior and Deformation Mechanism of Nanoporous Open-Cell Foam with Ultrathin Ligaments, *Journal of Nanomechanics and Micromechanics*, *4*(2), A4013012.

[49] **Adomaitis, R.A.** (2010). Development of a multiscale model for an atomic layer deposition process, *Journal of Crystal Growth*, *312*(8), 1449–1452.

[50] **Biener, M.M.**, **Biener, J.**, **Wichmann, A.**, **Arne, W. and Theodore, F.B.** (2011). ALD functionalized nanoporous gold: thermal stability, mechanical properties, and catalytic activity., *Nano letters*, *11*(8), 3085–3090.

[51] **Kang, H.J.**, **Kim, D.J.**, **Park, S.J.**, **Yoo, J.B. and Ryu, Y.S.** (2007). Controlled drug release using nanoporous anodic aluminum oxide on stent, *Thin Solid Films*, *515*(12), 5184–5187.

[52] **Qian, L.**, **Shen, W.**, **Das, B.**, **Shen, B. and Qin, G.W.** (2009). Alumina coating of ultrafine nanoporous gold at room temperature and their optical properties, *Chemical Physics Letters*, *479*(4-6), 259–263.

[53] **Guo, M.m.**, **Wang, P.s.**, **Zhou, C.h.**, **Xia, Y.**, **Huang, W. and Li, Z.** (2014). An ultrasensitive non-enzymatic amperometric glucose sensor based on a Cu-coated nanoporous gold film involving co-mediating, *Sensors and Actuators B: Chemical*, *203*, 388–395.

[54] **Zechner, J.**, **Mohanty, G.**, **Frantz, C.**, **Cebeci, H.**, **Philippe, L. and Michler, J.** (2014). Mechanical properties and interface toughness of metal filled nanoporous anodic aluminum oxide coatings on aluminum, *Surface and Coatings Technology*, *260*, 246–250.

[55] **Li, Z.**, **Zhang, J.**, **Fan, J.**, **Wang, Z. and Zhao, L.** (2014). On crushing response of the three-dimensional closed-cell foam based on Voronoi model, *Mechanics of Materials*, *68*, 85–94.

[56] **Song, Y.**, **Wang, Z.**, **Zhao, L. and Luo, J.** (2010). Dynamic crushing behavior of 3D closed-cell foams based on Voronoi random model, *Materials {&} Design*, *31*(9), 4281–4289.

[57] **Wejrzanowski, T.**, **Skibinski, J.**, **Szumbarski, J. and Kurzydlowski, K.J.** (2013). Structure of foams modeled by Laguerre–Voronoi tessellations, *Computational Materials Science*, *67*, 216–221.

[58] **Redenbach, C.**, **Shklyar, I. and Andrä, H.** (2012). Laguerre tessellations for elastic stiffness simulations of closed foams with strongly varying cell sizes, *International Journal of Engineering Science*, *50*(1), 70–78.

[59] **Schladitz, K.**, **Redenbach, C.**, **Sych, T. and Godehardt, M.** (2012). Model Based Estimation of Geometric Characteristics of Open Foams, *Methodology and Computing in Applied Probability*, *14*(4), 1011–1032.

[60] **Yildiz, Y.O. and Kirca, M.** (2017). Atomistic simulation of Voronoi-based coated nanoporous metals, *Modelling and Simulation in Materials Science and Engineering*, *25*(2), 025008.

[61] **Leonardi, A.**, **Scardi, P. and Leoni, M.** (2012). Realistic nano-polycrystalline microstructures: beyond the classical Voronoi tessellation, *Philosophical Magazine*, *92*(8), 986–1005.

[62] **Fan, Z.**, **Wu, Y.**, **Zhao, X. and Lu, Y.** (2004). Simulation of polycrystalline structure with Voronoi diagram in Laguerre geometry based on random closed packing of spheres, *Computational Materials Science*, *29*(3), 301–308.

[63] **Wu, Y.**, **Zhou, W.**, **Wang, B. and Yang, F.** (2010). Modeling and characterization of two-phase composites by Voronoi diagram in the Laguerre geometry based on random close packing of spheres, *Computational Materials Science*, *47*(4), 951–961.

[64] **Fritzen, F.**, **Böhlke, T. and Schnack, E.** (2009). Periodic three-dimensional mesh generation for crystalline aggregates based on Voronoi tessellations, *Computational Mechanics*, *43*(5), 701–713.

[65] **Møller, J.** (1994). *Lectures on Random Voronoi Tessellations*, volume 87 of *Lecture Notes in Statistics*, Springer New York, New York, NY.

[66] **Yang, R.Y.**, **Zou, R.P. and Yu, A.B.** (2002). Voronoi tessellation of the packing of fine uniform spheres, *Physical Review E*, *65*(4), 041302.

[67] **Xu, T. and Li, M.** (2009). Topological and statistical properties of a constrained Voronoi tessellation, *Philosophical Magazine*, *89*(4), 349–374.

[68] **Aurenhammer, F.** (1991). Voronoi diagrams—a survey of a fundamental geometric data structure, *ACM Computing Surveys*, *23*(3), 345–405.

[69] **Okabe, A.** (2000). *Spatial tessellations : concepts and applications of Voronoi diagrams*, Wiley, 2nd editio edition.

[70] **Stoyan, D.**, **Chiu, S.N.**, **Kendall, W.S. and Mecke, J.** (2013). *Stochastic geometry and its applications.*, Wiley, 3rd edition edition.

[71] **Zhu, H. and Windle, A.** (2002). Effects of cell irregularity on the high strain compression of open-cell foams, *Acta Materialia*, *50*(5), 1041–1052.

[72] **Zhu, H.**, **Hobdell, J. and Windle, A.** (2000). Effects of cell irregularity on the elastic properties of open-cell foams, *Acta Materialia*, *48*(20), 4893–4900.

[73] **Finney, J.** (1975). Volume occupation, environment and accessibility in proteins. The problem of the protein surface, *Journal of Molecular Biology*, *96*(4), 721–732.

[74] **Icke, V.** (1996). Particles, space, and time, *Astrophysics and Space Science*, *244*(1-2), 293–311.

[75] **Getis, A. and Boots, B.** (2008). *Models of Spatial Processes:An Approach to the Study of Point, Line and Area Patterns*, Cambridge University Press.

[76] **Arsie, A. and Frazzoli, E.** (2008). Efficient routing of multiple vehicles with no explicit communications, *International Journal of Robust and Nonlinear Control*, *18*(2), 154–164.

[77] **Ho, K.C.**, **Zhang, N.**, **Lin, J. and Dean, T.A.** (2007). An Integrated Approach for Virtual Microstructure Generation and Micro-Mechanics Modelling for Micro-Forming Simulation, *First International Conference on Integration and Commercialization of Micro and Nanosystems, Parts A and B*, ASME, pp.203–211.

[78] **Rycroft, C.H.** (2007). Multiscale modeling in granular flow, *Ph.D. thesis*, Massachusetts Institute of Technology, Cambridge, MA.

[79] **Du, Q.**, **Faber, V. and Gunzburger, M.** (1999). Centroidal Voronoi Tessellations: Applications and Algorithms, *SIAM Review*, *41*(4), 637–676.

[80] **Barber, C.B.**, **Dobkin, D.P. and Huhdanpaa, H.** (1996). The quickhull algorithm for convex hulls, *ACM Transactions on Mathematical Software*, *22*(4), 469–483.

[81] **Li, R. and Sieradzki, K.** (1992). Ductile-brittle transition in random porous Au, *Physical Review Letters*, *68*(8), 1168–1171.

[82] **Ding, Yi and Jonah, E.** (2003). Nanoporous Metals with Controlled Multimodal Pore Size Distribution, *J. Am. Chem. Soc.*, *125*(26), 7772–7773.

[83] **Ding, T.**, **Yao, L.**, **Liu, C. and Ciriminna, R.** (2016). Kinetically-controlled synthesis of ultra-small silica nanoparticles and ultra-thin coatings, *Nanoscale*, *8*(8), 4623–4627.

[84] **Stoldt, C.R.**, **Bright, V.M. and Sniegowski, J.J.** (2006). Ultra-thin film encapsulation processes for micro-electro-mechanical devices and systems, *Journal of Physics D: Applied Physics*, *39*(9), R163—-R170.

[85] **Zhou, X.W.**, **Johnson, R.A. and Wadley, H.N.G.** (2004). Misfit-energy-increasing dislocations in vapor-deposited CoFe/NiFe multilayers, *Physical Review B*, *69*(14), 144113.

[86] **Thompson, A.P.**, **Plimpton, S.J. and Mattson, W.** (2009). General formulation of pressure and stress tensor for arbitrary many-body interaction potentials under periodic boundary conditions, *The Journal of Chemical Physics*, *131*(15), 154107.

[87] **Liu, R. and Antoniou, A.** (2012). A relation between relative density, alloy composition and sample shrinkage for nanoporous metal foams, *Scripta Materialia*, *67*(12), 923–926.

[88] **Liu, R. and Antoniou, A.** (2013). A relationship between the geometrical structure of a nanoporous metal foam and its modulus, *Acta Materialia*, *61*(7), 2390–2402.

[89] **Gupta, G.**, **Thorp, J.C.**, **Mara, N.A.**, **Dattelbaum, A.M.**, **Misra, A. and Picraux, S.T.** (2012). Morphology and porosity of nanoporous Au thin films formed by dealloying of AuxSi1-x, *Journal of Applied Physics*, *112*(9), 94320.

[90] **Mathur, A. and Erlebacher, J.** (2007). Size dependence of effective Young's modulus of nanoporous gold, *Applied Physics Letters*, *90*(6), 61910.

[91] **Biener, J.**, **Hamza, A.V. and Hodge, A.M.** (2008). *Micro and Nano Mechanical Testing of Materials and Devices*, Springer US.

[92] **Faken, D. and Jónsson, H.** (1994). Systematic analysis of local atomic structure combined with 3D computer graphics, *Computational Materials Science*, *2*(2), 279–286.

[93] **Stukowski, A.** (2012). Structure identification methods for atomistic simulations of crystalline materials, *Modelling and Simulation in Materials Science and Engineering*, *20*(4), 45021.

[94] **Stukowski, A.** (2010). Visualization and analysis of atomistic simulation data with OVITO–the Open Visualization Tool, *Modelling and Simulation in Materials Science and Engineering*, *18*(1), 15012.

[95] **Sansoz, F.** (2011). Atomistic processes controlling flow stress scaling during compression of nanoscale face-centered-cubic crystals, *Acta Materialia*, *59*(9), 3364–3372.

[96] **Hull, D.**, **Bacon, D.J.**, **Hull, D. and Bacon, D.J.** (2011). *Dislocations in Face-centered Cubic Metals*, Butterworth-Heinemann.

[97] **Winter, N.**, **Becton, M.**, **Zhang, L. and Wang, X.** (2016). Failure Mechanisms and Scaling Laws of Nanoporous Aluminum: A Computational Study, *Advanced Engineering Materials*, *18*(4), 632–642.

[98] **Balk, T.J.**, **Eberl, C.**, **Sun, Y.**, **Hemker, K.J. and Gianola, D.S.** (2009). Tensile and compressive microspecimen testing of bulk nanoporous gold, *JOM*, *61*(12), 26–31.

[99] **Briot, N.J.**, **Kennerknecht, T.**, **Eberl, C. and Balk, T.J.** (2014). Mechanical properties of bulk single crystalline nanoporous gold investigated by millimetre-scale tension and compression testing, *Philosophical Magazine*, *94*(8), 847–866.

[100] **Biener, J.**, **Hodge, A.M.**, **Hamza, A.V.**, **Hsiung, L.M. and Satcher, J.H.** (2005). Nanoporous Au: A high yield strength material, *Journal of Applied Physics*, *97*(2), 024301.

[101] **Lee, D.**, **Wei, X.**, **Chen, X.**, **Zhao, M.**, **Jun, S.**, **Hone, J.**, **Herbert, E.G.**, **Oliver, W.C. and Kysar, J.W.** (2007). Microfabrication and mechanical properties of nanoporous gold at the nanoscale, *Scripta Materialia*, *56*(5), 437–440.

[102] **Gibson, L. and Ashby, M.** (1999). *Cellular Solids:Structure and Properties*, Cambridge : Cambridge University Press, 2nd editio edition.

[103] **Sun, X.Y.**, **Xu, G.K.**, **Li, X.**, **Feng, X.Q. and Gao, H.** (2013). Mechanical properties and scaling laws of nanoporous gold, *Journal of Applied Physics*, *113*(2), 023505.

[104] **Jin, H.J. and Weissmüller, J.** (2010). Bulk Nanoporous Metal for Actuation, *Advanced Engineering Materials*, *12*(8), 714–723.

[105] **Jiao, J. and Huber, N.** (2017). Deformation mechanisms in nanoporous metals: Effect of ligament shape and disorder, *Computational Materials Science*, *127*, 194–203.

[106] **Qian, L.H. and Chen, M.W.** (2007). Ultrafine nanoporous gold by low-temperature dealloying and kinetics of nanopore formation, *Applied Physics Letters*, *91*(8), 083105.

[107] **Ding, Y.**, **Chen, M. and Erlebacher, J.** (2004). Metallic Mesoporous Nanocomposites for Electrocatalysis, *J. Am. Chem. Soc.*, *126*(22), 6876–6877.

[108] **Haque, M.A. and Saif, M.T.A.** (2004). Deformation mechanisms in free-standing nanoscale thin films: a quantitative in situ transmission electron microscope study., *Proceedings of the National Academy of Sciences of the United States of America*, *101*(17), 6335–40.

[109] **Chen, L. and Shen, J.** (1998). Applications of semi-implicit Fourier-spectral method to phase field equations, *Computer Physics Communications*, *108*(2), 147–158.

[110] **Cahn, J.W. and Hilliard, J.E.** (1958). Free Energy of a Nonuniform System. I. Interfacial Free Energy, *The Journal of Chemical Physics*, *28*(2), 258.

[111] **Zhan, H.F.**, **Gu, Y.T. and Yarlagadda, P.K.D.V.** (2011). Advanced Numerical Characterization of Mono-Crystalline Copper with Defects, *Advanced Science Letters*, *4*(4), 1293–1301.

[112] **Yildiz, Y. and Kirca, M.** (2017). Effects of ultrathin coating on the tensile behavior of nanoporous gold, *Journal of Applied Physics*, *122*(8).

[113] **Badwe, N.**, **Chen, X. and Sieradzki, K.** (2017). Mechanical properties of nanoporous gold in tension, *Acta Materialia*, *129*, 251–258.

[114] **Gungor, M.R. and Maroudas, D.** (2005). Relaxation of biaxial tensile strain in ultrathin metallic films: Ductile void growth versus nanocrystalline domain formation, *Applied Physics Letters*, *87*(17), 171913.

[115] **Aqra, F. and Ayyad, A.** (2014). Surface free energy of alkali and transition metal nanoparticles, *Applied Surface Science*, *314*, 308–313.

[116] **Periodictable**, http://periodictable.com/, alındığı tarih: 2019.

[117] **Kolluri, K.**, **Gungor, M.R. and Maroudas, D.** (2008). Atomic-scale analysis of defect dynamics and strain relaxation mechanisms in biaxially strained ultrathin films of face-centered cubic metals, *Journal of Applied Physics*, *103*(12), 123517.

[118] **Kim, T.Y.**, **Dolbow, J.E. and Fried, E.** (2012). Numerical study of the grain-size dependent Young's modulus and Poisson's ratio of bulk nanocrystalline materials, *International Journal of Solids and Structures*, *49*(26), 3942–3952.

[119] **Parida, S.**, **Kramer, D.**, **Volkert, C.A.**, **Rösner, H.**, **Erlebacher, J. and Weissmüller, J.** (2006). Volume Change during the Formation of Nanoporous Gold by Dealloying, *Physical Review Letters*, *97*(3), 035504.

[120] **Yildiz, Y.O. and Kirca, M.** (2018). Compression and shear behavior of ultrathin coated nanoporous gold: A molecular dynamics study, *Journal of Applied Physics*, *124*(18), 184301.

[121] **Ngô, B.N.D.**, **Stukowski, A.**, **Mameka, N.**, **Markmann, J.**, **Albe, K. and Weissmüller, J.** (2015). Anomalous compliance and early yielding of nanoporous gold, *Acta Materialia*, *93*, 144–155.

[122] **Wang, K. and Weissmüller, J.** (2013). Composites of Nanoporous Gold and Polymer, *Advanced Materials*, *25*(9), 1280–1284.

[123] **Jin, H.J.**, **Kurmanaeva, L.**, **Schmauch, J.**, **Rösner, H.**, **Ivanisenko, Y. and Weissmüller, J.** (2009). Deforming nanoporous metal: Role of lattice coherency, *Acta Materialia*, *57*(9), 2665–2672.

[124] **Göken, M.** *Free-Surface Structure and Properties*, John Wiley & Sons, Ltd, Chichester, UK.

[125] **Koh, S.J.A. and Lee, H.P.** (2006). Molecular dynamics simulation of size and strain rate dependent mechanical response of FCC metallic nanowires, *Nanotechnology*, *17*(14), 3451–3467.

[126] **Kelchner, C.L.**, **Plimpton, S.J. and Hamilton, J.C.** (1998). Dislocation nucleation and defect structure during surface indentation, *Physical Review B*, *58*(17), 11085–11088.

[127] **Stukowski, A.**, **Bulatov, V.V. and Arsenlis, A.** (2012). Automated identification and indexing of dislocations in crystal interfaces, *Modelling and Simulation in Materials Science and Engineering*, *20*(8), 085007.

[128] **Stukowski, A. and Albe, K.** (2010). Extracting dislocations and non-dislocation crystal defects from atomistic simulation data, *Modelling and Simulation in Materials Science and Engineering*, *18*(8), 085001.

[129] **Ding, Y. and Zhang, Z.** (2013). *Nanoporous Metals*, Springer Berlin Heidelberg, Berlin, Heidelberg.

[130] **Hakamada, M. and Mabuchi, M.** (2007). Mechanical strength of nanoporous gold fabricated by dealloying, *Scripta Materialia*, *56*(11), 1003–1006.

[131] **Xian, Y.**, **Li, J.**, **Wu, R. and Xia, R.** (2018). Softening of nanocrystalline nanoporous platinum: A molecular dynamics simulation, *Computational Materials Science*, *143*, 163–169.

[132] **Li, J.**, **Xian, Y.**, **Zhou, H.**, **Wu, R.**, **Hu, G. and Xia, R.** (2018). Mechanical properties of nanocrystalline nanoporous gold complicated by variation of grain and ligament: A molecular dynamics simulation, *Science China Technological Sciences*, *61*(9), 1353–1363.

[133] **Gwak, E.J. and Kim, J.Y.** (2016). Weakened Flexural Strength of Nanocrystalline Nanoporous Gold by Grain Refinement, *Nano Letters*, *16*(4), 2497–2502.

[134] **Yildiz, Y. and Kirca, M.** (2017). A novel atomistic modeling technique for poly-crystalline nanoporous metals, *32nd Technical Conference of the American Society for Composites 2017*, volume 3.

[135] **Foley, D.**, **Coleman, S.P.**, **Tschopp, M. and Tucker, G.** (2016). Voronoi-Based Poly-crystalline Generation Algorithm for Atomistic Simulations, **Technical Report**, US Army Research Laboratory, ARL-TN-0806.

[136] **Ahadi, A.**, **Hansson, P. and Melin, S.** (2017). Tensile behavior of single-crystal nano-sized Cu beams – Geometric scaling effects, *Computational Materials Science*, *135*, 127–133.

[137] **Melin, S. and Ahadi, A.** (2017). Strain rate effects at tensile loading of single crystal Cu nano-wires, *International Summer School-Conference "Advanced Problems in Mechanics"*, St. Petersburg, Russia.

[138] **Foiles, S.M.**, **Baskes, M.I. and Daw, M.S.** (1986). Embedded-atom-method functions for the fcc metals Cu, Ag, Au, Ni, Pd, Pt, and their alloys, *Physical Review B*, *33*(12), 7983–7991.

[139] **Daw, M.S. and Baskes, M.I.** (1984). Embedded-atom method: Derivation and application to impurities, surfaces, and other defects in metals, *Physical Review B*, *29*(12), 6443–6453.

[140] **Zhou, M.** (2003). A new look at the atomic level virial stress: on continuum-molecular system equivalence, *Proceedings of the Royal Society of London. Series A: Mathematical, Physical and Engineering Sciences*, *459*(2037), 2347–2392.

[141] **Pilon, Dominic Panneton, Raymond Sgard, Franck Lefebvre, L.P.** (2004). Influence of micro-structural properties on the acoustic performances of novel metallic foams, *Canadian Acoustics*, volume 32.

[142] **Perrot, C.**, **Chevillotte, F. and Panneton, R.** (2008). Bottom-up approach for microstructure optimization of sound absorbing materials, *The Journal of the Acoustical Society of America*, *124*(2), 940–948.

[143] **Chen, Y.C.**, **Lu, Z.**, **Nomura, K.I.**, **Wang, W.**, **Kalia, R.K.**, **Nakano, A. and Vashishta, P.** (2007). Interaction of voids and nanoductility in silica glass., *Physical review letters*, *99*(15), 155506.

[144] **Notario, B.**, **Ballesteros, A.**, **Pinto, J. and Rodríguez-Pérez, M.** (2016). Nanoporous PMMA: A novel system with different acoustic properties, *Materials Letters*, *168*, 76–79.

[145] **Ren, Y.**, **Wang, K.**, **Zhu, B.**, **Wang, X.**, **Wang, X. and Han, F.** (2013). Synthesis of ZnO micro-rods on the cell walls of open celled Al foam and their effect on the sound absorption behavior, *Materials Letters*, *91*, 242–244.

[146] **Hadjiconstantinou, N.G. and Garcia, A.L.** (2001). Molecular simulations of sound wave propagation in simple gases, *Physics of Fluids*, *13*(4), 1040–1046.

[147] **Yano, T.** (2012). Molecular dynamics study of sound propagation in a gas, *AIP Conference Proceedings*, volume1474, American Institute of Physics, pp.75–78.

[148] **Ayub, M.**, **Zander, A.C.**, **Huang, D.M.**, **Howard, C.Q. and Cazzolato, B.S.** (2018). Molecular dynamics simulations of acoustic absorption by a carbon nanotube, *Physics of Fluids*, *30*(6), 066101.

[149] **Ayub, M.**, **Zander, A.**, **Huang, D.**, **Cazzolato, B. and Howard, C.** (2018). Molecular dynamics simulations of classical sound absorption in a monatomic gas, *Journal of Sound and Vibration*, *421*, 319–333.

[150] **Ayub, M.**, **Zander, A.C.**, **Howard, C.Q.**, **Huang, D.M. and Cazzolato, B.S.** (2015). Molecular Dynamics Simulations of Sound Wave Propagation in a Gas and Thermo-Acoustic Effects on a Carbon Nanotube, *Journal of Computational Acoustics*, *23*(04), 1540012.

[151] **Easter, S.R.**, **Baker, C.H. and Norris, P.M.** (2014). Temperature-Dependent Adsorption of Argon on Gold: A Molecular Dynamics Study, *Volume 8B: Heat Transfer and Thermal Engineering*, ASME, p.V08BT10A067.

[152] **Shi, Z.**, **Barisik, M. and Beskok, A.** (2012). Molecular dynamics modeling of thermal resistance at argon-graphite and argon-silver interfaces, *International Journal of Thermal Sciences*, *59*, 29–37.

[153] **Ranjith, R.**, **Park, J. and Myong, R.** (2014). 4TH MICRO AND NANO FLOW CONFERENCE 2014 : proceedings., *4th Micro and Nano Flows Conference proceedings.*, Brunel University, London, UK.

[154] **Wang, R.J. and Xu, K.** (2012). The study of sound wave propagation in rarefied gases using unified gas-kinetic scheme, *Acta Mechanica Sinica*, *28*(4), 1022–1029.

[155] **Kuipers, E.R.**, **Wijnant, Y.H. and de Boer, A.** (2014). Measuring oblique incidence sound absorption using a local plane wave assumption, *Acta Acustica united with Acustica*, *100*(2), 205–214.

[156] **Komarovsky, A.A. and Astakhov, V.P.** (2003). *Physics of strength and fracture control : adaptation of engineering materials and structures*, CRC Press.

[157] **Cai, J. and Ye, Y.Y.** (1996). Simple analytical embedded-atom-potential model including a long-range force for fcc metals and their alloys, *Physical Review B*, *54*(12), 8398–8410.

APPENDICES

APPENDIX A.1 : Input Scripts

APPENDIX A.1

Generation point cloud

```
clear all
clc
wallx=310;
wally=310;
wallz=310;
passband=50000;
dist=80.0;
a=310;
pass=0;
k=1;
while pass<passband
x=rand*wallx;
y=rand*wally;
z=rand*wallz;
site_c=[x y z];
if k==1
site(k,:)=site_c;
k=k+1;
else
[r,c]=size(site);
d1=[ones(r,1)*x ones(r,1)*y ones(r,1)*z];
d=sqrt(sum((site-d1).∧2,2));
varmi=find(d<dist);
if isempty(varmi)
site(k,:)=site_c;
k=k+1
pass=0;
else
```

```matlab
pass=pass+1;
end
end
end
for m=1:1:length(site);
nokt((27*m-26),:)=[site(m,1) site(m,2) site(m,3)];
nokt((27*m-25),:)=[site(m,1) site(m,2) site(m,3)+a];
nokt((27*m-24),:)=[site(m,1) site(m,2) site(m,3)+2*a];
nokt((27*m-23),:)=[site(m,1) site(m,2)+a site(m,3)];
nokt((27*m-22),:)=[site(m,1) site(m,2)+a site(m,3)+a];
nokt((27*m-21),:)=[site(m,1) site(m,2)+a site(m,3)+2*a];
nokt((27*m-20),:)=[site(m,1) site(m,2)+2*a site(m,3)];
nokt((27*m-19),:)=[site(m,1) site(m,2)+2*a site(m,3)+a];
nokt((27*m-18),:)=[site(m,1) site(m,2)+2*a site(m,3)+2*a];
nokt((27*m-17),:)=[site(m,1)+a site(m,2) site(m,3)];
nokt((27*m-16),:)=[site(m,1)+a site(m,2) site(m,3)+a];
nokt((27*m-15),:)=[site(m,1)+a site(m,2) site(m,3)+2*a];
nokt((27*m-14),:)=[site(m,1)+a site(m,2)+a site(m,3)];
nokt((27*m-13),:)=[site(m,1)+a site(m,2)+a site(m,3)+a];
nokt((27*m-12),:)=[site(m,1)+a site(m,2)+a site(m,3)+2*a];
nokt((27*m-11),:)=[site(m,1)+a site(m,2)+2*a site(m,3)];
nokt((27*m-10),:)=[site(m,1)+a site(m,2)+2*a site(m,3)+a];
nokt((27*m-9),:)=[site(m,1)+a site(m,2)+2*a site(m,3)+2*a];
nokt((27*m-8),:)=[site(m,1)+2*a site(m,2) site(m,3)];
nokt((27*m-7),:)=[site(m,1)+2*a site(m,2) site(m,3)+a];
nokt((27*m-6),:)=[site(m,1)+2*a site(m,2) site(m,3)+2*a];
nokt((27*m-5),:)=[site(m,1)+2*a site(m,2)+a site(m,3)];
nokt((27*m-4),:)=[site(m,1)+2*a site(m,2)+a site(m,3)+a];
nokt((27*m-3),:)=[site(m,1)+2*a site(m,2)+a site(m,3)+2*a];
nokt((27*m-2),:)=[site(m,1)+2*a site(m,2)+2*a site(m,3)];
nokt((27*m-1),:)=[site(m,1)+2*a site(m,2)+2*a site(m,3)+a];
nokt((27*m),:)=[site(m,1)+2*a site(m,2)+2*a site(m,3)+2*a];
end
ek=1:1:length(nokt);
site=[ek' nokt];
```

eval(['sites="voronoi_sites_' num2str(k) '_x' num2str(wallx) '_y' num2str(wally) '_z' num2str(wallz) '_d' num2str(dist) '.dat";']);

fid = fopen(sites,'wt');

dlmwrite(sites, site, '-append','coffset', 1, 'delimiter', ' ','newline','pc', 'precision',6);

fclose(fid);

Voro++ input file

```
#include "voro++.hh"
using namespace voro;
// Set up constants for the container geometry
const double x_min=0,x_max=930;
const double y_min=0,y_max=930;
const double z_min=0,z_max=930;
// Set up the number of blocks that the container is divided into
const int n_x=1,n_y=1,n_z=1;
int main() {
//double x,y,z;
// Create a container with the geometry given above, and make it
// non-periodic in each of the three coordinates. Allocate space for
// eight particles within each computational block
container con(x_min,x_max,y_min,y_max,z_min,z_max,n_x,n_y,n_z,false,false,false,8);
wall_plane pln1(1,0,0,670);
con.add_wall(pln1);
wall_plane pln2(-1,0,0,-260);
con.add_wall(pln2);
wall_plane pln3(0,1,0,670);
con.add_wall(pln3);
wall_plane pln4(0,-1,0,-260);
con.add_wall(pln4);
wall_plane pln5(0,0,1,670);
con.add_wall(pln5);
wall_plane pln6(0,0,-1,-260);
con.add_wall(pln6);
//Randomly add particles into the container
con.import("voronoi_sites_34_x310_y310_z310_d80.dat");
```

```
con.draw_cells_gnuplot("voronoi_sites_34_x310_y310_z310_d80.gnu"); }
```

Definition of line segments

```
clear all
clc
name='voronoi_sites_34_x310_y310_z310_d80';
fname=strcat(name,'.gnu');
eval(['load ' strcat(name,'.gnu')])
vertices=voronoi_sites_34_x310_y310_z310_d80;
fid = fopen(strcat(name,'.gnu'));
radik=10.0;
lines = textscan(fid, '%s', 'Delimiter', '\n');
lines = lines{1};
% Find all the blank lines using cellfun:
blank_lines1= find(cellfun('isempty', lines));
len=length(blank_lines1);
blank_lines1(len-1:len)=[];
blank_lines2=blank_lines1(1:2:length(blank_lines1));
[r,c]=size(vertices);
m=1;j=1;n=1;k=1;
fclose(fid);
while m<r
if n+1~=blank_lines2(j)
n_v(k,:)=[vertices(m,:) vertices(m+1,:)];
m=m+1;
n=n+1;k=k+1;
else
n_v(k,:)=[vertices(m+1,:) vertices(m+2,:)];
m=m+2;
j=j+1;
n=n+4;k=k+1;
end
end
x=[n_v(:,1)';n_v(:,4)'];
```

```
y=[n_v(:,2)';n_v(:,5)'];
z=[n_v(:,3)';n_v(:,6)'];
plot3(x,y,z)
lines=strcat('lines_cyl_',name(15:length(name)),'.dat');
fid = fopen(lines,'wt');
dlmwrite(lines, n_v,'coffset', 1, 'delimiter', ' ','newline','pc', 'precision',6);
fclose(fid);
```

Generation of a Lammps script

```
clc
clear
name='voronoi_sites_34';
lines='lines_cyl_34_x310_y310_z310_d80.dat';
n_v=importdata(lines);
wallx=930;
wally=930;
wallz=930;
sratio_min=0.538721;
lattice=4.08; %Au:4.08 Cu:3.615 pt:3.92
kat=1.5;
minrad=lattice*kat;
minlen=minrad;
radii=10;
wall=[wallx;wally;wallz];
name2=name(15:length(name));
name2=strcat(name2,'_wallx_',num2str(wallx),'_wally_',num2str(wally),
'_wallz_',num2str(wallz));
mkdir(name2);
copyfile(lines,name2);
copyfile('Pt-Au.eam.alloy',name2);
[coord]=lines_voro_non(n_v,sratio_min,minlen,name2);
coat_thick=8; %Thickness of coating in radius (Angstrom)
voro_lammps_coating(coord,name2,wall, coat_thick)
```

Function (lines_voro_non)

```
function [coord]=lines_voro_non(lines,sratio_min,minlen,name)
point1=lines(:,1:3);
point2=lines(:,4:6);
lngth=sqrt(sum((point1-point2).^2,2));
lines(find(lngth<minlen),:)=[];
point1=lines(:,1:3);
point2=lines(:,4:6);
vert=unique([point1;point2],'rows');
vert=unique(vert,'rows');
lngth=sqrt(sum((point1-point2).^2,2));
hml=length(lines);
vec=ones(length(lines),1);
vec2=ones(length(vert),1);
m=1;n=1;
for k=1:length(vert)
id1=find(ismember(point1, vert(k,:),'rows')==1);
id2=find(ismember(point2, vert(k,:),'rows')==1);
ids=unique([id1;id2]);
lngth_id=lngth(ids);
minl=min(lngth_id);
maxl=max(lngth_id);
radii(k)=mean(lngth_id)*sratio_min;
end
coord0=[vert radii'];
for i=1:length(lines)
tip1=lines(i,1:3);
tip2=lines(i,4:6);
dist=sqrt(sum((tip2-tip1).^2));
vid1=find(ismember(vert,tip1,'rows')==1);
vid2=find(ismember(vert,tip2,'rows')==1);
r1=radii(vid1);
r2=radii(vid2);
rm=(r1+r2)/3;
if r1>r2
```

```
r11=r1;r22=r2;
tip11=tip1;tip22=tip2;
else
r11=r2;r22=r1;
tip11=tip2;tip22=tip1;
end
tt=1-rm/r11;
abct=tip22-tip11;
crdm=abct*tt+tip11;
dist1=tt*dist;
dist2=dist-dist1;
N1=ceil(dist1/(rm));
tt1=0:1/N1:1;
tt1(1)=[];
abct=crdm-tip11;
kac=length(tt1);
for j=1:kac;
xyzt=abct*tt1(j)+tip11; % point coordinates on target line
coord1(m,1:3)=xyzt;
coord1(m,4)=r11-(r11-rm)*tt1(j);
m=m+1;
end
N2=ceil(dist2/(rm));
tt2=0:1/N2:1;
tt2(1)=[];
tt2(length(tt2))=[];
abct=crdm-tip22;
kac=length(tt2);
for j=1:kac;
xyzt=abct*tt2(j)+tip22; % point coordinates on target line
coord2(n,1:3)=xyzt;
coord2(n,4)=r22+(rm-r22)*tt2(j);
n=n+1;
end
m=m+1;
```

```
n=n+1;
%
end
coord=[coord0; coord1; coord2];
coord=unique(coord,'rows');
coord(1,:)=[];
coord_f=strcat('coord_smin',num2str(sratio_min),'.dat');
fid = fopen(coord_f,'wt');
dlmwrite(coord_f, coord, '-append','coffset', 1, 'delimiter', ' ','newline','pc',
'precision',6);
fclose(fid);
movefile(coord_f,name);
```

Function (voro_lammps_coating)

```
function voro_lammps_coating(coord,name,wall, coat_thick)
name2=strcat(name2,'_wallx_',num2str(wallx),'_wally_',
num2str(wally),'_wallz_',num2str(wallz),'_radii_',num2str(radii));
cent=coord;
wallx=wall(1);
wally=wall(2);
wallz=wall(3);
min=0.46;
lattice_core=4.08;
lattice_coat=3.92;
id=find(cent(:,1)<wallx & cent(:,1)>min & cent(:,2)<wally & cent(:,2)>min &
cent(:,3)<wallz & cent(:,3)>min );
cent=cent(id,:);
%Writing the include file
inc='include_porous_core_sp.dat';
inc2='include_porous_coat_sp.dat';
inc3='include_porous_del_sp.dat';
inc4='radiiofmodel.dat';
fid = fopen(inc,'wt'); % central points of spherical regions for core material
fid2 = fopen(inc2,'wt'); % central points of spherical regions for coating
fid3 = fopen(inc3,'wt'); %
```

```
fid4 = fopen(inc4,'wt');
fprintf(fid,'## %s \n', name);
fprintf(fid2,'## %s \n', name);
fprintf(fid2,'## Thickness of coating %6.3f \n', coat_thick);
fprintf(fid4,'## %s \n', name);
dlmwrite(inc4, cent, '-append', 'delimiter', ' ','newline','pc', 'precision',6);
fclose(fid4);
movefile(inc4,name);
m=1;
for k=1:length(cent)
if k<2
fprintf(fid,'region %5.1d sphere %6.3f %6.3f %6.3f %6.3f side in units box\n',m,
cent(k,1),cent(k,2),cent(k,3),cent(k,4));
m=m+1;
else
fprintf(fid,'region %5.1d sphere %6.3f %6.3f %6.3f %6.3f side in units box\n',m,
cent(k,1),cent(k,2),cent(k,3),cent(k,4));
m=m+1;
fprintf(fid,'region %5.1d union 2 %5.1d %5.1d units box\n',m, m-1, m-2);
m=m+1;
end
fixed(k,1),fixed(k,2),fixed(k,3),radyus2);
end
fprintf(fid,'lattice fcc %7.4f\n',lattice_core);
fprintf(fid,'create_atoms 1 region %5.1d\n',m-1);
fclose(fid);
movefile(inc,name);
for j=1:m-1
fprintf(fid3,'region %5.1d delete\n',j);
end
fprintf(fid3,'log log_after_delete.txt\n');
fclose(fid3);
movefile(inc3,name);
m=1;
for k=1:length(cent)
```

```matlab
if k<2
fprintf(fid2,'region m_%s sphere %6.3f %6.3f %6.3f %6.3f side out units box\n',num2str(m), cent(k,1),cent(k,2),cent(k,3),cent(k,4));
fprintf(fid2,'region c_%s sphere %6.3f %6.3f %6.3f %6.3f side in units box\n',num2str(m), cent(k,1),cent(k,2),cent(k,3),cent(k,4)+coat_thick);
m=m+1;
else
fprintf(fid2,'region m_%s sphere %6.3f %6.3f %6.3f %6.3f side out units box\n',num2str(m), cent(k,1),cent(k,2),cent(k,3),cent(k,4));
fprintf(fid2,'region c_%s sphere %6.3f %6.3f %6.3f %6.3f side in units box\n',num2str(m), cent(k,1),cent(k,2),cent(k,3),cent(k,4)+coat_thick);
m=m+1;
fprintf(fid2,'region m_%s intersect 2 m_%s m_%s units box\n',num2str(m), num2str(m-1), num2str(m-2));
fprintf(fid2,'region c_%s union 2 c_%s c_%s units box\n',num2str(m),num2str(m-1),num2str(m-2));
m=m+1;
end
end
fprintf(fid2,'region c_%s intersect 2 c_%s m_%s units box\n',num2str(m), num2str(m-1),num2str(m-1));
fprintf(fid2,'lattice fcc %8.4f\n',lattice_coat);
fprintf(fid2,'create_atoms 2 region c_%s\n',num2str(m));
fprintf(fid2,'log log_after_coat.txt\n');
fclose(fid2);
movefile(inc2,name);
%%%%%%%%%Writing the input script %%%%%%%%%%%%%%%%%%
region_id=m-1;
inc='include_porous_core_sp.dat';
inc1='include_porous_coat_sp.dat';
inc3='include_porous_del_sp.dat';
inc2='porous_coat_sp.in';
fid = fopen(inc2,'wt');
xmin=310; %Main block sizes
xmax=620;
ymin=310;
ymax=620;
```

zmin=310;

zmax=620;

sim_xmin=xmin-50; %Simulation box sizes

sim_xmax=xmax+50;

sim_ymin=ymin-50;

sim_ymax=ymax+50;

sim_zmin=zmin-50;

sim_zmax=zmax+50;

fprintf(fid,'# 3D nanoporous material\n');

fprintf(fid,'dimension 3\n');

fprintf(fid,'boundary p p p\n');

fprintf(fid,'atom_style atomic\n');

fprintf(fid,'units metal\n');

fprintf(fid,'neighbor 2.0 bin\n');

fprintf(fid,'neigh_modify every 1 check yes\n');

fprintf(fid,'# create geometry\n');

fprintf(fid,'region box block %6.3f %6.3f %6.3f %6.3f %6.3f %6.3f units box\n',sim_xmin,sim_xmax,sim_ymin,sim_ymax,sim_zmin,sim_zmax);

fprintf(fid,'create_box 2 box\n');

box\n',xmin,xmax,ymin,ymax,zmin,zmax);

fprintf(fid,'include %s \n',inc);

fprintf(fid,'include %s \n',inc3);

fprintf(fid,'include %s \n',inc1);

fprintf(fid,'region x1 block INF %6.1f INF INF INF INF units box\n',xmin);

fprintf(fid,'region x2 block %6.1f INF INF INF INF INF units box\n',xmax);

fprintf(fid,'region y1 block INF INF INF %6.1f INF INF units box\n',ymin);

fprintf(fid,'region y2 block INF INF %6.1f INF INF INF units box\n',ymax);

fprintf(fid,'region z1 block INF INF INF INF INF %6.1f units box\n',zmin);

fprintf(fid,'region z2 block INF INF INF INF %6.1f INF units box\n',zmax);

fprintf(fid,'region sil union 6 x1 x2 y1 y2 z1 z2\n');

fprintf(fid,'delete_atoms region sil\n');

fprintf(fid,'change_box all x final %6.1f %6.1f y final %6.1f %6.1f z final %6.1f %6.1f units box\n', xmin, xmax, ymin, ymax, zmin, zmax);

fprintf(fid,'# EAM potential\n');

fprintf(fid,'pair_style eam/alloy\n');

```
fprintf(fid,'pair_modify shift yes\n');
fprintf(fid,'pair_coeff * * Pt-Au.eam.alloy Au Pt\n');
fprintf(fid,'dump 1 all xyz 50 coated_coord.xyz\n');
fprintf(fid,'dump 3 all custom 50 coated_coord.lammpstrj id type x y z\n');
fprintf(fid,'run 1\n');
fclose(fid);
movefile(inc2,name);
```

CURRICULUM VITAE

Name Surname: Yunus Onur YILDIZ

Place and Date of Birth: Ankara - 22.07.1981

E-Mail: yunusonur@gmail.com

EDUCATION:

- **B.Sc.:** 2004, Erciyes University, Mechanical Engineering

- **M.Sc.:** 2007, Gazi University, Mechanical Engineering

PROFESSIONAL EXPERIENCE AND REWARDS:

- **2019-present** Research Assistant, Sinop University.

- **2014-2019** Research Assistant, Istanbul Technical University.

- **2018-2019** Visiting Researcher, Lund University.

- **2013-2014** Research Assistant, Firat University.

- **2009-2012** Oceangoing Watchkeeping Engineer, YASA Holding A.S.

PUBLICATIONS, PRESENTATIONS AND PATENTS ON THE THESIS:
<u>Articles</u>

- **Yildiz Y. O.**, Ahadi, A. and Kirca, M. 2019. Strain Rate Effects on Tensile and Compression Behavior of Nano-crystalline Nanoporous Gold : A Molecular Dynamic Study, *Mechanics of Materials*, in Review.

- **Yildiz Y. O.** and Kirca M. 2019. Acoustical Properties of Platinum and Silver Coated Nanoporous Gold: A Molecular Dynamic Study, *The Journal of Sound and Vibration*, in Review.

- **Yildiz Y. O.** and Kirca M. 2018. Compression and Shear Behavior of Ultrathin Coated Nanoporous Gold: A Molecular Dynamics Study, *Journal of Applied Physics*, 124, 184301.

- **Yildiz Y. O.** and Kirca M. 2017. Effects of Ultrathin Coating on the Tensile Behavior of Nanoporous Gold, *Journal of Applied Physics*, 122, 084305.

- **Yildiz Y. O.** and Kirca M. 2017. Atomistic Simulation of Voronoi-based Coated Nanoporous Metals, *Modelling and Simulation in Materials Science and Engineering*, 25, 025008.

Conferences

- **Yildiz Y. O.**, Ahadi A. and Kirca M. 2019. Grain Size Effects on Tensile Behaviour of Nanocrystalline Nanoporous Gold. *The fourth International Symposium on Atomistic and Multiscale Modeling of Mechanics and Multiphysics*, August 05-08, 2019 Nurnberg, Germany.

- **Yildiz Y. O.** and Kirca M. 2017. A Novel Atomistic Modeling Technique for Polycrystalline Nanoporous Metals. *32nd Annual Technical Conference*, October 23-25, 2017 West Lafayette, Indiana, USA.

- **Yildiz Y. O.** and Kirca M. 2016. Effects of Nano-Coating on the Mechanical Behavior of Nanoporous Metals. *ICTAMM 2016 : 18th International Conference on Theoretical and Applied Multiscale Mechanics*, August 04-05, 2016 Amsterdam, The Netherlands.

OTHER PUBLICATIONS, PRESENTATIONS AND PATENTS:
Articles

- Erturk A. S., **Yildiz Y. O.** and Kirca M. 2019. Mechanical Performance and Morphological Evolution of Heat-Treated Nanoporous Gold: A Molecular Dynamics Study, *Physica E: Low-dimensional Systems and Nanostructures*, 108, 15-21.

- Gulmez, D. E. **Yildiz Y. O.** and Kirca M. 2018. Nanoporous gold reinforced with carbon based nanomaterials: A molecular dynamics study, *Composites Part B: Engineering*, 151, 62-70.

- Erturk A. S., **Yildiz Y. O.** and Kirca M. 2018. Mechanical behavior of a novel carbon-based nanostructured aluminum material, *Computational Materials Science*, 144, 193-209.

- Zeinalabedini H., **Yildiz Y. O.** Zhang P., Laux K., Kirca M., and To A.C. 2016. Homogenization of Additive Manufactured Polymeric Foams with Spherical Cells, *Additive Manufacturing*, 12, 274-281.

- Gunay E., Aygun C. and **Yildiz Y. O.** 2014. Nonlinear Buckling Finite Element Analysis of Stiffened Boron-Al Plates, *Computational Materials Science*, 24, 20-28.

- Gunay E., Aygun C. and **Yildiz Y. O.** 2013. Nonlinear Buckling Finite Element Analysis of Stiffened Steel Plates, *Advanced Materials Research*, 699, 450-456.

- **Yildiz Y. O.** and Gunay E. 2007. Stability Analysis of Stiffened Isotropic Thin Plates Using Finite Element Method, *Journal of The Institute of Science and Technology of Erciyes University*, 23, 171-187.

Conferences

- **Yildiz Y. O.**, Erturk A. S., Ahadi A. and Kirca M. 2018. Coated Nanoporous Structures Subjected to Stress Relief Annealing. *31st Nordic Seminar in Computational Mechanics*, October 25-26, 2018 Umea, Sweden.

- **Yildiz Y. O.** and Kirca M. 2017. Modelling and Simulation of Multilayer Coated Nanoporous Metals. *ICCE-25: The 25th Annual International Conference on Composites/Nano Engineering*, July 16-22, 2017 Roma, Italy.

- Gunay E., Aygun C. and **Yildiz Y. O.** 2013. Nonlinear Buckling Finite Element Analysis of Stiffened Boron-Al Plates. *9th International Conference on Fracture and Strength of Solids*, June 9-13, 2013 Jeju, Korea.

- **Yildiz Y. O.** and Kirca M. 2006. Buckling Analysis of Stiffened Composite Plates Under Bi-axial Loading with FEM. *1st National Conference on Aeronautics and Aerospace Technologies*, September 21-23, 2006 Middle East Technical University, Ankara.